Solid State NMR studies of functional oxides

Chiara Ferrara

THÈSE

en vue de l'obtention du grade de

Docteur de l'Université de Lyon, délivré par l'École Normale Supérieure de Lyon

En cotutelle avec Università degli Studi di Pavia

Discipline : CHIMIE

Laboratoire Centre de Résonance Magnétique Nucleaire a Très Hauts Champs

École Doctorale en Chimie

présentée et soutenue publiquement le date 6 Février 2014

par Madame Chiara FERRARA

SOLID STATE NMR STUDIES OF FUNCTIONAL OXIDES

Directeur de thèse : Dr. Guido PINTACUDA

Co-directeur de thèse : Prof. P. MUSTARELLI

Après l'avis de : Prof. Michaël DESCHAMPS
Dr. Roberto SIMONUTTI

Devant la commission d'examen formée de :

Prof. Mariano CASU, Università degli Studi di Cagliari, Examinateur

Prof. Michaël DESCHAMPS, Université Orleans, Rapporteur

Dr. Anne LESAGE, Ecole Normale Supérieure de Lyon, Examinateur

Prof. Piercarlo MUSTARELLI, Università degli Studi di Pavia, Co- directeur

Dr. Guido PINTACUDA, Ecole Normale Supérieure de Lyon, Directeur

Dr. Roberto SIMONUTTI, Università degli Studi di Milano Bicocca, Rapporteur

Keywords:

RMN du solide, oxydes fonctionnels, matériaux, caractérisation structurale, RMN quadripolaire, RMN paramagnétique, perovskite, mélilite, orthosilicates famille, MQMAS, aMAT, SHAPS.

Solid state NMR, functional oxides, materials, structural characterization, quadrupolar NMR, paramagnetic NMR, perovskite structure, melilite system, orthosilicates family, MQMAS, aMAT, SHAPS.

Résumé

Les oxydes fonctionnels sont des matériaux qui manifestent des propriétés intéressantes. L'étude de l'environnement local par rapport à la structure moyenne idéale est essentiel et peut être fourni par l'utilisation de techniques modernes de résonance magnétique nucléaire (RMN). Le travail présenté dans cette thèse suit et développe ces approches combinées pour l'enquête de trois classes différentes d'oxydes fonctionnels qui trouvent des applications dans des domaines d'intérêt technologique pertinente, comme l'optique et de l'énergétique : système perovskite $LaSrAlO_4$, mélilite $LaSr(Ga/Al)_3O_7$ et la famille de orthosilicates $Li_2(Fe/Mn)SiO_4$.

Abstract

The functional oxides are performing materials showing interestant properties. The study of the local environment respect to the average structure is essential for the deep understanding of the correlations between structure and properties ; this investigation of short and medium range can be performed with the use of solid state NMR techniques. In particular in this thesis three different classes of materials for applications in fields of optic and energy are considered : perovskite structure $LaSrAlO_4$, the melilite system $LaSr(Ga/Al)_3O_7$ and the family of orthosylicates $Li_2(Fe/Mn)SiO_4$.

Introduction

Les oxydes fonctionnels sont des matériaux qui manifestent des propriétés intéressantes et qui peuvent être exploitées dans de nombreux domaines technologiques comme l'optique et de l'énergétique. Les propriétés correspondantes de ces matériaux (les propriétés de transport de conduction ionique et électrique ou des phénomènes optiques et magnétiques) sont liées à la présence de défauts dans la structure. Dans le même temps, la présence de ces entités complique considérablement la détermination de la structure du matériau considéré, qui est la première étape pour la compréhension des propriétés fonctionnelles finales, en introduisant des différences entre le niveau local et la structure moyenne du système. L'étude de l'environnement local, des distorsions et écarts par rapport à la structure moyenne idéale est donc indispensable et peut être fourni par l'utilisation de techniques modernes de résonance magnétique nucléaire (RMN).

La RMN à l'état solide est devenue une technique primaire pour la caractérisation structurale et dynamique d'oxydes fonctionnels complexes. Un avantage clé d'une expérience de RMN est l'échelle locale de l'information obtenue. De plus, la sonde RMN est sélective, et presque tous les noyaux peuvent être étudiés séparément, et deux signatures (déplacement chimique et détails de relaxation) peuvent être obtenus.
Dans le même temps, les oxydes fonctionnels présentent souvent des complications supplémentaires à partir du point de vue de la RMN, comme une forte anisotropie structurelle, et la présence d'interactions quadrupolaires électriques et paramagnétiques. Dans le passé, l'ensemble de ces éléments a représenté graves limitations à l'application de la RMN pour l'étude de ces systèmes. L'innovation continue dans la technologie des sondes, à savoir l'avènement de la rotation rapide et ultra-rapide à l'angle

magique, le développement de nouvelles séquences d'impulsions, et la disponibilité des champs magnétiques très élevés ont ouvert la voie à l'étude de matériaux fonctionnels de plus en plus complexes. Avec la possibilité d'approcher expérimentalement ces systèmes, le développement parallèle de nouvelles et puissantes techniques de calcul conduit également à une meilleure compréhension des liens entre les observables RMN et l'information structurelle.

Le travail présenté dans cette thèse suit et développe ces approches combinées pour l'enquête de trois classes différentes d'oxydes fonctionnels qui trouvent des applications dans des domaines d'intérêt technologique pertinente, comme l'optique et de l'énergétique.

Les concepts fondamentaux et les principales caractéristiques des expériences de RMN sont discutés dans le chapitre 1. L'Hamiltonien globale du système RMN est défini et les termes singuliers sont discutés, les problèmes liés à la présence de différentes interactions sont définies ainsi que des stratégies et des techniques utilisées pour aborder les systèmes présentés dans les chapitres suivants.

Le chapitre 2 est consacré à l'analyse du système $LaSrAlO_4$. Ce système à couches appartient à la famille des composés $AA'BO_4$, un sous-groupe de l'oxyde à base de A_2BO_4 avec une structure de type K_2NiF_4, connu comme étant le premier élément de la série de Ruddlesden - Popper (RP). L'analyse structurale est effectuée par une combinaison de mesures de RMN, des mesures de diffraction de radiation de synchrotron et de neutrons, et l'analyse de la fonction de distribution de couple obtenue à partir de techniques de modélisation atomistique.

Le chapitre 3 présente les résultats obtenus pour l'enquête de la famille mélilite de composés de formule générale $LaSrGa_{3-x}Al_xO_7$ avec x = 0, 1, 1.5, 2, 3. Ces composés sont étudiés à l'aide de rayons X et la diffraction des neutrons afin d'obtenir une caractérisation complète de la structure à longue portée. Comme la structure présente une forte anisotropie et un haut degré de désordre, la RMN du solide est nécessaire pour étudier l'ordre local. Les deux Ga et Al sont des noyaux quadripolaires et donc la rotation rapide à l'angle magique (MAS) et des champs magnétiques élevés sont requis avec des séquences d'impulsions spécifiques (quantique multiple MAS , MQMAS). Un aperçu complet de la structure a été réalisée pour les échantillons $LaSrAl_3O_7$ pour lesquels calculs avec la théorie fonctionnelle de densité (DFT) ont été effectués. Résultats sur ce modèle de référence ont ensuite été utilisées pour comprendre les données obtenues pour la série complète d'échantillons Ga / Al .

Dans le chapitre 4, matériaux pour une application comme cathodes dans les batteries au lithium sont considérées. Nous avons considéré la série des orthosilicates de formule générale $Li_2Mn_{1-x}Fe_xSiO_4$ avec x = 0, 0.25, 0.5, 0.75, 1. Cette série est une alternative possible à la famille bien connue des $LiMn_{1-x}Fe_{1+x}PO_4$, car elle offre une capacité électrique très élevée en raison de la présence de deux ions lithium dans la structure par unité de formule disponibles pour le processus électrochimique. Un travail préliminaire a été réalisée sur des échantillons en abondance naturelle préparés selon différentes techniques de synthèse. Cette famille de composés se caractérise par une grande variété de formes polymorphes, qui peut être obtenue en faisant varier la composition et les conditions de synthèse. La caractérisation structurale n'est pas trivial et l'utilisation combinée de la technique traditionnelle de longue portée (diffraction) et sonde locale (RMN à l'état solide) est obligatoire. L'étude RMN de cette famille de composés s'est avérée très difficile, en raison de la forte

interaction paramagnétique lié à la présence d'ions de métaux de transition. Afin d'améliorer la sensibilité des expériences de RMN, la séparation des isotopes du ^{29}Si a ainsi été réalisée. L'utilisation combinée de l'étiquetage ^{29}Si, champs magnétiques moyens-hauts, rotation ultra rapide MAS et des séquences d'impulsions sur la base des impulsions adiabatiques nous a permis d'obtenir des spectres résolus de ^{7}Li et ^{29}Si.
Les principaux points et conclusions des travaux présentés dans les chapitres précédents sont donnés dans les conclusions avec le potentiel des techniques de RMN appliquées aux systèmes complexes.

Le travail de trois ans de cet projet de thèse a été réalisé entre le Dipartimento di Chimica de l'Università degli Studi di Pavia, en Italie, où les procédures de synthèse, d'analyse de structure (RMN, DRX) et les calculs préliminaires ont été effectuées, et le Centre de RMN à Très Haut Champ de l'École Normale Supérieure de Lyon, France où les mesures de RMN ont été recueillies et analysées.

Introduction

Solid State Nuclear Magnetic Resonance, *ssNMR*, has obtained a primary role for both structural and dynamic characterization of complex functional oxides. The key issue is the local scale of the information obtained from the NMR experiment. Moreover, the NMR probe is selective, and nearly all the nuclei can be separately investigated. Finally, both chemical shift signatures, and relaxation details can be obtained.

Functional oxides are materials that manifest interesting properties that can be exploited in many different technological fields. In many cases the relevant properties of a material are related to the presence of defects in the structure. The role of the defects is crucial for the rising of properties (transport properties as ionic and electric conduction or optical and magnetic phenomena). At the same time, the presence of these entities significantly complicates the structural determination of the considered material, that is the first step for the understanding of the final functional properties, introducing differences between the local and the average structure of the system. The study of local environment, distortions and deviations from the ideal average structure is thus essential and can be provided by the use of modern NMR techniques.
At the same time, functional oxides often present additional complications from the point of view of NMR, such as strong structural anisotropy, and the presence of electric quadrupolar and paramagnetic interactions. In the past, all these elements represented severe limitations to the application of NMR to the study of these systems. The continuous innovation in probes technology, *i.e.* the advent of fast and ultra fast magic angle spinning, the development of new pulses and sequences dedicated to specific problems, and the availability of very high

magnetic fields are paving the way to the study of more and more complex functional materials. Together with the possibility of experimentally approaching these complex systems, the parallel development of new and powerful computational techniques is also leading to a deeper understanding of the connections between the NMR observables and the structural information.
The work presented in this thesis follows and develops these combined approach for the investigation of three different classes of functional oxides that find applications in some fields of relevant technological interest, such as optics and energetics.

The fundamental concepts and the key features of the NMR experiments are discussed in *Chapter 1*. Here the global Hamiltonian of the NMR system is defined and the singular terms are discussed; the problems related to the presence of different interactions are defined together with strategies and techniques used to approach the systems presented in the following chapters.

Chapter 2 is devoted to the analysis of the $LaSrAlO_4$ system. This layered system belongs to the family of $AA'BO_4$ compounds, a subgroup of the A_2BO_4-based oxide with K_2NiF_4-type structure, known as the first member of the Ruddlesden-Popper (RP) series. The structural analysis is performed with a combination of NMR measurements, neutron and synchrotron diffraction measurements and pair distribution function analysis obtained from atomistic modeling techniques.

Chapter 3 presents the results obtained for the investigation of the melilite family of compounds with general formula $LaSrGa_{3-x}Al_xO_7$ with x =0, 1, 1.5, 2, 3. These compounds are investigated by means of X ray and neutron diffraction in order to obtain full long range structural characterization. As the structure presents strong anisotropy and a high degree of disorder, solid-state NMR is

required to investigate the local order. Both Ga and Al are quadrupolar nuclei and thus fast magic-angle spinning (MAS) and high magnetic fields are required together with specific pulse sequences (multiple-quantum MAS, MQMAS). A complete insight into the structure was performed for the sample $LaSrAl_3O_7$ for which density functional theory (DFT) calculations were performed. Results on this reference model were then used to understand the data obtained for the full series of Ga/Al samples.

In *Chapter 4* materials for application as cathodes in lithium batteries are considered. We considered the series of orthosilicates of general formula $Li_2Mn_{1-x}Fe_xSiO_4$ with x = 0, 0.25, 0.5, 0.75, 1. This series is a possible alternative to the well known family of $LiMn_{1-x}Fe_{1+x}PO_4$, as it offers a very high electrical capacity due to the presence of two lithium ions in the structure per formula unit available for the electrochemical process. Preliminary work was carried out on natural abundance samples prepared according to different synthesis techniques. This family of compounds is characterized by a huge variety of polymorphs which can be obtained by varying composition and synthesis conditions. The structural characterization is not trivial and the combined use of traditional long-range technique (diffraction) and local probe (solid state NMR) is mandatory. The NMR study of this family of compounds proved to be very challenging, due to the strong paramagnetic interaction related to the presence of transition metal ions. In order to improve the sensitivity of the NMR experiments, isotopic enrichment of ^{29}Si was thus performed. The combined use of ^{29}Si labeling, medium-high magnetic fields, ultra fast MAS and pulse sequences based on adiabatic pulses allowed us to obtain resolved spectra of ^{7}Li and ^{29}Si.

Università degli Studi
di Pavia

Dipartimento di Chimica
Sezione Chimica Fisica

École Normale Supérieure
de Lyon

Centre de résonance
magnétique nucléaire

Thesis

Dottorato in Scienze Chimiche
S.S.D. CHIM/02

Doctorat en Chimie

Dissertation

SOLID STATE NMR STUDIES OF FUNCTIONAL OXIDES

Presented and discussed by

Chiara FERRARA

Supervisor:
Prof. P. MUSTARELLI

Supervisor:
Dr. G. PINTACUDA

Présentée et soutenue publiquement devant la comission d'examen formée de

Prof. P. MUSTARELLI
Prof. M. CASU
Dr. R. SIMONUTTI

Dr. G. PINTACUDA
Dr. A. LESAGE
Prof. M. DESCHAMPS

Year 2014

Bibliographical identification

Name of the author:	Chiara FERRARA
Title of the thesis:	Solid State NMR studies of functional oxides
Phd program:	Scienze Chimiche Chimie
Supervisors:	Prof. P. MUSTARELLI Dr. G. PINTACUDA
Year of graduation:	2014
Keywords:	Solid state NMR, functional oxides, materials, structural characterization, quadrupolar NMR, paramagnetic NMR, perovskite structure, melilite system, orthosilicates family, MQMAS, aMAT, SHAPS.

Acknowledgments

I would like to express my gratitude to my supervisors, Prof. Piercarlo Mustarelli and Dr. Guido Pintacuda for having proposed me this project and for the supporting during the three year work of study and research.

My sincere thanks also go to Dr. Cristina Tealdi and Dr. Andrew Pell for the precious knowledge, the time spent with me and for me. I'm grateful to have had the opportunity to work with them.

I would like to acknowledge the French Ministry for the Foreign Affairs for the financial support (dossier n. 781569G).

For different reasons, my sincere and boundless thanks go also to Luca and Francesca and to my family.

Fortune's always hiding,
I've looked everywhere,
I'm forever blowing bubbles,
Pretty bubbles in the air…

VII

Declaration of the student

I declare that I have worked on this thesis independently using only primary and secondary sources listed in the references.

Chiara Ferrara

INDEX

Pag.

Chapter 1

Introduction

Chapter 2
The perovskite compound $LaSrAlO_4$

Chapter 3

The melilite series $LaSr(Ga/Al)_3O_7$

Chapter 4

The orthosilicates series Li_2MSiO_4

Pag.

Chapter 1

Introduction

Chapter 2

The perovskite compound $LaSrAlO_4$

Chapter 3

The melilite series $LaSr(Ga/Al)_3O_7$

Chapter 4

The orthosilicates series Li_2MSiO_4

Abstract

Solid State Nuclear Magnetic Resonance, *ssNMR*, has obtained a primary role for both structural and dynamic characterization of complex functional oxides. This prominent position between the characterization techniques is due to some relevant features of the solid state NMR. The key issue is the local scale of the information obtained from the NMR experiment. Moreover, the NMR probe is selective, and nearly all the nuclei can be separately investigated. Finally, both chemical shift signatures, and relaxation details can be obtained.

Functional oxides are materials that manifest interesting properties that can be exploited in many different technological fields. In many cases the relevant properties of a material are related to the presence of defects in the structure. Defects can be represented by vacancies, substitutions, interstitial species intrinsically or intentionally introduced into the system. The role of the defects is crucial for the rising of properties (transport properties as ionic and electric conduction or optical and magnetic phenomena). At the same time, the presence of these entities significantly complicates the structural determination of the considered material, that is the first step for the understanding of the final functional properties, introducing differences between the local and the average structure of the system. The study of local environment, distortions and deviations from the ideal average structure is thus essential and can be provided by the use of modern NMR techniques.
At the same time, functional oxides often present additional complications from the point of view of NMR, such as strong structural anisotropy, and the presence of electric quadrupolar and paramagnetic interactions. In the past, all these elements represented severe limitations to the application of NMR to the

study of these systems. The continuous innovation in probes technology, *i.e.* the advent of fast and ultra fast magic angle spinning, the development of new pulses and sequences dedicated to specific problems, and the availability of very high magnetic fields are paving the way to the study of more and more complex functional materials. Together with the possibility of experimentally approaching these complex systems, the parallel development of new and powerful computational techniques is also leading to a deeper understanding of the connections between the NMR observables and the structural information.
The work presented in this thesis follows and develops these combined approach for the investigation of three different classes of functional oxides that find applications in some fields of relevant technological interest, such as optics and energetics.

The fundamental concepts and the key features of the NMR experiments are discussed in *Chapter 1*. Here the global Hamiltonian of the NMR system is defined and the singular terms are discussed; the problems related to the presence of different interactions are defined together with strategies and techniques used to approach the systems presented in the following chapters.

Chapter 2 is devoted to the analysis of the $LaSrAlO_4$ system. This layered system belongs to the family of $AA'BO_4$ compounds, a subgroup of the A_2BO_4-based oxide with K_2NiF_4-type structure, known as the first member of the Ruddlesden-Popper (RP) series. The structural analysis is performed with a combination of NMR measurements, neutron and synchrotron diffraction measurements and pair distribution function analysis obtained from atomistic modeling techniques.

Chapter 3 presents the results obtained for the investigation of the melilite family of compounds with general formula $LaSrGa_{3-}$

$_xAl_xO_7$ with x =0, 1, 1.5, 2, 3. These compounds are investigated by means of X ray and neutron diffraction in order to obtain full long range structural characterization. As the structure presents strong anisotropy and a high degree of disorder, solid-state NMR is required to investigate the local order. Both Ga and Al are quadrupolar nuclei and thus fast magic-angle spinning (MAS) and high magnetic fields are required together with specific pulse sequences (multiple-quantum MAS, MQMAS). A complete insight into the structure was performed for the sample $LaSrAl_3O_7$ for which density functional theory (DFT) calculations were performed. Results on this reference model were then used to understand the data obtained for the full series of Ga/Al samples.

In *Chapter 4* materials for application as cathodes in lithium batteries are considered. We considered the series of orthosilicates of general formula $Li_2Mn_{1-x}Fe_xSiO_4$ with x = 0, 0.25, 0.5, 0.75, 1. This series is a possible alternative to the well known family of $LiMn_{1-x}Fe_{1+x}PO_4$, as it offers a very high electrical capacity due to the presence of two lithium ions in the structure per formula unit available for the electrochemical process. Preliminary work was carried out on natural abundance samples prepared according to different synthesis techniques. This family of compounds is characterized by a huge variety of polymorphs which can be obtained by varying composition and synthesis conditions. The structural characterization is not trivial and the combined use of traditional long-range technique (diffraction) and local probe (solid state NMR) is mandatory. The NMR study of this family of compounds proved to be very challenging, due to the strong paramagnetic interaction related to the presence of transition metal ions. In order to improve the sensitivity of the NMR experiments, isotopic enrichment of ^{29}Si was thus performed. The combined use of ^{29}Si labeling, medium-high magnetic fields, ultra

fast MAS and pulse sequences based on adiabatic pulses allowed us to obtain resolved spectra of ^{7}Li and ^{29}Si.

The main points and conclusions of the work presented in the previous chapters are given in the *Conclusions* together with the prospective of the NMR techniques applied to complex systems.

The three-year work of this Ph.D. project has been carried out between the Dipartimento di Chimica of the Università degli Studi di Pavia, Italy where synthesis procedure, preliminary structural (NMR, XRD) analysis and calculations were performed, and the Centre RMN à Très Haut Champ of the École Normale Supérieure de Lyon, France where NMR measurements were collected and analyzed.

Chapter 1

Introduction

Solid State Nuclear Magnetic Resonance (*ssNMR*) spectroscopy is a very powerful tool for chemical analysis to investigate structures, dynamics and interactions of a wide variety of different systems (biomacromolecules, amorphous systems, polymers, crystal inorganic materials, small organic molecules..). The growing importance of this technique is due to the continuous and great developments in sample preparations, tremendous engineering advances in probe and magnet technology, increase in the field strengths available, *RF* irradiation sequences together with the great flexibility and versatility of *ssNMR*.
This chapter is mainly concerned with the basic description of nuclear spin system, the interactions of such system with an external magnetic field and other sources of local magnetic fields and the Hamiltonian that can describe these interactions, introducing all the quantities necessary for the description of the system. The last part of the chapter will be devoted to the description of the techniques used to study and analyze the different systems focusing the attention on methods for quadrupolar and paramagnetic systems.

1.1 - THE QUANTUM-MECHANICAL MODEL

For a nucleus it is possible to define the nuclear spin angular momentum *I*, and associated to this, a nuclear magnetic moment μ . The magnetic moment is related to the spin angular momentum according to the relation

$$\mu = \gamma \hbar I \quad \text{with } |\mu| = |\gamma| \hbar \sqrt{I(I+1)} \qquad (1.1)$$

where γ is the nuclear gyromagnetic ratio [rads^{-1} T^{-1}] defined as

$$\gamma = \frac{q}{2m} \tag{1.2}$$

where q is the charge and m is the mass of the nucleus.
If the moment is inclined at an angle Θ with respect to the applied external magnetic field B, the nucleus is characterized by a motion of precession at a constant angle Θ about B at a constant angular frequency ω according to the Larmor equation

$$\omega = -\gamma B \tag{1.3}$$

In NMR the external magnetic field is usually referred as B_0 and is taken to be along the z positive axis in the laboratory frame reference system (*LFR*), *i.e.* B_0 = (0 0 B_0). The frequency of precession is called *Larmor frequency* and is defined as

$$\omega_0 = -\gamma B_0 \tag{1.4}$$

The definition of the Larmor frequency is given by the Larmor equation but the term is often used to refer to the direct frequency that is of more immediate experimental relevance, $\nu_0 = \omega_0/2\pi$.
The energy of the interaction of the nucleus with the external applied magnetic field is defined by the equation

$$E = -\mu B_0 \tag{1.5}$$

In a quantum-mechanical picture the energies and the energy levels in a system are given by the time-dependent Schrödinger equation

$$i\hbar \frac{\partial \Psi}{\partial t} = H \Psi \tag{1.6}$$

Where H is the Hamiltonian, the total energy operator and Ψ is the wave function.
In the NMR experiment the system is interrogated by the use of radio-frequency (*RF*) pulses that are assumed not to change or modify the energy levels of the systems. Thus it is possible to

assume that the Hamiltonian is time-independent and consider the relative Schrödinger equation

$$H\varphi = E\varphi \tag{1.7}$$

Where φ is the time independent wave function related to Ψ according to the relation

$$\Psi = \varphi \exp\left(-iEt/\hbar\right) \tag{1.8}$$

The Hamiltonian gives all the possible energy levels of the systems: electronic transitions, rotations, vibrations, etc. NMR energy levels splitting is in the order of magnitude of ~10^{-6} eV (~ hundreds of MHz) and is considerably different from energy splitting involved in other interactions to be considered separately and independently from other terms that can be ignored. From this point all the Hamiltonian equations will be related only to the nuclear spins, considering valid the Born-Oppenheimer approximation.

It is possible to introduce a complete set of orthogonal spin functions φ_n as the basis set for the definition of any eigenfunction φ of the considered Hamiltonian. In this way any eigenfuntion can be rewrite as a linear combination of the spin functions

$$\varphi = \sum_n C_n \varphi_n \tag{1.9}$$

Where the coefficient C_n is different for different interactions. In the NMR experiment the φ_n can be identify by the quantum numbers I and m where I is the already mentioned spin quantum number and m is the z-component of I with possible values given my $m = -I, -I+1 \ldots 0..I-1,I$. The state of a nucleus is thus define by the pair of the quantum number I and m and it is usually reported as $|I, m\rangle$ with Dirac notation.According to this approach each individual nucleus is considered, and from this starting point the properties of the whole system are derived as an *average ensemble*.

To determine any physical property of the system, an operator has to be used. In particular, to define the total energy of the system, the total energy Hamiltonian operator $\hat{H}$ is defined. Apart from the external magnetic field, there are different sources of magnetic fields into the sample, which affect the nuclear spin system and thus the final *eigenstates* and related energies.

1.2 – GENERAL EXPRESSION FOR THE NUCLEAR INTERACTIONS

By means of the quantum-mechanical picture it is possible to consider all the interactions of one nuclear spin with the other magnetic sources. The general Hamiltonian of the system is thus described as a sum of different individual terms that can be considered singularly

$$\hbar\widehat{H}_{TOT} = \hbar \sum_{i} \widehat{H}_{loc,i} \tag{1.10}$$

Each term in the Hamiltonian can be represented as the interaction of the nuclear magnetic momentum I of the *i-th* nucleus with a local magnetic field $B_{loc,m}$. The source of the local magnetic field determines the characteristic of the interaction

$$\hbar\widehat{H}_{TOT} = \hbar \sum_{m,i} -\gamma k_m \hat{I}_i B_{loc,m} \tag{1.11}$$

$$B_{loc,m} = A^{m}_{loc,ij} J^{m}_{j} \tag{1.12}$$

The local field $B_{loc,m}$ is a linear vector, k_m is a constant peculiar for each interaction, $A^{m}_{loc,ij}$ is a 3x3 second-rank Cartesian tensor, called *coupling tensor* as it describes (strength and orientation) the interaction between the *i-th* nuclear spin I and the source of the local field J_j; thus in turn it defines the anisotropy of the interactions. J_j is a vector that is the source of the magnetic field. (another nucleus, another local field, an unpaired electron, etc.).

Thus, the general contribution to the global Hamiltonian can be written as

$$\hat{H}_{loc} = -\gamma\, \hat{I}\, B_{loc} = \hat{I}\, A_{loc}\, J \tag{1.13}$$

It is also possible to use a frame in which the tensor has only diagonal elements, this is called the principal axis frame (*PAF*). It will be possible to pass from the *PAF* to most useful frames, according to the various specific cases, using rotation operators $R(\Theta, \Phi)$

$$\begin{pmatrix} \hat{I}_x \\ \hat{I}_y \\ \hat{I}_z \end{pmatrix} = R(\Theta, \Phi) \begin{pmatrix} \hat{I}_{x,PAF} \\ \hat{I}_{y,PAF} \\ \hat{I}_{z,PAF} \end{pmatrix} \tag{1.14}$$

1.3 – CARTESIAN AND SPHERICAL FORMALISM

The anisotropy of the spin interactions can be efficiently expressed with the use of 3X3 Cartesian tensors presented above as it can give the direct physical description of the interaction. In particular, three quantities are usually reported: isotropic value A_{iso}, anisotropy Δ_A and asymmetry η, defined according to the expressions

$$A_{iso} = \frac{1}{3}\left(\mathrm{A}_{xx}^{PAF} + \mathrm{A}_{yy}^{PAF} + \mathrm{A}_{zz}^{PAF}\right) \tag{1.15}$$

$$A = A_{zz}^{PAF} - \mathrm{A}_{iso} \tag{1.16}$$

$$\eta = \frac{A_{xx}^{PAF} - A_{yy}^{PAF}}{\Delta_A} \tag{1.17}$$

The nine components of the Cartesian second-rank tensor can be also expressed as the sum of three different irreducible tensors: the scalar A_0, the anti-symmetric tensor A_1 and the symmetric tensor A_2

$$A_{ij} = A_0 + A_1 + A_2$$
$$\frac{1}{3} Tr\{A_{ij}\} + A'_{ij} + A''_{ij} \tag{1.18}$$

where

$$A_0 = \frac{1}{3} Tr\{A_{ij}\} = \frac{1}{3} \sum_i A_{ii} \tag{1.19}$$

$$A_1 : A'_{ij} = \frac{1}{2} (A_{ij} - A_{ji}) \tag{1.20}$$

$$A_2 : A''_{ij} = \frac{1}{2} (A_{ij} + A_{ji}) - \frac{1}{3} Tr\{A_{ij}\} \tag{1.21}$$

In the following discussion it will be convenient the use of different reference axes systems for different interactions and thus rotation operations are needed together with other punctual operations.

When tensors need to be expressed into a new coordinates system related to the old one by an operation of rotation about the Euler angles (α, β, γ) it is more convenient to express the tensors with the use of spherical tensor formalism.

A second rank tensor A_k can be decomposed into three irreducible spherical tensors in terms of the Cartesian tensor according to relations 1.22

$$A_{00} : A_{00} = -\left(1/\sqrt{3}\right)[A_{xx} + A_{yy} + A_{zz}]$$
$$A_{10} : A_{00} = -\left(i/\sqrt{2}\right)[A_{xy} - A_{yx}]$$
$$A_{1\pm1} : A_{1\pm1} = -(1/2)[A_{zx} - A_{xz} \pm i(A_{zy} - A_{yz})] \tag{1.22}$$
$$A_{20} : A_{20} = \left(1/\sqrt{6}\right)[3A_{zz} - (A_{xx} + A_{yy} + A_{zz})]$$

$$A_{2\pm1}: A_{2\pm1} = \pm(1/2)[A_{xz} + A_{zx} \pm i(A_{yz} + A_{zy})]$$

$$A_{2\pm2}: A_{2\pm2} = (1/2)[A_{xx} - A_{yy} \pm i(A_{xy} + A_{yx})]$$

Interaction	$A_{\alpha\beta}$ ***(α,β = x, y, z)***	A_{kq}
Chemical shift	$\gamma\sigma_{\alpha\beta}$	$A_{00} = -\frac{1}{\sqrt{3}}\begin{pmatrix} A_{xx} + A_{yy} \\ +A_{zz} \end{pmatrix} = -\frac{1}{\sqrt{3}} Tr\{A_{\alpha\beta}\}$
Dipole-dipole	$D_{\alpha\beta}$	$A_{10} = -\frac{i}{\sqrt{2}}(A_{xy} - A_{yx})$
J- coupling	$J_{\alpha\beta}$	$A_{1\pm1} = -\frac{1}{2}\begin{bmatrix} A_{zx} - A_{xz} \\ \pm i(A_{zy} - A_{yz}) \end{bmatrix}$
Spin rotation	$C_{\alpha\beta}$	$A_{20} = \frac{1}{\sqrt{6}}\begin{bmatrix} 3A_{zz} \\ -(A_{xx} + A_{yy} + A_{zz}) \end{bmatrix}$
Quadrupole	$\frac{eQ}{2I(2I-1)\hbar} V_{\alpha\beta}$	$A_{2\pm1} = \pm\frac{1}{2}\begin{bmatrix} A_{xz} + A_{zx} \\ \pm i(A_{yz} + A_{zy}) \end{bmatrix}$ $A_{2\pm2} = \frac{1}{2}\begin{bmatrix} A_{xx} - A_{yy} \\ \pm i(A_{xy} + A_{yx}) \end{bmatrix}$

Table 1.1 – Relation between Cartesian tensor and spherical tensor for the different spin interactions.[1]

In some particular cases the definition of the tensors is simplify: when the Cartesian tensor is symmetric and the trace is zero only the second rank irreducible tensor is non zero. This is, for

example, the case of dipolar and quadrupolar interactions while the chemical shift tensor has a non-zero trace.
As already mentioned, the Hamiltonians term of spin interactions have general formula

$$H = X\,A\,Y = \sum_{i,j} A_{ij} X_i\, Y_j \qquad (1.23)$$

Where X, Y are vectors representing the spins and A the coupling matrix. It is possible to express X_i and Y_j as a unique tensor T_{ij} considering the dyadic product

$$T_{ij} = Y_j X_i \qquad (1.24)$$

This is possible to rewrite the spin interaction Hamiltonian in terms of irreducible spherical tensors

$$H = \sum_{k=0}^{2} \sum_{q=-k}^{+k} (-1)^q\, A_{kq} T_{k-q} = A_k T_k \qquad (1.25)$$

Where the spherical tensor components A_{kq} and T_{kq} can be expressed in terms of Cartesian tensor component according to relations reported in Tables 1.1 and 1.2.

The A_{kq} is a tensor due to lattice variables. This notation is particularly useful when rotations or other unitary transformations are performed.
To clarify the differences between the two notations it is possible to consider that while in the Cartesian formalism the different terms of the Hamiltonian are arranged according to the references axis, in the spherical notation the terms of the Hamiltonian are arranged according to their rotational symmetry.

Interaction	T_{00}	T_{10}	$T_{1\pm1}$	T_{20}	$T_{2\pm1}$	$T_{2\pm2}$
Chemical shift	$-\frac{1}{\sqrt{3}} I_z B_0$	0	$-\frac{1}{2} I_\pm B_0$	$\sqrt{\frac{2}{3}} I_z B_0$	$\pm\frac{1}{2} I_\pm B_0$	0
Dipole-dipole	0	0	0	$\frac{1}{\sqrt{6}}(3I_zS_z - \boldsymbol{I} \cdot \boldsymbol{S})$	$\pm\frac{1}{2}(I_zS_\pm + I_\pm S_z)$	$\frac{1}{2} I_\pm S_\pm$
J-coupling	$-\frac{1}{\sqrt{3}} I \cdot S$	$-\frac{1}{2\sqrt{2}}(I_+S_- - I_-S_+)$	$+\frac{1}{2}[I_zS_\pm - I_\pm S_z]$	$\frac{1}{\sqrt{6}}(3I_zS_z - \boldsymbol{I} \cdot \boldsymbol{S})$	$\pm\frac{1}{2}(I_zS_\pm + I_\pm S_z)$	$\frac{1}{2} I_\pm S_\pm$
Spin rotation	$-\frac{1}{\sqrt{3}} I \cdot J$	$-\frac{1}{2\sqrt{2}}(I_+J_- - I_-J_+)$	$+\frac{1}{2}[I_zJ_\pm - I_+J_z]$	$\frac{1}{\sqrt{6}}(3I_zJ_z - \boldsymbol{I} \cdot \boldsymbol{J})$	$\pm\frac{1}{2}(I_zJ_\pm + I_\pm J_z)$	$\frac{1}{2} I_\pm J_\pm$
Quadrupole	0	0	0	$\frac{1}{\sqrt{6}}(3I_z^2 - I(I+1))$	$\pm\frac{1}{2}(I_zI_\pm + I_\pm I_z)$	$\frac{1}{2} I_\pm I_\pm$

Table 1.2 – Spherical tensor representation of spin operators.[1]

1.4 – THE NMR HAMILTONIAN

The total interaction energy of a nucleus can be seen as the result of the sum of all the individual contributions experienced by the nucleus. These interactions are represented in the total Hamiltonian

$$H_{tot} = H_Z + H_{RF} + H_{CS} + H_D + H_J + H_Q + H_P + H_{exp} \qquad (1.26)$$

That include the H_Z Zeeman interaction between the nucleus and the external field, the interaction H_{RF} between the nucleus and the applied *RF* pulse, the chemical shielding H_{CS} defining the interaction between the nucleus and the local change in the magnetic field due to changes in electron density, the dipolar coupling trough space H_D between two nuclei, the indirect spin coupling H_J that defines the interaction trough bonds of the nuclei, the electric quadrupole interaction H_Q that affects the Zeeman energy level although it is an electric effect, the interaction with unpaired electrons H_P. H_{exp} accounts for experimental inhomogeneities and other minor sources of local fields.
It is possible to discriminate between external and internal interactions. External interactions are the interactions of the nuclei with external sources of magnetic fields, such as the applied magnetic field B_0 and the magnetic field B_1 of the *RF* pulses; the internal interactions refer to interactions between nuclei and sources of magnetic field internal and intrinsic in the sample, *i.e.*, local magnetic fields generated by other nuclei, electrons etc.
It is generally the case that

$$H_{ext} \gg H_{int} \qquad (1.27)$$

As far as this condition is valid, and particularly that the Zeeman interaction with the external applied magnetic field B_0 is the dominant interaction, it is possible to consider the z axis of the field B_0 as the quantization axis for the energy level of the

investigated system, *i.e.* the internal interactions can be considered a perturbation to the Zeeman interaction.

H_m	*Interaction*	$A^m_{loc,ij}$	J_j	*Size (Hz)*	*Description*
H_Z	Zeeman	*1*	B_0	10^7-10^9	Interaction with main external magnetic field
H_{RF}	Zeeman	*1*	B_1	10^3 - 10^5	Interaction with the applied RF field
H_D	Dipolar	*D*	I	10^3-10^4	Spin-spin interaction through space
H_{CS}	Chemical shielding	σ	B_0	10^2-10^5	Local magnetic field altered by electron density
H_J	Spin spin	*J*	I	10^0-10^2	Spin-spin interaction through chemical bonds
H_Q	Quadrupolar	*eq*	I	10^3-10^7	Interaction of quadrupolar momentum with the local electric field gradient
H_P	Paramagnetic	*P*	S	10^2-10^5	Interaction with unpaired electrons

Table 1.3 – NMR interactions, description and order of magnitude of the strength of the effect.[2]

All these terms contribute in a different way to the global Hamiltonian. Each interaction arises from a peculiar effect and thus has a peculiar effect on the NMR spectra as far as concerns the intensity, shape and position of the NMR line. A detailed description of each term is needed in order to fully understand the observed NMR line.

1.4.1 - The Zeeman term, $\widehat{H}_z$

Considering an isolated spin μ in the static uniform magnetic field B_0 the related Hamiltonian that defines the interaction can be written as

$$\hat{H}_Z = -\hat{\mu} B_0 \tag{1.28}$$

Where $\hat{\mu}$ is the magnetic momentum operator and B_0 the external magnetic field. This is usually called *Zeeman Hamiltonian* and can be rewritten using the definition of the quantum magnetic momentum $\hat{\mu}$

$$\hat{\mu} = \gamma\hbar\hat{I} \tag{1.29}$$

$$\hat{H} = -\gamma\hbar\hat{I} B_0 \tag{1.30}$$

$$\hat{\mathrm{H}}|\mathrm{I},\mathrm{m}> = \mathrm{E}_{\mathrm{I,m}}\,|\mathrm{I},\mathrm{m}> \tag{1.31}$$

The *eigenfunction* of $\hat{H}$ are wavefunctions describing all the possible states of the spin system within the magnetic field. The energies related of the *eigenstates* are defined as

$$E_{I,m} = -\gamma\hbar B_0 m \tag{1.32}$$

For a spin I = ½ there are two states and the energy difference ΔE between thems is equal to $-\gamma\hbar B_0$. In frequency units it correspond to

$$\omega_0 = \gamma B_0 \tag{1.33}$$

That is the already mentioned Larmor equation.

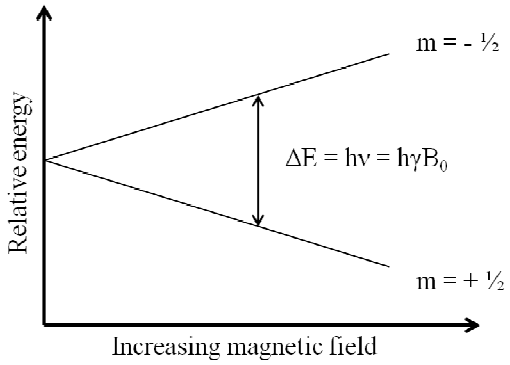

Figure 1.1 – Schematic representation of the relation between the energy separation between nuclear energy levels and the strength of the applied magnetic field.

In a NMR experiment the applied static magnetic field is order of magnitude larger than any other local interaction so the B_0 remains the quantization axis for the nuclear spin system and many of the other interactions are negligible respect to this main field. The only components of local interactions that will have effect on the spin state are:

- component parallel or antiparallel to the applied magnetic field B_0;
- component preceding in the plane orthogonal to the applied field at frequency near to the Larmor frequency (as the applied RF field).

1.4.2 - The RF term, $\hat{H}_{RF}$

The application of a radio-frequency, *RF*, pulse introduces an oscillating magnetic field $B_1(t)$ in the spin system. The interaction between the nuclei and the external field B_1 is the same of the

interaction with B_0 described above; the main difference is the time-dependence of the applied field. This implies that both the eigenstates and the eigenvalues of the spin systems are time dependent. It is possible to express the eigenstates of the time dependent Hamiltonian as linear combinations of the Zeeman states defined previously for the system in a static field B_0. The Hamiltonian describing the interaction with the external magnetic field must consider the sum of these two contributions

$$B_{tot}(t) = i\, 2B_1 cos(\omega_{RF} t) + \; k\, B_0 \qquad (1.34)$$

Where i and k are unit vector in the direction of x and z axis respectively. Thus the Hamiltonian describing the interaction between the nucleus I and the field B is given by

$$\widehat{H} = \; -\hat{\mu} \cdot B = \; -\gamma \left(\hat{I}_z B_0 + \hat{I}_x B_1 cos(\omega_{RF} t) \right) \qquad (1.35)$$

It is possible to consider the B_1 field as a sum of two counter-rotating components rotating at the same frequency but in opposite directions. Only the component with frequency similar to the Larmor value and rotating in the same sense has an effect on the spin because the resonance condition is matched. The counter component that rotats in the opposite direction of the preceding Larmor frequency can be neglected as it is in a non-resonant condition and thus has no effect on the spin

$$\widehat{H} = -\gamma \left(\hat{I}_z B_0 + B_1 e^{-i\omega_{RF} t \hat{I}_z} \hat{I}_z e^{+i\omega_{RF} t \hat{I}_z} \right) \qquad (1.36)$$

In order to find the eigenfunctions for this system, it would be necessary to use the time-dependent Schrödinger equation; to avoid this passage it is possible to remove the time dependence from the Hamiltonian by transforming the reference axes frame into a new rotating frame, *RoF*, identical to the old one but rotating about B_0 with constant rate ω_{RF}. In this new frame the Hamiltonian becomes $\widehat{H'}$ defined as

$$\widehat{H'} = (\gamma B_0 - \omega_{RF})\hat{I}_z + \gamma B_1 \hat{I}_x \quad (1.37)$$

And the corresponding wave functions

$$\Psi' = e^{+i\omega_{RF}t\hat{I}_z}\,\Psi \quad (1.38)$$

Where $e^{+i\omega_{RF}t\hat{I}_z}$ is the rotating operator necessary to rotate the spin coordinate axis frame by angle $\omega_{RF}t$. The time dependence is then incorporated in the reference system; the effect of the *RF* pulse is to flip the magnetization from the *z*-axis to the *xy* plane.

1.4.3 - The shielding and chemical shift term, $\widehat{H}_{CS}$

The exact resonance frequency depends on the chemical environment at the site of the nucleus as the resonance frequency is extremely sensitive to the actual magnetic field. The external magnetic field has an effect also on the electrons that surround a nucleus; their motion and polarization create a supplemental local magnetic field. This secondary field sums over the B_0 experienced by the nucleus and finally changes the resonance frequency. The interaction of the secondary local field produced by electrons with the nucleus is called the *shielding interaction* and the frequency shift is called the *chemical shift*. The shielding interaction can be decomposed in two main contributions:

- *Diamagnetic contribution*. The external magnetic field causes circulation of electrons that consequently causes a magnetic field that is opposed to the principal one and so shields the nucleus. This contribution depends on the term $1/r_i^3$ where r_i is the distance between the nucleus and the *i*-th electron. For this reason the main contribution to the shielding comes from the inner core electrons. According to these considerations, the chemical shielding for an atom in a molecule is, at a certain extent, constant.

For a more precise analysis, also electrons of nuclei around the considered nucleus must be considered.

- *Paramagnetic contribution*. The external magnetic field creates also a distortion of the distribution of electrons that can be seen as a mixing of ground and excited states. Some of these excited states can be paramagnetic and introduce a certain degree of paramagnetism; this introduces a new local field that reinforces the external applied magnetic field and tends to de-shield the nucleus.

The chemical shielding Hamiltonian can be written as

$$\hat{H}_{CS} = \gamma \hat{\mathrm{I}} \cdot \sigma \cdot B_0 \qquad (1.39)$$

The ultimate source of the shielding is the external magnetic field, B_0 that thus correspond to the J_j of the general formula. The term σ is the second rank tensor called c*hemical shift tensor*, the $A^m_{loc,ij}$ coupling matrix; it defines the orientation of the electron density distribution respect to the nucleus.
It can be written as the sum of two contributions, the symmetric and the anti-symmetric components. It is useful to consider this decomposition as only the symmetric part of the tensor turns out to affect the NMR spectrum in a significant way.

It is possible to choose the axes frame in order to make the tensor σ diagonal. This is the principal axes frame, *PAF*, and the σ_{ii}^{PAF} are the principal axis components of the tensor. It is common to express the three main values of the tensor not as σ_{ii}^{PAF} but as the isotropic value σ_{iso}, the anisotropy Δ_{cs} and the asymmetry η_{cs} defined as

$$\sigma_{iso} = \frac{1}{3}\left(\sigma_{xx}^{PAF} + \sigma_{yy}^{PAF} + \sigma_{zz}^{PAF}\right) \qquad (1.40)$$

$$\Delta_{CS} = \sigma_{zz}^{PAF} - \sigma_{iso} \tag{1.41}$$

$$\eta_{CS} = \frac{\sigma_{xx}^{PAF} - \sigma_{yy}^{PAF}}{\Delta} \tag{1.42}$$

To deal with the chemical shielding Hamiltonian it is necessary to transform the spin coordinates into the already mentioned rotating frame, *R0F*, directed along the *z*-axis of the laboratory frame (the same axis of B_0) and rotating with a speed of ω_0, the Larmor frequency of the spin. After the transformation, the Hamiltonian is time-dependent and is difficult to manage. The best way to deal with it is considered the Average Hamiltonian Theory, *AHT*,[3] that approximates a periodic function as a sum of successive higher-order terms. In this approximation it is possible to consider only the average chemical shift Hamiltonian to the first order

$$\bar{H}_{CS}^{(0)} = \gamma \hat{I}_z \sigma_{zz}^{lab} B_0 \tag{1.43}$$

It is possible to calculate the relative energy and frequency of the total Hamiltonian

$$E_{cs} = \gamma \hbar \sigma_{zz}^{lab} B_0 m \tag{1.44}$$

$$\omega_{cs} = \gamma \sigma_{zz}^{lab} B_0 \tag{1.45}$$

To analyze in detail the expression of ω_{cs} it is necessary to express the σ_{zz}^{lab} in term of the principal value of the shielding tensor and the orientation of the *PAF* respect to the laboratory frame. Using the two angles Θ and Φ to define the direction of B_0 respect to the *PAF*, it is possible to rewrite the generic expression of ω_{cs}

$$\omega_{cs}(\theta, \Phi) = -\omega_0 \sigma_{iso} - \frac{1}{2}\omega_0 \Delta \begin{Bmatrix} 3cos^2\theta - 1 \\ +\eta sin^2\theta cos2\Phi \end{Bmatrix} \tag{1.46}$$

For the axial symmetry ($\sigma_{xx}^{PAF} = \sigma_{yy}^{PAF}$) it is possible to simplify

$$\omega_{cs}(\Theta) = -\omega_0 \sigma_{zz}^{PAF} \frac{1}{2}\{3cos^2\Theta - 1\} \qquad (1.47)$$

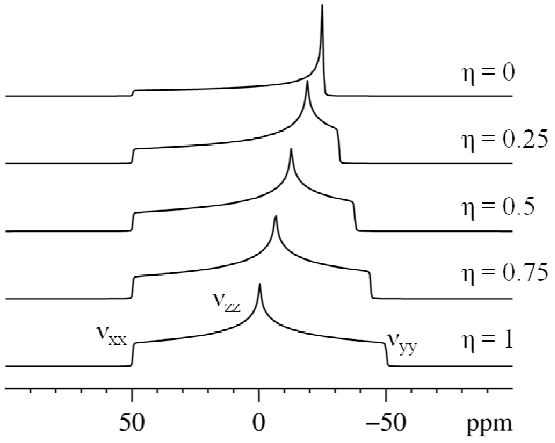

Figure 1. 2 – Typical chemical shift anisotropy powder pattern lineshape as function of the η parameters.

The effect of such interaction on a powder spectrum is relevant. In a powder sample all the possible molecular orientations are present and so all the possible Φ and Θ are represented. The spectrum will therefore reflects this situation and will be composed from the sum of all the contributions. The intensity of a certain frequency is proportional to the number of molecules with that specific orientation. The spectral shape is thus very distinctive of the symmetry of the shielding tensor and so in the end of the symmetry at the nucleus site, as shown in Figure 1.2.

An alternative way to re-express the H_{CS} terms can be considered using the spherical tensor formalism, considering the transformation from the Cartesian formalism reported in Table 1.1

and 1.2; this could be very useful to consider the effect of MAS rotation on the experimental lineshape.

1.4.4 - The scalar coupling term, $\hat{H}_J$

The scalar coupling (spin–spin coupling or J coupling) is the indirect interaction of nuclear moments mediated trough electrons involved in chemical bonds between the considered nuclei. The first nucleus creates a perturbation in surrounding electrons, this perturbation generates a local magnetic field at the site of the second nucleus. This interaction is different from the dipolar interaction because the mechanism is based on the presence of a chemical bond, it is not trough space, thus is relevant in covalent compounds and is strongly dependent on lenght and angles of the involved chemical bonds.
The Hamiltonian is given by

$$\hat{H}_J = h\, J_{12} \hat{I}_1 \hat{I}_2 \qquad (1.48)$$

J_{12} is the spin- spin coupling constant in Hz. The source of this coupling could be spin-orbital, spin-dipolar or Fermi contact. The Hamiltonian H_J does not shown any dependence from B_0.
Scalar coupling is orientation dependent, thus a tensor is needed for its description. This interaction can be neglected in solids, except that in case of paramagnetic hyperfine coupling (see Paragraph 1.4.7). In liquids, in contrast, J-coupling is a powerful tool to investigate the network of local spin and study the local fragments of large molecules (e.g. proteins).[2]
The magnitude of scalar coupling depends on the degree of covalence of bonds involved, number of bonds, gyromagnetic ratio, degree of orbital overlap.
J should be described by a tensor so that the anisotropy can be defined as

$$\Delta J = J - J_{\perp} \qquad (1.49)$$

So the complete Hamiltonian is

$$\hat{H}_J = J\,\hat{I}_z\hat{S}_z + \frac{\Delta J}{3}\left[3\hat{I}_z j_z(\hat{S}\cdot j) - \hat{I}_z\hat{S}_z\right] \qquad (1.50)$$

As *J*-coupling is usually considered to be directed along the inter-nuclear vector about which the tensor is probably axially symmetric, J_z is the projection of the unique axes of the *J* tensor onto the *z*- direction.

1.4.5 - The dipolar term, $\hat{H}_D$

Each nucleus with an associated nuclear spin *I* has a magnetic moment and generates a local magnetic field that is experienced by the other near nuclei. This interaction that occurs trough space is the magnetic dipole-dipole coupling. In solution this interaction is averaged to zero (it has no isotropic value) by random molecular tumbling, whereas in solid systems it is one of the major causes of line-broadening. The dependence of this interaction from distance is scaled as $1/r^3$ where *r* is the inter-nuclear distance and depends on the relative positions of the interacting spins. In a classical picture the dipole-dipole interaction *U* can be defined as

$$U = \left\{\frac{\mu_1\mu_2}{r^3} - 3\frac{(\mu_1 r)(\mu_2 r)}{r^5}\right\}\frac{\mu_0}{4\pi} \qquad (1.51)$$

Where *r* is again the inter-atomic distance between the two magnetic dipoles μ_1 and μ_2. In a quantum-mechanical picture the magnetic moment operator $\hat{\mu}$ for the nuclear spin *I* is considered

$$\hat{\mu} = \gamma\hbar\hat{I} \qquad (1.52)$$

So it is possible to define the Hamiltonian for the dipole-dipole interaction between spin *I* and spin *S*

$$\widehat{H}_{dd} = -\frac{\mu_0}{4\pi}\gamma_I\gamma_S\hbar\left\{\frac{\hat{I}\hat{S}}{r^3} - 3\frac{(\hat{I}\cdot r)(\hat{S}\cdot r)}{r^5}\right\} \qquad (1.53)$$

It is also possible to rewrite the equation:

- in spherical polar coordinates

$$\widehat{H}_{dd} = -\frac{\mu_0}{4\pi}\frac{\gamma_I\gamma_S\hbar}{r^3}[A+B+C+D+E+F]$$

$$A = \hat{I}_z\hat{S}_z(3cos^2\Theta - 1)$$

$$B = -\frac{1}{4}\left[\hat{I}_+\hat{S}_- + \hat{I}_-\hat{S}_+\right](3cos^2\Theta - 1)$$

$$C = -\frac{3}{2}\left[\hat{I}_z\hat{S}_+ + \hat{I}_+\hat{S}_z\right](sin\Theta cos\Phi e^{-i\Phi}) \qquad (1.54)$$

$$D = -\frac{3}{2}\left[\hat{I}_z\hat{S}_- + \hat{I}_-\hat{S}_z\right](sin\Theta cos\Phi e^{+i\Phi})$$

$$E = \frac{3}{4}\left[\hat{I}_+\hat{S}_+\right](sin^2\Theta e^{-2i\Phi})$$

$$F = \frac{3}{4}\left[\hat{I}_-\hat{S}_-\right](sin^2\Theta e^{+2i\Phi})$$

Where $\hat{I}_+\hat{S}_+$ and $\hat{I}_-\hat{S}_-$ are the raising and lowering operators for spin *I* and *S*, and Φ and Θ are the polar angles defining the relative orientation of the vector between *I* and *S* respect to the external magnetic field B_0.

- Cartesian tensorial form

$$\widehat{H}_{dd} = -2\hat{I}\,D\,\hat{S} \qquad (1.55)$$

The spin *S* is the ultimate source of the local magnetic field at the spin *I*. The interaction is defined thank to the tensor *D* with principal values of $-d/2$, $-d/2$, $+d$ where *d*, the dipolar coupling constant, defined as

$$d = \hbar\left(\frac{\mu_0}{4\pi}\right)\frac{1}{r^3}\gamma_I\gamma_S \tag{1.56}$$

The tensor *D* describes the orientation dependence of the *I-S* interaction respect to the applied field. *I* and *S* are quantized angular momenta along B_0 and they generate a local field that, in turns, depend on the orientation respect of B_0.

The dipolar coupling tensor is traceless, there is no isotropic component so when the dipolar interaction is averaged by molecular motion in solution it is averaged to zero. This tensor is always symmetric in its *PAF* with the unique axis directed along the *I-S* vector.
As for other interactions, in order to study the effects of dipolar-coupling on NMR spectrum it is necessary to transform the Hamiltonian and to rewrite it in the rotating frame, thus is convenient to deal with the spherical form. The transformation is done by applying the rotation operator $\hat{R}_z(\omega_0 t)$ to the global Hamiltonian

$$\hat{H}_{tot} = \hat{H}_0 + \hat{H}_{dd} \tag{1.57}$$

The rotation about the *z* axis has no effect on the $\hat{H}_0$ term, and the second term has different forms considering different situations: *homonuclear coupling* (dipolar coupling between two identical spins) and *heteronuclear coupling* (dipolar coupling between two different nuclear species).

- Homonuclear coupling

$$\widehat{H^*}_{(t)HOM} = -d\,\{[A + B] + \hat{R}_z^{-1}(\omega_0 t)\,[C + D + E + F]\,\hat{R}_z(\omega_0 t)\} \tag{1.58}$$

- Heteronuclear coupling

$$\widehat{H^*}_{(t)HET} = -d\{[A] + \hat{R}_z^{-1}(\omega_0 t)\,[B + C + D + E + F]\,\widehat{R}_z(\omega_0 t)\} \tag{1.59}$$

For the homonuclear coupling the terms A and B are unaffected by the rotation transformation, differently from heteronuclear coupling for which only the term A remains the same. Applying the average Hamiltonian theory it is possible to obtain the dipolar coupling contribution to the first order average Hamiltonian in the rotating frame

- Homonuclear coupling:

$$\widehat{H}_{dd}^{HOMO} = -d \cdot \frac{1}{2}(3cos^2\Theta - 1)\left[3\hat{I}_z\hat{S}_z - \hat{I}\hat{S}\right] \tag{1.60}$$

- Heteronuclear coupling:

$$\widehat{H}_{dd}^{HETERO} = -d(3cos^2\Theta - 1)\hat{I}_z\hat{S}_z \tag{1.61}$$

The $\hat{I}_z\hat{S}_z$ term causes a first-order change in energy, so an energy shift of the nuclear spin levels. The term $\hat{I}\hat{S}$ has the effect of mixing the degenerate Zeeman states. The *eigenfunctions* of the system will consist in linear combinations of degenerate Zeeman levels. The homonuclear spectrum will be very broad resulting from a huge range of transition frequencies.
In the case of heteronuclear coupling, the term B is not relevant to the first order, so there is no mixing of the Zeeman states. The effect of the heteronuclear coupling between two different spins is similar to the effect of axial chemical shift anisotropy. As there is no mixing of the Zeeman states, it is possible to calculate the transition frequency for I and S spins in the coupled system IS

$$\omega_{dd}^I(\Theta) = \omega_0^I \pm \frac{1}{2}d(3cos^2\Theta - 1) \tag{1.62}$$

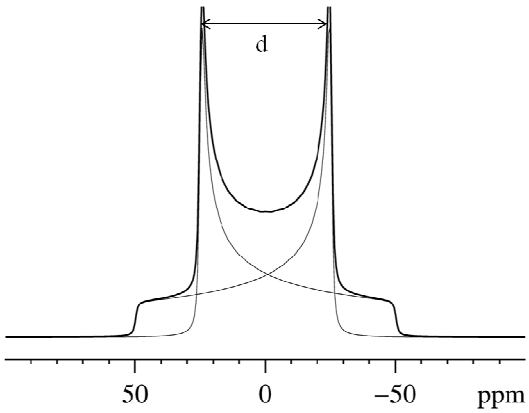

Figure 1.3 –Dipolar lineshape for a powder sample; the dipolar coupling constant can be measured from the splitting of "horns" of the Pake doublet. The horn shape is created by crystallite for which the I-S internuclear vector is perpendicular to direction of the applied magnetic field.

There are two transitions *I-S* with the same dependence on Θ so for the powder sample each of them gives origin to the typical powder pattern of the axial chemical shift anisotropy; the two transitions are symmetric so the spectrum is composed of two mirror peaks both centered at the same isotropic frequency, as reported in Figure 1.3.

1.4.6 - The quadrupolar term, $\widehat{H}_Q$

About ¾ of the NMR active nuclei have a nuclear spin higher than ½ and therefore possess an electric quadrupolar momentum that interacts with the electric field gradient around the nucleus. The electric quadrupole momentum arises from the distribution of the positive charge in the nucleus. In order to define the distribution of charge in a nucleus it is not sufficient to express the

total charge, it is necessary to expand the charge distribution function as a series of multipoles in which the zeroth-order term is the total charge, the first-order term is the electric dipole, the second-order term is the electric quadrupole, and so on.

As stated, the quadrupole momentum interacts with the electric field gradient around the nucleus. This interaction has the effect of changing the nuclear spin levels energies and is summed over the other interactions already described. The strength of this interaction depends on the nuclear quadrupolar momentum (a property of each isotope) and on the strength of the electric field gradient, *EFG* (a property of the sample). It is important to stress that B_0 can be still considered the quantization axis only if the Zeeman interaction is considerably stronger and dominant with respect to the quadrupolar interaction ($H_z \sim 10H_Q$). If this condition is respected it is still possible to define spin levels using quantum number I and m. This is not always the case because for some nuclei, ^{87}Rb and ^{14}N for example,[2] the quadrupolar interaction is so strong to be of the order of magnitude of the Zeeman interaction. In this and following chapters, only cases where the hypothesis for which the H_z is the dominant interaction are considered, so H_Q can always be treated with the perturbation theory[4] or with the Average Hamiltonian Theory.[5,6] The use of the *AHT* leads to a more compact operator form of the Hamiltonian and thus will be use in the following discussion. Extensive discussion on the background for the quadrupolar interaction can be found in literature. [6-8,10]

The dipolar electric momentum interacts with the external applied magnetic fields and orientates respect to B_0 in order to minimize the energy. The dipole and quadrupole electric momenta are fixed with respect to the nuclei so as the dipole momentum orientates with B_0, also the quadrupolar momentum assumes a specific and defined orientation with respect to the external field even if there

is no a direct magnetic interaction between the electric quadrupole moment and the magnetic field.

The quadrupolar Hamiltonian is defined as

$$\hat{H}_Q = \frac{eQ}{2I(I-1)\hbar}\,\hat{I}\,V\,\hat{I} \tag{1.63}$$

Where e is the proton charge, Q the quadrupolar momentum, I is the nuclear spin momentum and V is the electric field gradient at the nucleus defined as a second rank Cartesian tensor.
It is convenient to define the parameters

$$eq = V_{ZZ}^{PAF} \tag{1.64}$$

$$\eta_Q = \frac{V_{XX}^{PAF} - V_{YY}^{PAF}}{V_{ZZ}^{PAF}} \tag{1.65}$$

η_Q is called the asymmetry parameter, eq is the anisotropy parameter of the *EFG* tensor. The trace of the *EFG* tensor is null so there is no isotropic component.
Rewriting the quadrupole Hamiltonian in the *PAF*, and bearing in mind that the *EFG* is traceless, it becomes simply:

$$\hat{H}_Q = \frac{e^2qQ}{4I(I-1)\hbar}\left[3\hat{I}_{z,PAF}^2 - \hat{I}^2 + \frac{1}{2}\eta_Q\left(\hat{I}_{x,PAF}^2 - \hat{I}_{y,PAF}^2\right)\right] \tag{1.66}$$

The term $e^2qQ/\hbar$ is known as the quadrupole-coupling constant, is often reported in units of rad Hz and called quadrupolar coupling constant, C_Q. This approach is correct but not very useful and easy to handle in NMR experiments.

It is necessary to re-express the equation in terms of the laboratory frame using rotation matrix $R(\Theta,\Phi)$ with Θ and Φ spherical polar angles defining the orientation of the laboratory frame respect to

the *PAF*. The expression for H_Q in the laboratory frame using linear combination of $\hat{I}_x, \hat{I}_y$ and $\hat{I}_z$ is

$$\begin{aligned}\widehat{H}_Q = \frac{e^2qQ}{4I(I-1)\hbar}\{&\frac{1}{2}(3cos^2\Theta-1)\left(3\hat{I}_z^2-\hat{I}^2\right)\\&+\frac{3}{2}sin\Theta cos\Theta\left[\hat{I}_z\left(\hat{I}_+ + \hat{I}_-\right)+\left(\hat{I}_+ + \hat{I}_-\right)\hat{I}_z\right]\\&+\frac{3}{4}sin^2\Theta\left(\hat{I}_+^2+\hat{I}_-^2\right)\}\\+\eta_Q\frac{e^2qQ}{4I(I-1)\hbar}\{&\frac{1}{2}cos^2\Phi[(3cos^2\Theta-1)\left(3\hat{I}_z^2-\hat{I}^2\right)\\&+(cos^2\Theta+1)\left(\hat{I}_+^2+\hat{I}_-^2\right)]\\&+\frac{1}{2}sin\Theta(cos\Theta cos2\Phi - i\,sin2\Phi)\left(\hat{I}_+\hat{I}_z+\hat{I}_z\hat{I}_+\right)\\&+(cos\Theta cos2\Phi - i\,sin2\Phi)\left(\hat{I}_-\hat{I}_z+\hat{I}_z\hat{I}_-\right)\\&+\left(i/4\right)sin2\Phi cos\Theta\left(\hat{I}_+^2-\hat{I}_-^2\right)\end{aligned} \qquad (1.67)$$

In the case of axial symmetry ($\eta = 0$) only the first term is non-zero, otherwise all the terms must be considered. From this equation it is clear that the matrix of H_Q in the Zeeman basis contains both diagonal and off-diagonal terms.

The quadrupolar Hamiltonian can be written in a more compact form as the scalar product of spin and spatial tensors

$$\widehat{H}_Q = \sum_{m=-2}^{2}(-1)^m R_{2,m}^{Q,lab}\, T_{2,-m} \qquad (1.68)$$

Where $T_{2,-m}$ are spherical tensor spin operator reported in Table 1.2 and $R_{2,m}^{Q,lab}$ are the spherical tensor components of the spatial part

of H_Q in the laboratory frame. In the *PAF* of the quadrupolar interaction it is possible to rewrite these latter terms in the form of

$$R_{2,0}^{Q,PAF} = \sqrt{\frac{3}{2}}\omega_Q^{PAF}$$
$$R_{2,\pm1}^{Q,PAF} = 0 \qquad (1.69)$$
$$R_{2,\pm2}^{Q,PAF} = \frac{\eta_Q \omega_Q^{PAF}}{2}$$

With ω_Q^{PAF} the quadrupolar splitting parameter in the *PAF* defined in terms of C_Q

$$\omega_Q^{PAF} = \frac{3\pi C_Q}{2I(2I-1)} \qquad (1.70)$$

To find the exact energies (*eigenstates* and the corresponding *eigenvalues*) it is necessary to diagonalize the matrix of H_Q in the Zeeman basis. In the hypothesis of Zeeman interaction being the dominant one, only the secular part of H_Q affects the energies of the spin states system. The non-secular part has only a small and negligible effect. So it is possible to obtain the approximate energies of the spin system with the use of the *AHT*. In the case of quadrupolar interaction, it is necessary to take into account corrections that cause energy changes less than ~1/10 of the Zeeman energies in that particular field. The first- and second-order energy corrections to the Zeeman levels found by perturbation theory are

$$E_m^{(1)} = \frac{e^2qQ}{4I(I-1)\hbar}(3m^2 - I(I+1))\frac{1}{2}[(3cos^2\Theta - 1) + \eta cos2\Phi sin^2\Theta] \qquad (1.71)$$

$$E_m^{(2)} = \frac{e^2qQ}{4I(I-1)\hbar}\frac{m}{\omega_0} \times \{-\frac{1}{5}(I(I+1)-3m^2)\left(3+\eta_Q^2\right)$$

$$+\frac{1}{28}(8I(I+1)-12m^2-3)\left[\left(\eta_Q^2-3\right)(3cos^2\Theta-1)\right.$$
$$\left.+6\eta_Q sin^2\Theta cos2\Phi\right]$$

$$+\frac{1}{8}(18I(I+1)-34m^2-5)[\frac{1}{140}(18-\eta^2)(35cos^4\Theta$$
$$-30cos^2\Theta+3)$$

$$+\frac{3}{7}\eta_Q sin^2\Theta(7cos^2\Theta-1)cos2\Phi+\frac{1}{4}\eta_Q^2 sin^4\Theta cos4\Phi]\} \quad (1.72)$$

Coming back to the expression of the quadrupolar Hamiltonian as product of spin and spatial tensors presented above it is possible to find the same result. Also in this case the time dependent quadrupolar Hamiltonian defined in the rotating frame can considered by the means of the *AHT* as a sum of infinite contributions. As already stated, the series can be truncated after two terms

$$H_Q = H_Q^{(1)} + H_Q^{(2)} \quad (1.73)$$

and express these terms as a products of spin and spatial parts

$$H_Q^{(1)} = R_{2,0}^{Q,lab} T_{2,0} \quad (1.74)$$

The first order Hamiltonian does not affect the frequencies of the symmetric transitions from $-m$ to $+m$ but does affect those of the satellite transitions. As it is defined by a spatial tensor of rank two, it is averaged by MAS rotations and thus can be ignored when the spinning speed largely exceeds the size of this term.

The second order quadrupolar term for spin I = 3/2 can be written as

$$H_Q^{(2)} = \frac{-\sqrt{10}}{5\omega_0}\left(4R_{2,-1}^{Q,lab}R_{2,1}^{Q,lab} + R_{2,-2}^{Q,lab}R_{2,2}^{Q,lab}\right)T_{3,0} + \frac{6}{5\omega_0}\left(R_{2,-1}^{Q,lab}R_{2,1}^{Q,lab} + R_{2,-2}^{Q,lab}R_{2,2}^{Q,lab}\right)T_{1,0} \quad (1.75)$$

With the use of Clebsch-Gordon coefficients the products of the second-order spatial tensor components can be re-ordered in order to highlight that the second order quadrupoalr Hamiltonian is the sum of terms of zeroth, second and fourth spatial rank l, $R_{l,0}^{QXQ,lab}$

$$H_Q^{(2)} = \frac{1}{5\omega_0}\left(\frac{12}{\sqrt{5}}T_{1,0} + 3\sqrt{2}\,T_{3,0}\right)R_{0,0}^{QXQ,lab} + \frac{1}{5\omega_0}\left(3\sqrt{\frac{2}{7}}T_{1,0} - 6\sqrt{\frac{5}{7}}T_{3,0}\right)R_{2,0}^{QXQ,lab} + \frac{1}{5\omega_0}\left(-9\sqrt{\frac{2}{35}}T_{1,0} - \frac{17}{\sqrt{7}}T_{3,0}\right)R_{4,0}^{QXQ,lab} \quad (1.76)$$

The term with spatial rank zero is orientation-indipendent and appears as the quadrupolar shift contribution; the second-rank term can be averaged by MAS, as discussed above and thus can be neglected in opportune conditions; the fourth rank tensor in only partially averaged by MAS (~ 7/18 of the static size) and it is the source of the residual quadrupolar anisotropic broadening. It is relevant to notice that this term affects all the transitions, non only the satellites. The effect on this term on each one of the energy levels is given by $< m_I| - 9\sqrt{\frac{2}{35}}T_{1,0} - \frac{17}{\sqrt{7}}T_{3,0}|m_I >$; it is possible to evaluate that the fourth rank contribution to the triple quantum and central transitions frequencies are in ratio -7:9. This can be

seen as the gradient of the ridge lineshapes obtained in triple quantum MQMAS, as discusses in the following part.

k	$T_{0k}(I)$	$T_{1k}(I)$	$T_{2k}(I)$	$T_{3k}(I)$
0	$\hat{1}$	$\hat{I}_z$	$\sqrt{\frac{1}{6}}[3\hat{I}_z^2 - I(I+1)]$	$\sqrt{\frac{1}{10}}[5\hat{I}_z^2 - (3I(I+1)-1)]\hat{I}_z$

Table 1. 4 – Irreducible spherical tensor operators $T_{l0}(I)$ expressed in term of Cartesian operators.[10,11]

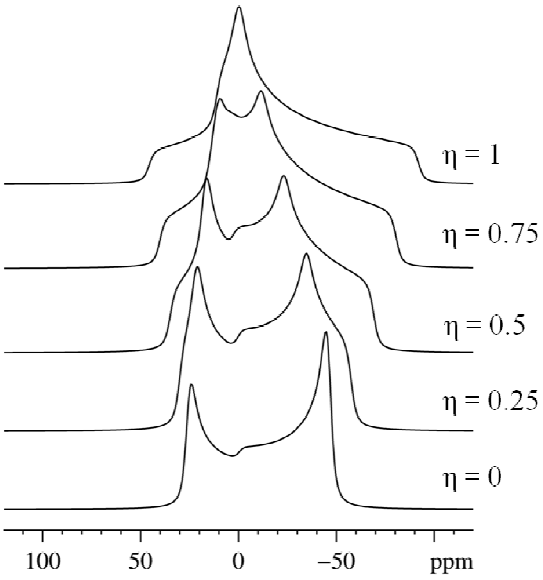

Figure 1.4 – Central transition lineshape under static conditions as function of the asymmetry parameters η.

Several considerations must be done:

- The first order term has the same orientation dependence of chemical shift anisotropy and dipolar interaction. So for small quadrupolar coupling constants, the spectrum of a quadrupolar nucleus will have the typical feature of chemical shift anisotropy and hetero-nuclear dipole-dipole interactions.

- The first term of the second-order energy correction equation has no orientation dependence; it is an isotropic term. So the isotropic shift seen in any spectrum of a quadrupolar nucleus has a contribution from the quadrupolar interaction.

- The second order correction terms have an inverse dependence on ω_0 so it is possible to minimize these terms by increasing the external applied field.

- The fourth rank term in the second order quadrupolar Hamiltonian has a complex spatial dependence and rotation about one axis cannot average completely this interaction; more complex techniques are needed and will be described at the end of this chapter..

1.4.7 - The paramagnetic term, $\hat{H}_P$

An additional interaction is present when the material contains unpaired or conduction electrons. It is possible to distinguish between two main cases:

- Conduction delocalized electrons (*e.g.* conducting solids)

- Unpaired localized electrons (*e.g.* transition metal ions, lanthanides ions, organic radicals)

As the interactions and the effects on the NMR spectra are considerably different for localized and delocalized electrons, these two interactions need different approaches and discussions. Delocalized electrons occupy energy levels in a pairwise fashion (Pauli exclusion principle) from the lowest energy level to the Fermi level. In the presence of an external magnetic field the energy of spin-up and spin-down states changes, this shift in the energy of the states leads to a change in the population that, in turn, give origin to a net magnetization of the material and hence to an associated susceptibility called the Pauli susceptibility, X_P and thus to a new net magnetic field ΔB. The overall effect on the NMR spectrum is a shift, called Knight shift.
In this chapter the attention is focused on the case of the presence of localized electrons related to transition metal ions as the systems discussed in the following chapters mainly deal with this class of materials.

Localized electrons

Paramagnetic interaction takes place when the materials contain localized unpaired electrons; these are a source for additional local magnetic field at the site of the nuclei. In this sense the metal ion can be seen as a source of spin density from which the spin is partially transferred from the original center to other chemically bonded atoms. The fraction of a spin is usually called *spin density* and it is given in atomic units. The spin density has a sign that define the orientation of this quantity parallel or antiparallel with the respect of the external applied magnetic field; the spin density as well as its sign can be determined by the NMR spectroscopy.[12]

The H_P term is affected by different and important contributions arising from different phenomena. For long time the lack of a quantitative quantum-mechanic description and the gap in the underlying physical formalism have made the treatment of paramagnetic NMR systems very difficult to approach. Recently several contribution to the development in this field have been done and a quantitative description can be given.[13-16]
It is necessary to consider the globality of these interactions; many different approaches have been proposed[17-20] but the simplest way to include all the different terms is to consider the electron spin resonance, *ESR*, Hamiltonian

$$\begin{aligned} H_{ESR} &= H_{Zeeman,I} + H_{Zeeman,S} + H_{Hyperfine,I-S} + H_{ZFS} \\ &= -\gamma B_0 \cdot (1 - \sigma_{orb}) \cdot I + \mu_B B_0 \cdot g \cdot S + S \cdot A \cdot I \\ &\quad + S \cdot D_S \cdot S \end{aligned} \tag{1.77}$$

This expression includes:

- the Zeeman interaction between the nucleus and the external magnetic field together with shielding effects, encapsulated in the σ tensor;

- the Zeeman interaction between the unpaired electron and the external magnetic field and shielding effect embodied in the g tensor;

- the hyperfine interaction between the nucleus and the electron, coupled trough the hyperfine tensor A;

- the zero-field splitting, *ZFS*, interaction due to electrons, defined with the tensor, D_S.

Al these terms have an effect on the shift and lineshape of the NMR signals; at the same time it must be considered the relative relaxation of the two spins involved in the interaction. The dynamic of the relaxation and precession of the electronic spins is order of magnitude faster that the timescale of NMR phenomena, the spin experienced by the nuclei is not the actual electronic spin but the thermal averaged *Curie spin* given by the Boltzmann distribution over the thermally populated electronic states

$$\langle S_z \rangle = \frac{\sum_{M_S} M_s \exp\left\{\frac{-g_e \mu_B M_S B_0}{k_B T}\right\}}{\sum_{M_S} \exp\left\{\frac{-g_e \mu_B M_S B_0}{k_B T}\right\}} \qquad (1.78)$$

$$\langle S_{\pm} \rangle = 0$$

Where M_S is the magnetic quantum number defining the electron Zeeman states.
In the high temperature limit it is possible to simplify the expression for the Curie spin into

$$\langle S_z \rangle = \frac{g_e \mu_B B_0}{3 k_B T} S(S+1) \qquad (1.79)$$

In a classical picture, the Curie spin $\langle S_z \rangle$ can be related to the average moment $\langle \mu_S \rangle$ that is directly related to the magnetic susceptibility X

$$\langle \mu_S \rangle = \frac{\mathrm{X}}{\mu_0} \mathrm{B}_0 \qquad (1.80)$$

The global Hamiltonian can be thus be rewritten as function of the Curie spin

$$\begin{aligned} H_{ESR} = & -\gamma B_0 \cdot (1 - \sigma_{orb}) \cdot I + \mu_B B_0 \cdot g \cdot \langle S \rangle \\ & + \langle S \rangle \cdot A \cdot I + \langle S \rangle \cdot D \cdot \langle S \rangle \end{aligned} \qquad (1.81)$$

From the definition of the Curie spin it appears that the quantity $\langle S \rangle$ is no more a characteristic of the electron but it has a direct dependence on the external magnetic field. The hyperfine term can thus be rewritten as a Zeeman term as the nuclear spin is ultimately coupled to the external magnetic field.
From the point of view of the NMR experiment it is possible to distinguish between terms that give origin to a shift and terms that affect the broadening of the spectra. The shift is mainly due to the average local magnetic field due to the unpaired electrons (thus, ultimately to the spin density) while the broadening is due to the effect of fast electron spin relaxation. The chemical shift of open shell systems has been described with the use of different formalisms. Classically it was formulated with the use of spin susceptibilities and the point-dipole approximation[20]; with the use of the above mentioned formalism of the *ESR* Hamiltonian it is possible write the hyperfine shift, δ_{HF}, tensor of a nucleus for a general systems $S > ½$

$$\delta_{HF} = -\frac{\mu_B}{kT\gamma}\, g\langle SS\rangle_0 A \qquad (1.82)$$

Where $\langle SS\rangle_0$ represents the Boltzmann population of the electronic spins when no external magnetic field is applied and thus *ZFS* interaction can be considered. In systems where the *ZFS* term is absent, the $\langle SS\rangle_0$ is simplified to the form

$$\langle SS\rangle_0 = \frac{1}{3}\, S\,(S+1) \qquad (1.83)$$

The expression of the hyperfine shift, δ_{HF}, of a nucleus in a systems where S = ½ without thermally accessible electronic exited states is given simply by

$$\delta_{HF} = \frac{S(S+1)\mu_B}{3kT\gamma}\, g \cdot A \qquad (1.84)$$

where g and A are the g- and hyperfine tensors respectively. Both g and A are general 3X3 matrices; as mentioned in the initial part of this chapter they can be decomposed into an isotropic value (zeroth-rank tensor), a pure anisotropic symmetric part (second rank tensor, accounting for anisotropies) and a first rank asymmetric tensor. This last term can be neglected as it does not affect the shift, it can give only small contributions to spin relaxation dynamics.
Tensor g can is usually decomposed according to

$$g = (g_e + \Delta g_{iso}) + \Delta\tilde{g} \qquad (1.85)$$

Where g_e is the isotropic value of the free electron while Δg_{iso} and $\Delta\tilde{g}$ are the isotropic and anisotropic parts of the Δg matrix accounting for electron in a specific environment.
Similar decomposition is proposed for the A matrix

$$A = A_{FC} + A_{SD} + A_{PC} + A_{SD,2'} + A_{AS} \qquad (1.86)$$

where A_{FC} is the Fermi contact contribution, A_{SD} is the dipolar coupling between I and S, A_{PC} is the pseudo contact term, $A_{SD,2'}$ is the spin orbit contribution to the dipolar coupling (anisotropy), A_{AS} is the anti-symmetric component of the tensor. A paramagnetic system where only the electronic spin contributes to the total angular momentum can be described totally by the first two terms. When there is also a orbital contribution to the global angular momentum, also the other terms must be considered. A detailed analysis of the individual contribution leads to identify A_{FC} and A_{PC} as pure isotropic coupling terms; the first one is cause by the localization of the electron spin density at the site of the nucleus trough the chemical bonds while the second is due to the pure spin-orbit coupling. The A_{SD} and $A_{SD,2'}$ are second order symmetric tensors and are related to the anisotropic part of the interaction. The δ_{HF} is then calculated as product of g, the transpose of A and the temperature dependant term. This lead to

presence of variety of different terms both isotropic and anisotropic.

	Term	*Label*	*Trad. assignment*	*Description*
		Isotropic term		
$\boldsymbol{\delta_{T,iso}}$	$g_e A_{FC}$	A	$g_e f_s A_s$	Contact shift (give isotropic spin density of the atom)
	$g_e A_{PC}$	B	$g_e f_s A_s$	
	$\Delta g_{iso} A_{FC}$	C	$g_e f_s A_s$	
	$1/3 * Tr(\Delta\tilde{g} \cdot A_{dip})$	D	$\delta_{SD,iso}$	Spin dipolar shift, ("pseudocontact shift" *)
$\boldsymbol{\delta_{orb,iso}}$			$\delta_{dia,iso}$	Diamagnetic shift
		Anisotropic term		
$\boldsymbol{\Delta\delta_T}$	$g_e A_{dip}$	E	$g_e f_p A_p$	Spin density informations in p-type orbitals
	$g_e A_{dip,2}$	F	$g_e f_p A_p$	
	$\Delta g_{iso} A_{dip}$	G	$g_e f_p A_p$	
	$A_{FC}\Delta\tilde{g}$	H	$g_e f_p A_p$	
	$\Delta\tilde{g}A_{dip} - 1/3 * Tr(\Delta\tilde{g} \cdot A_{dip})$	I		(No equivalent for traditional assignment)
$\boldsymbol{\Delta\delta_{orb}}$			$\Delta\delta_{orb}$	Diamagnetic orbital shift

Table 1.5 – Isotropic and anisotropic terms of the δ_{HF} for a S = ½ system.[22,23]

** We want to make the point with the use of the term "pseudo-contact". This term is usually employed to describe the isotropic contribution given by the expression* $1/3 * Tr(\Delta\tilde{g} \cdot A_{dip})$*, as reported also in this Table. This use is very common but not proper. The isotropic contribution reported with the label "D"in the table is due to the dipolar coupling between the nucleus and the electron in the case of spin-only system and thus can be define as "dipolar coupling", as we report in the main text with the label* A_{SD}*. The pseudo-contact term still gives a isotropic contribution but arises from the spin-orbit coupling, called* A_{PC} *in above discussion. In the following text we will refer to this correct use of the "pseudo-contact" and "dipolar coupling" terminology.*

The two main contributions, as discussed in following discussion, are found to be the spin-only terms A_{FC} and A_{SD}. For their relevance they are discussed further in the following sections.

Fermi contact

Unpaired external electron density induces (through the mechanism of spin polarization through chemical bonds) spin polarization to the *s*-orbital electrons that have a non-zero density at the site of nucleus

$$\hat{H}_{FC} = A_{FC}\hat{I} \tag{1.87}$$

This polarization of *s* orbitals interacts directly with the nuclear magnetic moment and gives origin to a frequency shift

$$\Delta\nu_c = \frac{A_{FC}\gamma_L B_0}{\hbar} \langle S_z \rangle \tag{1.88}$$

Where $\langle S_z \rangle$ is the average component of the electron spin along the direction of the applied magnetic field and depends on the total angular momentum quantum number for the electrons, γ_L is the Landè factor. This kind of interaction can take place not only for the same nucleus of the unpaired electron but this polarization can

be transmitted trough chemical bonds as *transferred hyperfine interaction*. This effect decreases rapidly with the increasing number of the chemical bonds and depends on the bond angles. The Fermi contact term in paramagnetic compound is found to be the dominant effect.

Dipolar coupling

The magnetic momentum of the nucleus can interact with the average electronic magnetic momentum trough space with the classic, already mentioned, dipolar effect. The shift caused by the dipolar interaction

$$H_{SD} = \sum_{m=-1,0,1} D_{2,0}\, d^2_{0m}(\beta_{PL}) T_{2,m} \tag{1.89}$$

Where:

- $D_{2,0}$ is the non zero component of the traceless axially symmetric rank 2 dipolar coupling tensor *D*

$$D_{2,0} = \sqrt{6}\,\frac{\hbar \gamma_I \mu_B g_e}{4\pi r^3_{IS}} \tag{1.90}$$

- $d^l_{m,m'}(\beta_{PL})$ is the reduced Wigner matrix element and β_{PL} the angle between the principal axis of the *D* tensor and the magnetic field

- $T_{2,m}$ are the binary product of the *X* susceptibility tensor components with the nuclear spin operator *I*. In the high field approximation only the I_z terms are retained after truncation and the spin-operator are reduced to

$$T_{2,0} = \frac{2}{3}\mathrm{X}_{2,0} I_z B_0 - \frac{\sqrt{2}}{3}\mathrm{X}_{0,0} I_z B_0$$
$$T_{2,\pm 1} = \pm\,\frac{1}{2}\langle \mathrm{S}_{\pm}\rangle I_z = 0 \tag{1.91}$$

$$T_{2,\pm 2} = 0$$

Together with the Fermi contact interaction, the dipolar term is one of the strongest interactions that affects the NMR spectra; particularly this term is responsible of the huge anisotropies (thousands of ppm) characteristic of these systems.

1.5 - NATURE OF THE INTERACTIONS

All the terms that compose the global Hamiltonian are similar in form and, particularly, they contain an anisotropic part with an orientation dependence that cause broadening in the powder NMR spectrum where all the orientations of the sample are represented. From the first order term obtained from perturbation theory, the angular dependence is of the general form $\Delta((3cos^2\beta - 1) + \eta sin^2\beta cos2\alpha)$ with α and β defining the orientation of the particular local contribution respect to the main magnetic field B_0 andt is similar for all the interactions.

The anisotropic part of a specific interaction can provide information about the local structure, being strongly related to the local environment of the nuclei. On the other hand, the anisotropic part gives origin to broadening which can be so significant to lead to strong overlapping between the signals from different sites, lowering the global resolution of the spectrum. In liquids, the anisotropic interactions are averaged by the continuous, random tumbling motion that is rapid (~10^{-13} s) in comparison with the NMR time scaling (>10^{-10} s). This isotropic averaging of the second-rank tensor interactions leads to high resolution in spectra. In solids, high resolution may be obtained by averaging voluntarily the anisotropic components of the interactions.

The Hamiltonian terms are function of spatial and spin variable of the nuclei. The major task in solid state NMR is to manipulate

either the spatial or spin parts (or both at the same time) of the Hamiltonian, in order to recover the typical narrow isotropic resonances known from liquid NMR. Oh the other hand, the challenge is to maintain or selective reintroduce sufficient spectral information for structural characterization. This usually means making them time-dependent. The two main approaches are the use of mechanical techniques for averaging of the spatial part, and the use of pulse techniques for the averaging of the spin part.

Different techniques developed for the resolution of specific problems and for the selective suppression/ reintroduction of particular term of the global Hamiltonian are presented below. Particular attention will be devoted to two distinct cases: quadrupolar and paramagnetic interactions.
Due to their abundance, quadrupolar nuclei are dominant in several systems including porous materials, ceramic, glasses, superconductors and also biological system. Two main factors have limited the routine study of these materials: the line broadening rising from the size of the quadrupolar coupling and the complex spin dynamics due to the presence of more than two energy levels. Paramagnetic compounds are of primary importance in many different fields of materials science, ranging from energy technology to complex biological systems. Such compounds were historically considered bad candidates for NMR study. Due to the relevance of roles played both by quadrupolar and paramagnetic systems, many efforts were devoted to the development of techniques that allow their study. Nowadays the availability of high magnetic field, ultra-fast MAS together with the development of new probes and pulse sequences have paved the way to the high resolution of solid state quadrupolar and paramagnetic systems; the major techniques and methods are presented below.

1.5.1 – Spatial term manipulation: sample rotation

Magic Angle Spinning, MAS, is the most widely used technique to enhance spectral resolution in solid state NMR.[24] MAS consists in the rotation of the sample loaded in a special container (rotor) at a fixed angle with the respect to the magnetic field. In this system the Hamiltonian becomes time dependant and to be correctly defined is to be referred not to the *PAF* but to the rotor axis frame, *RAF*, with the use of Euler angles that define the relative orientation between the two reference systems. The Hamiltonian acquires a modulation of the form $^1/_2\,(3cos^2\Theta - 1)$ that is the second order Legendre polynomial $P_2(cos\Theta)$. Choosing the condition $\Theta = arctan\sqrt{2}$ that is to say Θ is set to 54°44'8'' the value of $P_2(cos\Theta)$ is zero and the anisotropic part vanishes, leaving only the isotropic part as obtained for the solution NMR. It should be stressed that this is valid if two conditions are respected:

- the spinning speed is high if compared to the magnitude of the considered interaction and exceeds it ($\nu_{MAS\ rot} >> \nu_{int}$);

- the first order term obtained with the use of perturbation theory can be considered as the only relevant contribution in describing the considered interaction.

If the first condition is not respected, the time modulation of the Hamiltonian produces a pathway of spinning sidebands that are signals separated from the isotropic line by integer multiples of the spinning frequency, and they extend to cover a range of the order of magnitude of the static anisotropy interaction. At the moment, very fast magic angle spinning, *VFMAS*, up to 30 kHz and ultra fast magic angle spinning, *UFMAS*, at 70 kHz, are achieved, but some lines encountered in solid state NMR are still broader. Further technological developments are needed for the

mechanical rotation of the sample: rotation up to 100 kHz have just been made available. Such rotations are suitable for the average of H_{CS} and H_D terms, higher rotations are not needed as it is impossible to completely address the quadrupolar and paramagnetic systems only with the spinning of the sample. At the same time, it is possible to couple the MAS technique to other averaging method (pulse sequences) to address these specific problems.

The second condition is a considerable limit, as in many cases it is not sufficient to consider only the first-order term in perturbation theory and further terms must be take into account, the most important case is represented by the second-order quadrupolar term. In this case, even *UFMAS* cannot completely average this term due to their particular orientation dependence. In fact, the second order quadrupolar term has an isotropic component together with an anisotropic part that is proportional to the second-order and fourth-order Legendre polynomials for which no single angle can simultaneously average, *i.e.* $P_2(\cos\Theta) = 0$ and $P_4(\cos\Theta) = 0$.

In order to address the problem of high resolution for quadrupolar nuclei, different complex techniques based on rotation of the samples have been proposed. Particularly the Variable Angle Spinning (VAS),[25] the Double Rotation (DOR),[26,27] and the Dynamic Angle Spinning (DAS).[28-30] All these techniques are mechanically challenging and suffer for many limitations in maximum speed available, the necessity of dedicated probes and modified pulse sequences. These aspects together with the availability of the *MQMAS* technique, presented below, are made the use of complex mechanical rotation methods not very common and used only for fringe researches.

1.5.2 – Spin term manipulation: quadrupolar techniques

The Multiple Quantum MAS (*MQ MAS*) was presented in literature in 1995 by Frydman and Harwood as a 2D pulse sequence to obtain high resolution spectra for half-integer quadrupolar nuclei under MAS conditions.[31] It correlates the high resolution isotropic spectrum in the indirect dimension to the corresponding MAS spectrum in the direct dimension. Differently from VAS, DOR and DAS techniques it does not require a special probe and it is easy to implement: it has become the primary method for the study of such systems which were previously neglected. It is a 2D sequence that achieves high resolution refocusing during a period of free precession kt_1 the evolution of the magnetization that has evolved during the period t_1. This is possible thanks to the change of the transition frequency that is achieved by changing the order of the evolving coherence. During the period t_1 the multiple quantum coherence corresponding to the transition $+m \rightarrow -m$ evolves; this coherence is then converted into the observable single quantum coherence that evolves in the second period kt_1.

The frequency of the symmetric $+m \rightarrow -m$ transitions for a half integer quadrupolar nucleus is affected only from the second order term and thus depends of the *k-th* rank V_{k0}^{Q} tensor components V_{00}^{Q}, V_{20}^{Q} and V_{40}^{Q}. The zero rank term is an isotropic component, the second rank term is averaged to zero by *MAS*, that is assumed to average to zero also dipolar and *CSA* interaction. Thus, the only anisotropy in the evolution during t_1 is the one arising from V_{40}^{Q} term. Thus under MAS conditions only isotropic and forth-rank terms remain. For different transitions the amplitude of the anisotropic terms are related by a scaling factor; it is possible to refocus the fourth-rank term leaving the isotropic shift by correlating the multiple quantum (triple quantum is usually considered) to the single quantum coherence in a 2D

spectrum. This is done with the use of a second *RF* pulse that transfers the remaining multiple quantum coherence, *MQC*, into the observable single quantum, *SQC*, + ½ -> - ½ transition. The evolution of the *MQC* under the V_{40}^{Q} term during t_1 is refocused during kt_1 under the V_{40}^{Q} term associated with the central transition. The value of *k* is given by the ratio of the coefficient of the V_{40}^{Q} term in the frequency of the *MQC* and the one of the central transition. At the end of the kt_1 period, a normal FID is collected in a 2D dataset. The FT produces a 2D spectrum in which the f_1 dimension shows the isotropic spectrum and in the f_2 the isotropic powder MAS spectrum is given.

The 2D spectrum obtained contains ridge lineshapes that lies along the gradient related to the scaling factor of the anisotropy of the forth rank term relatively to the central transition, already described above (for *I*= 3/2 the slope is -7/9).
Since the MQMAS was presented the first time, numerous variants and modifications of the original experiment were proposed (Figure 1.5 and 1.6), most of them concerning the achievement of optimal conditions for excitation of the *MQC* and the reconversion pulse to single quantum coherence, *SQC*.

One of the major limitation of *MQMAS* is the sensitivity issue. The excitation of multiple-quantum coherences and their reconversion into observable single-quantum coherehcens are intrinsically inefficient processes, with the efficiency depending strongly on the C_Q. This can lead to differences in sensitivity for species affected by different C_Q and also distortions within the inhomogeneous broadened quadrupolar lineshapes. There have been various attempts to improve and increase the sensitivity with the use of adiabatic pulses or composite pulses[32,34] but the sensitivity is still the main problem of *MQMAS* experiment.

The *MQMAS* experiment removes only the forth rank broadening due to the second order quadrupolar Hamiltonian; second rank broadening (due to quadrupolar interaction, dipolar copupling or *CSA*) is removed by MAS. Any anisotropy described by a fourth-rank tensor arising from other interactions will not be refocused by the *MQMAS* and will remain in the spectrum.

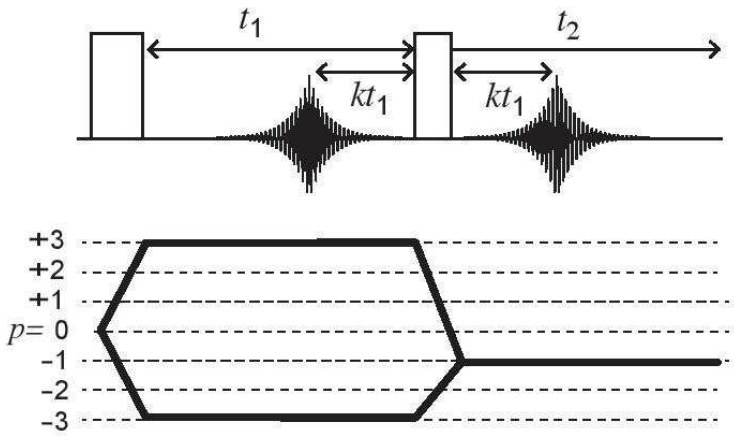

Figure 1.5 - The two pulses MQMAS sequence presented originally by Frydman and Harwood.[31] The 2D experiment provides isotropic spectrum in the F1 dimension and second-order lineshape (MAS) in the F2 dimension. The first RF excites all the possible MQ coherences, must be hard. After the evolution period t1 the second RF pulse converts the MQ coherence into a-1Q observable coherence. The phase cycling allows to select the desired MQ coherence. For a spin I = 3/2 the 0Q -> +3Q -> -1Q is the anti-echo pathway, 0Q -> -3Q -> -1Q is the echo pathway. For 3Q-MAS experiment with the other half-integer spins, 0Q -> +3Q -> -1Q is the echo pathway, 0Q -> -3Q -> -1Q is the anti-echo pathway. Shearing transformation is required to obtain 2D isotropic – anisotropic correlation spectrum.

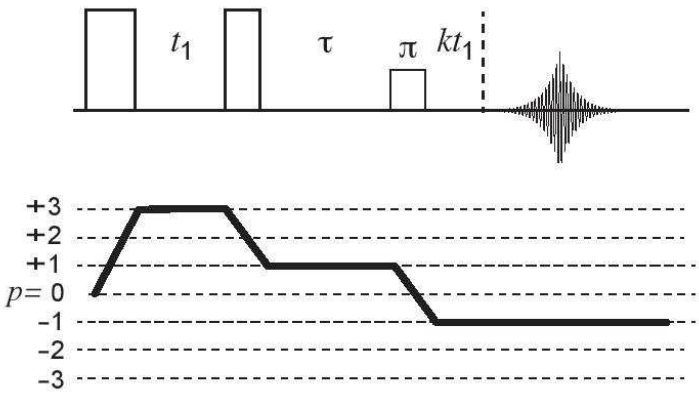

Figure 1.6 –The phase modulated split t_1 approach to MQMAS.[35] The t_1 evolution period is split (12/31 and 19/31) between the MQ and SQ precessions; the second order quadrupoalr broadening is refocused at the end of the total t_1 period without the need for shearing. The echo is shifted of a time τ in order to collect the whole echo during the t_2 time domain. In this sequence the third pulse is a selective π pulse for the central transition. For the experiment applied to I=3/2 the anti-echo pathway is involved and the anti-echo is recorded while for the experiment applied to I = 5/2 the echo pathway is involved. Therefore, the echo is recorded.

1.5.3 – Spin term manipulation: paramagnetic techniques

Solid state paramagnetic systems have been considered for a long time the pillars of Hercules of NMR due to a great variety of problems that are implied in such systems, among which huge shift anisotropy, difficulty in the irradiation of the whole frequency range, low sensitivity. On the other hand, paramagnetic systems can present also considerable advantages as enhanced resolution thank to massive chemical shifts, large chemical shift anisotropy that can be related to structural information, enhanced

relaxation that allow both the increment of the number of scans and contrast the low sensitivity problem and finally the selective saturation of nuclei far from the paramagnetic center, long range information due to the nature of the interaction. Furthermore, paramagnetic system cover a role of central importance in may relevant fields as biological and materials sciences.

Until very recently very few progresses have been made with paramagnetic NMR. Two main innovations led to the progress in this field:

- the advent of Very Fast and Ultra Fast MAS probes;

- the development of Adiabatic Pulses and relatives pulse schemes.

MAS technique has been already described in this chapter, and the use in the context of paramagnetic systems is due to the ability of MAS technique to average the first term of different Hamiltonian components given by the perturbation theory tratment. As already explained, paramagnetic interaction is one of the broadest and, when present, it generally dominates the spectrum. Spinning rates available today (up to 100 kHz) are not able to cover the paramagnetic broadening. MAS by itself it is not enough to completely average the paramagnetic interactions and to solve the resolution problems, but it is an essential tool if combined with suitable pulses and pulse sequences.
This leads inevitably to the presence of wide sideband patterns dominating the spectrum of paramagnetic systems. The presence of the sideband patterns can be very useful as the powder pattern shape can give information about the anisotropic part of the interactions that originates the broadening. At the same time the overlapping of several broad powder patterns prevents the

separation of the different contributions limiting the amount of information that can be extracted from the spectrum. Several 2D techniques have been proposed to simultaneously obtain the isotropic information in one dimension related to the anisotropy broadening in the other dimension.[36,38]

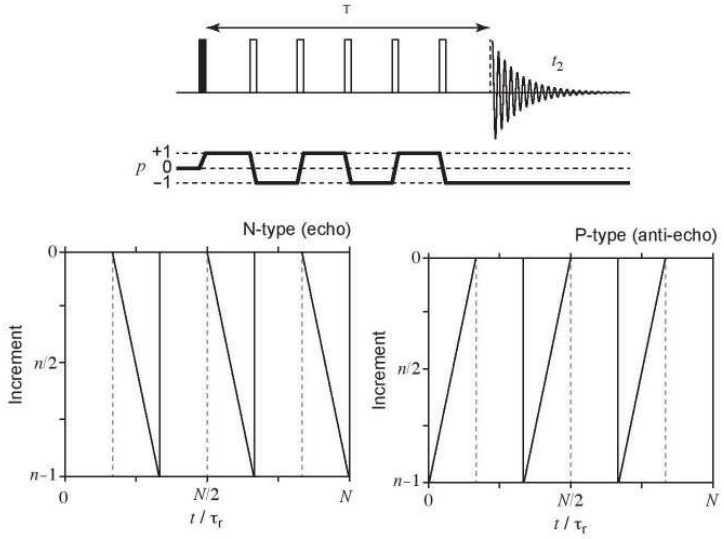

Figure 1.7 – The MAT sequence with the five π pulses during the period T together with the increment representation.

One of the useful approach is the *Magic Angle Turning* sequence, *MAT*, based on the *5-π* pulse sequence presented in Figure 1.7.[39] This is a constant time experiment in which during the period of constant length *T* that is an integer product of the rotor period, five *π* pulses are applied; the second and forth pulses are at fixed time *T/3* and *2T/3*. The first, the third and the fifth pulses are applied at *T/6-τ*, *T/2- τ* and *5T/6 – τ* respectively: their position is variable during the pulse sequence and it is determined by the variable *τ*. When *τ* is equal to 0 the five pulses are equally spaced; for *τ < 0* the moving pulses are later respect to the equally spaced

situation and for $\tau > 0$ they are earlier. Thus the evolution variable is limited in the range $-T/6 < \tau < +T/6$. The pulse sequence give origin to a phase modulated 2D experiment where the isotropic indirect dimension shows only the isotropic shift without any contribution from the sideband pattern, independently from the spin rate. The direct dimension presents the classical sidebands pattern of the rotating sample.

The shift anisotropy, *SA*, can be typically on the order of 500- 1000 ppm depending on the nature of the paramagnetic centre; this range is much broader of the practical RF amplitudes. In these conditions, spin excitation is a problem and this factor can constitute the barrier to further progresses in the study of paramagnetic systems. One possible strategy for the approaching of huge broadband excitation is to use sweep-frequency adiabatic pulses. Adiabatic Pulses (*AP*) constitute a relatively new excitation approach in which the carrier frequency varies with time during the length of the pulse. Recent developments in this field have expanded the capability and application fields of adiabatic pulses particularly for magnetic resonance imaging (MRI) and high resolution spectroscopy, and also to facilitate the heteronuclear decoupling.[40]

The adiabatic pulses can be usefully described in the frequency-modulated frame, *FMF*. This *FMF* rotates synchronously with the instantaneous applied *RF* so that B_1 is fixed during the adiabatic passage. When the frequency of the pulse deviates from the ω_0 (Larmor frequency), a magnetic field of amplitude $\Delta\omega/\gamma$ appears along z-axis with $\Delta\omega = \omega_0 - \omega_{RF}$. In the *FMF* the effective field $B_{eff}(t)$ is the vector resulting from the sum of longitudinal field $\Delta\omega/\gamma$ and $B_1(t)$. As the ω_{RF} is time dependent, $B_{eff}(t)$ is also time dependent and it changes its orientation with angular velocity $d\alpha/dt$ where α is

$$\alpha(t) = \arctan\left[\frac{\gamma B_1(t)}{\Delta\omega(t)}\right] \tag{1.92}$$

During the adiabatic passage the magnetization *M* is locked along the effective field $B_{eff}(t)$ throughout the pulse if the adiabatic condition is respected

$$\left|\gamma B_{eff}(t) \gg \left|\frac{d\alpha}{dt}\right|\right| \tag{1.93}$$

That is to say that frequency is swept and the amplitude profile is modulated in such a way that the rate of change the angle Θ of the $B_{eff}(t)$ is negligible with respect to the $\omega_{eff}(t)$. The magnetization vector can be carried from +*z* to –*z* modeling Θ from +π/2 to –π/2.

Application and treatment of adiabatic pulses in rotating solids is not trivial as the system is strongly perturbed by the shift modulation imposed by the sample rotation. The main problem for the use of *AP* in rotating solids is the shift anisotropy modulation. The presence of such time dependent term reduces greatly the quality factor of the pulse making the inversion of the magnetization vector not complete. Moreover, the shift anisotropy modulation is different for each crystallite in the rotating sample. The presence of this term does create some conditions that must be respected for the *RF* amplitude, the sweep width and the pulse length in order to obtain efficient and total inversion of the magnetization vector.
Taking in consideration all the restrains and the specific conditions for this system, a new class of *Short High Power Adiabatic Pulses*, *SHAPs*, has been recently developed.[41] The use of high power allows the design of very short adiabatic pulses related to a wide and fast frequency sweep, remaining in the limit of the adiabatic condition. The great advantage of *SHAPs* respect to the traditional *AP* is that it addresses completely the problem of

shift anisotropy that was the true limit for application of *AP* on paramagnetic systems under VFMAS. *SHAPs* can be enclosed as building block in more complex pulse sequences. This is a very important feature because it allows the use of pulse sequences that address the problem of the huge sideband patterns presented above. This problem is exacerbated by the high fields and is particularly severe in case of presence of many sites.

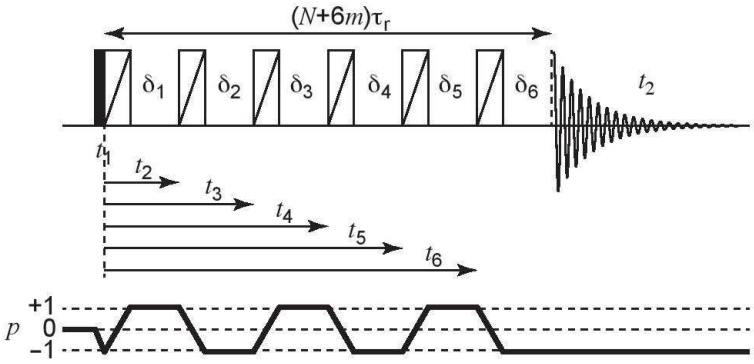

Figure 1.8 – aMAT pulse sequence; the train of π pulses is replaced by a train of adiabatic pulses; the scheme for the increment is very similar to those of the original MAT sequence.

It is possible to encapsulate the *SHAPs* into the *MAT* scheme presented above; the brilliant combination of these different building blocks and techniques had lead to the introduction of the adiabatic-MAT, aMAT, pulse sequence.[42] This sequence is expected to be carried under *UFMAS* conditions and incorporates the *SHAPs* into the *MAT* experiment in place of the 180° pulse train. This sequence gives impressive results, allowing to high resolution together with complete removing of the overlap between the sideband manifolds for paramagnetic systems and

efficient separation of the different isotropic shift over a wide range of spectral frequencies (~ 1MHz).

The continuous developments in different field of solid state NMR (probes technology, pulse schemes, advanced electronic components) open the route for the study of new systems; particularly the introduction of the techniques presented in this chapter and their intelligent combination paves the way to the study of very complex quadrupolar materials and paramagnetic systems.

1.6 - REFERENCES

1. M. Mehring, *"Principles of High resolution NMR in solids"*, Springer-Verlag Berlin Heidelberg New York, (1983).
2. K.J.D. MacKenzie, M.E. Smith, *"Multinuclear Solid State NMR of inorganic materials"*, Pergamon Materials Series, (2002).
3. M.M. Maricq, *Phys. Rev. B*, 25 (1982) 6622-6632.
4. P.W. Atkins, "*Molecular Quantum Mechanics, second ed*.", Oxford University Press, Oxford, (1983) (Chapter 8).
5. M.M. Maricq, J.S. Waugh, *J. Chem. Phys*., 70 (1979) 3300.
6. S.N. Stuart, *J. Magn. Reson. A,* 101 (1993) 327.
7. M.H. Cohen, F. Reif, *Solid Stat. Phys*., 5 (1957), 321.
8. P.P. Man in "*Encyclopedia of Analytical Chemistry*" (2000), Ed. Meyers, John Wiley and sons, Chichester, p 12224.
9. H.A. Buckmaster, R. Chatterjee, Y.H. Shing, *Phys. Stat. Sol. A,* 13 (1972) 9–50.
10. P.J. Grandinetti, J.T. Ash, N.M. Trease, *Prog. Nucl. Magn. Res. Spect.,* 59 (2011) 121-196.
11. K. Schmidt-Rohr, H.W. Spiess, *"Multidimensional Solid State NMR and Polymers"*, Academic Press, London, (1994).
12. K. Itoh, M. Kinoshita, *"Molecular Magnetism"*, Kodasha, Tokyo, and Gordon and Breach Science Publishers, Australia, (2000).
13. C.P. Grey, Y.J. Lee, *Sol. State Scie*., 5 (2003) 883–894.
14. C.P. Grey, N. Dupré, *Chem. Rev*., 104 (2004) 4493-4512.
15. G. Pintacuda, G. Kervern, *Curr Chem*.,335, (2013) 157-200.
16. M. Kaupp, F.H. Köhler, *Coordin. Chem. Rev*., 253 (2009) 2376-2386.
17. I. Bertini, C. Luchinat, *Coord. Chem. Rev*. 150 (1996) 1.
18. L.P. Kazansky, B.R. McGarvey, *Coord. Chem. Rev*., 188 (1999) 157.
19. T.O. Pennanen, J. Vaara, *J. Chem. Phys*., 123 (2005) 174102.

20. M. Kaupp, M. Bühl, V.G. Malkin, "*Calculation of NMR Parameters"*, Weinheim, Wiley-VCH (2004).
21. L.P. Kazansky, B.R. McGarvey, *Coord. Chem. Rev*. 188 (1999) 157.
22. M. Kaupp, F.H. Köhler, *Coord.Chem. Rev,* 253 (2009), 2376-2386.
23. T.O. Pennanen, J. Vaara, *Phys. Rev. Lett.*, 100 (2008) 133002.
24. E.R. Andrew, *Int.Rev. Phys. Chem.,* 1 (1981) 195.
25. S. Ganapathy, S. Schramm, E. Oldfield, *J. Chem. Phys.*, 77 (1982) 4360.
26. A. Samonson, E. Lippmaa, A. Pines, *Molec. Phys*., 65 (1988) 1013.
27. B.F. Chemlka, K.T. Muller, A. Pines, J. Stebbins, Y. Wu, J.W. Zwanziger, *Nature*, 339 (1989), 42.
28. A. Llor, J. Virlet, *Chem. Phys. Lett*., 152 (1988), 248.
29. A.A. Samoson, E. Lippmaa, A. Pines, *Mol. Phys*., 65 (1988) 1013.
30. J.W. Zwanziger, B.F. Chmelka, *"NMR basic principles and progress"*, vol 31, Eds. Blumich, B.& Kosfeld, R. Springer-Verlag, Berlin.
31. L. Frydman, J.S. Harwood, *J. Am. Chem. Soc*., 117 (1995) 5367.
32. A.P.M. Kentgens, R. Verhagen, *Chem. Phys. Lett*., 300 (1999) 435.
33. P.K. Madhu, A. Goldburt, L. Frydman, S. Vega, *Chem. Phys. Lett.,* 307 (1999) 41.
34. R. Siegel, T.T. Nakashima, R.E. Wasylishen, *Chem. Phys. Lett*., 403 (2005) 353.
35. S.P. Brown, S. Wimperis**,** *J. Magn. Reson*., 128 (1997) 42-61.
36. W.P. Aue, D.J. Ruben, R.G. Griffin, *J. Chem. Phys*., 80 (1984) 1729.
37. Z.Gan., *J.Am. Chem. Soc*., 114 (1992) 8307.
38. A.C. Kolbert, R.G. Griffin, *Chem. Phys. Lett.*, 166 (1990) 87.

39. J.Z. Hu, D.W. Alderman, C. Ye, R.J. Pugmire, D.M. Grant, *J. Magn. Res. A,* 105 (1993) 82-87.
40. Garwood, M., DelaBarre, L. *J. Magn. Reson*., 153 (2001) 155 – 177.
41. L.J.M. Davis, I. Heinmaa,G.R. Goward, *Chem. Mater*. 22 (2010) 769.
42. R.J. Clement, A. Pell, D.S. Middlemiss, F.C. Strobridge, B.X.Y. Zhu, J.K. Miller, M.S. Whittingham, L. Emsley, C.P. Grey, G. Pintacuda, *J. Am. Chem. Soc*., 134 (2012) 17178-17185.

Chapter 2

The perovskite compound $LaSrAlO_4$

2.1 – THE PEROVSKITE STRUCTURE

$AA'BO_4$ compounds, a subgroup of the A_2BO_4 oxides with K_2NiF_4-type structure and known as the first member of the Ruddlesden- Popper (RP) series $A_{n+1}B_nO_{3n+1}$, are the subject of great attention due to the variety of their potential technological applications which strongly depend on composition. The general formula can be rewritten as $AO(ABO_3)_n$ to evidence the main feature of this structural system: the presence of *n* layers ABO_3 with perovskite structure spaced by AO rock-salt slabs, as reported in Figure 2.1.[1,2]

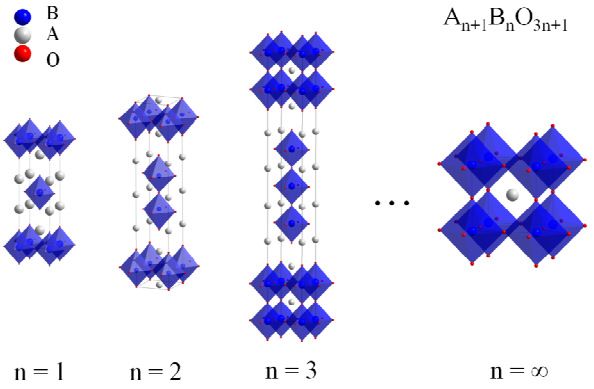

Figure 2.1 – Ruddlesden Popper series; member n = 1 with formula A_2BO_4, member n = 2 with formula $A_3B_2O_7$, member n = 3 with formula $A_4B_3O_{10}$, member n = ∞ with formula ABO_3.

The first members of the RP series with formula $AA'BO_4$ are characterized by intriguing electrical, magnetic, optical, catalytic properties related to the strong structural anisotropy due to the layered arrangement. According to composition, substitution, heating treatments, and synthesis route this system can crystallize in tetrahedral or orthorhombic structure. The structure is stable if the condition r_A / r_B ranging from 1.7 to 2.4 holds.[3] Basing on this condition, it is possible to foresee deviations from the perfect tetrahedral symmetry but it is also evident that this structure can accommodate a huge range of different combinations of element both on *A* and *B* sites, expanding the number of compounds based on this structure and thus the range of possible applications.

The nature (charge, dimension, electronic configuration) of *A* and *B* cations, together with the high degree of possible substitutions on these sites strongly influence the structure of the system and offer the opportunity to modulate the physical relevant properties. A wide variety of compounds belonging to this family have been proposed for applications in different fields. One relevant class of materials of formula Ln_2CuO_4 (*Ln* rare earth) has been studied for the relevant properties of superconduction at high temperature (HTSC), particularly the substituted system $YBa_2Cu_3O_7$, known as YBCO, and ruthenates systems.[4,5]

La_2MO_4 (*M* = Ni, Mn, Co) have been proposed as electrode materials for solid oxide fuel cells due to their high mixed oxide-ion/electronic conductivity, together with the higher members of the family, $La_3Ni_2O_7$ and $La_4Ni_3O_{10}$[6,7] they also find application in the field of catalytic combustions of CO for the reduction of atmospheric pollution.[8] Layered perovskites find applications also in the field of thermoelectric systems, combining proper thermal and electrical properties.[9]

Members of the family of $LnABO_4$ where *Ln* is a rare earth, *A* is a alkaline earth and *B* a metal not from the *d*-block, are studied for solid state laser applications, like in the case of $YCaAlO_4$ thanks to

the large crystal-field splitting associated with large zero-field splitting.[10]

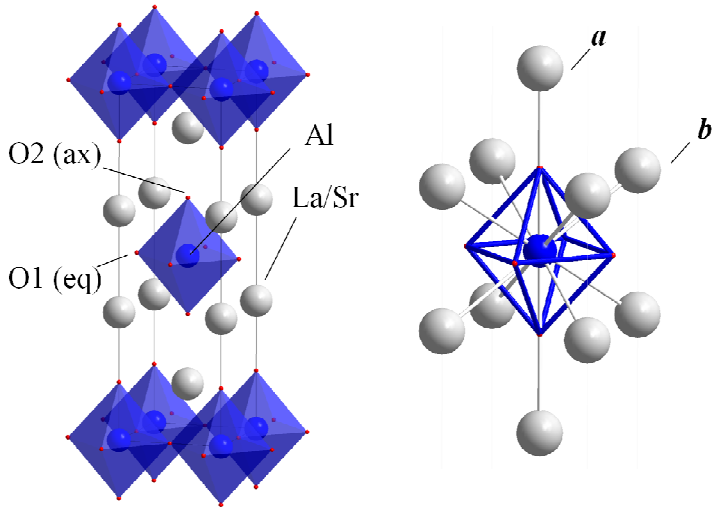

Figure 2.2 – $LaSrAlO_4$ structure, Al blue, La/Sr grey, O red. On the right the Al first coordination sphere (octahedral coordination with oxygen) and the second coordination sphere (La/Sr mixed occupancy site).

In this context, $LaSrAlO_4$ is in particular known as the most suitable substrate for thin film deposition of single layer high-TC cuprate superconductors.[11,12] $LaSrAlO_4$ crystallizes in the tetragonal space group *I*4/*mmm*. The structure, presented in Figure 2.2, is composed of AlO_6 octahedra connected to form a two-dimensional network by corner-shared oxygens. These layers are separated by (La,Sr)O slabs with the rock-salt structure. Within this structure, La and Sr are 9-coordinated to oxygen and each Al has 10 La/Sr nearest-neighbours. In the ideal K_2NiF_4-type structure only one crystallographic site (grey site in Figure 2.2) is available

for La and Sr (*0, 0, z*) and the cations are supposed to be randomly distributed over this site throughout the structure. Consistently, only one distinct crystallographic site (*0, 0, 0*) is available for Al (blue site in Figure 2.2). Previous studies on $LaSrAlO_4$ have supported this result through X-ray diffraction[13] as well as spectroscopic ellipsometry measurements.[14] Indeed, deviations from the ideal random distribution of the cations on the *A* site have not been evidenced for any compound with this type of structure by the use of average structure probes (such as X-ray or neutron diffraction).[13,15-17] A study on $LaCaAlO_4$ by X-ray diffraction discussed an indirect evidence of local ordering of the *A* site cations in this specific structure through the analysis of the modulation of the diffuse scattering background.[18] However, $^{63,65}Cu$ wide-line NMR studies performed on the $La_{2-x}Sr_xCuO_{4-d}$ system have clearly shown the presence of two distinct copper sites,[19] while an infrared and Raman spectroscopic study on the system $La_{2-x}Sr_xAl_{1-x}Mg_xO_4$ suggested the presence of local distortions in the Al/MgO_6 octahaedra, as opposed to the average situation derived from X-ray powder diffraction.[20] Both these studies indicate that two distinct *B* sites can be locally found when two different species share this crystallographic position (Cu with different oxidation states in the first case; Al or Mg in octahedral coordination in the second case), even though the average structure maintains the ideal symmetry.

In particular, we were searching for differences between average and local arrangements of the *B* site cation in this system. Since in this case only one species is unequivocally occupying the *B* site, the presence of two local arrangements for the Al site would only be ascribable to the *A* site population and distribution. Bearing in mind these evidences, in this Chapter we present the investigation of the structure of $LaSrAlO_4$, selected as a representative example of a family of compounds with K_2NiF_4-type structure thanks to its particular properties that makes it the best candidate for this kind

of study. ^{27}Al is particularly suitable for structural determination analysis as it is a quadrupolar nucleus, thus a good NMR probe for the investigation of local environments and distortions. Furthermore, aluminum is characterized by a close shell configuration with only one oxidation state available, reducing the complexity of the system by eliminating the structural dependence on the electronic configuration.
To investigate these aspects, *i)* the combined neutron and synchrotron X-ray diffraction as space-averaged probes, and *ii)* the pair distribution function analysis and ^{27}Al MQMAS-NMR as local probes have been used as complementary techniques. The analysis and discussion of the experimental results have been supported by the use of atomistic modeling techniques and are presented below.

2.2 – EXPERIMENTAL SECTION

Synthesis **-** A powder sample of nominal composition $LaSrAlO_4$ was prepared by a modified sol-gel Pechini method. Sol gel method was chosen since solid-state syntheses involving Al_2O_3 are usually non trivial and need long heating treatments together with high temperature. However, the solid-state method was also considered and several attempts were made, but the best results were obtained by sol gel preparation. Stoichiometric amounts of $La(NO_3)_3{\cdot}9H_2O$, $Sr(NO_3)_2$ and $Al(NO_3)_3{\cdot}9H_2O$ were used as starting materials, citric acid as the chelating agent and ethylene glycol to enhance the gelation process. A homogeneous aqueous solution of the metal salts was obtained after a thorough mixing. The pH of the solution was adjusted to approximately 8 in order to promote the complexation of the metal ions. The solution was dried slowly at 70 °C under continuous and vigorous stirring. After the complete evaporation of the water, the dried gel obtained was first heated at 700 °C to burn out the organic matter, then at 1300 °C for

12 hours to improve the crystallization grade of the compound, and finally slowly cooled down to room temperature.

Diffraction measurements **-** The sample was preliminary checked with laboratory X ray powder diffraction to control the purity of the phase, subsequently structural data were obtained from refinement of high quality diffraction measurements.

Diffraction is one of the main non-destructive techniques for the qualitative and quantitative analysis of crystalline materials. Diffraction is a physical phenomenon that can be treated by the means of a simplified model considering the radiation to be reflected from different crystallographic planes when the wavelength of the monochromatic radiation is comparable with the inter-plane distances of the crystal structure. If this condition is respected the incident radiation is reflected at a particular angle related to the inter-plane distance and to the wavelength according to the Bragg's law

$$2dsin\Theta = n\lambda \qquad (2.1)$$

A diffraction pattern is reported as a series of peaks intensities as function of the angle 2Θ covered by the incident and reflected radiations. The use of different radiation beams (X-rays, neutrons, electrons) allows to obtain different information. X-rays are sensible to the electron density so are proper for detection of heavy atoms; neutrons interacts with the nuclei with different efficiency according with the neutron cross section of every isotope and for this reason the use of neutron diffraction is particularly useful for accurate structural characterization in presence of light atoms (*e.g.* oxygen). In this case both X-rays and neutron measurements were collected to combine the advantages of the two techniques.
Room temperature neutron diffraction data were acquired on the D1A instrument at the Institute Laue Langevin (ILL) in Grenoble.

The measurement was recorded in air in a silica glass container and the diffraction patterns collected in the angular range 0°-160°, with step 0.1° and wavelength 1.9095 Á. The background due to the empty quartz tube (recorded at the same temperature of the sample) was subtracted from the pattern. Cell parameters, zero point, profile parameters, atomic positions and isotropic thermal factors for all the ions were refined.

X-ray powder diffraction data were collected using a two-dimensional, 2D, detector on a finely powdered sample packed in kapton capillaries. The experiments were conducted using synchrotron X-rays with the wavelength of 0.107980 Å at the 11-ID-C beam line at the Advanced Photon Source (APS) at Argonne National Laboratory at room temperature. The data were collected using a GE amorphous Si large panel 2D detector. In order to avoid saturation of the detector, each measurement was carried out in multiple exposures. Each exposure lasted 5 s and the sample was exposed ten times to improve the counting statistics. The 2D data sets from the sample were combined and integrated using the program FIT2D[21] before further processing. Data from an empty container were also collected to subtract the container scattering.

Pair Distribution Functions, PDF - Pair Distribution Function (*PDF*) is a powerful tool for the investigation of short and medium range both in amorphous and crystalline materials. For crystalline materials *PDF* has a central role to determine deviation of short-range order from the average structure. *PDF* describes the probability of finding any two atoms at given interatomic distance *r*. The *PDF* can be calculated from the Bragg intensities and from the diffuse scattering intensities. The particular feature of *PDF* is that it can discriminate between short-range order, represented by finite non-random displacements from ideal crystal structure, and random displacements of the atoms. The experimental *PDF*, *G(r)*, or radial distribution functions given by $4\pi r^2 G(r)$ are directly

obtained from diffraction data by the means of Fourier Transform of the normalized total structure factor *S(Q)* where *Q* is given by

$$Q = \frac{4\pi(sin\Theta)}{\lambda} \qquad (2.2)$$

thus *S(Q)* is the measured intensity corrected for background, Compton and multiple scattering, absorption, geometric and other instrumental factors. Experimental factors can strongly influence the quality of the experimental *PDF* data, principally the Fourier termination errors, resolution and counting statistic. Termination errors are minimized by measuring up to the largest possible *Q* value, that is limited by the instrumental highest diffraction angle available.

For the *PDF* analysis the corrected total scattering structure function, *S*(*Q*), was obtained using standard corrections[22] with the program PDFGETX2[23] Finally, the *PDF* was obtained by Fourier transformation of *S*(*Q*) according to

$$G(r) = \frac{2}{\pi}\int_0^{Qmax} Q[S(Q) - 1]\, sin(Q_r)dQ \qquad (2.3)$$

A Q_{max} =31 Å^{-1} was used. Modelling of the experimental *PDF* data was carried out with the aid of PDFGUI and PDFFfit2 software.[24]

Rietveld refinements **-** The diffraction patterns were analyzed according to the Rietveld method[25,26] by means of the Fullprof software package.[27] The Rietveld method is based on the knowledge of the basis structural parameters of the considered structure (space group, cell parameters, atomic coordinates), of the kind of measurements (kind of radiation, wavelengths, angular range) and of the experimental set up. This information is used to calculate a theoretical diffraction pattern. The difference between the experimental and the calculated pattern is minimized according to a multi-parameters non-linear best-fit procedure, in order to find a local minimum. The quality of the fit is evaluated

by the means of particular agreement factors like R_{wp}, R_{exp}, X^2; for a detailed description see Ref. 28.

Solid State NMR **-** ^{27}Al Magic Angle Spinning (MAS) NMR spectra were acquired at 104.2 MHz on a 400 MHz Bruker spectrometer, equipped with a 4 mm probe (spin rate 13 kHz), and at 195.46 MHz on a 750 MHz Bruker spectrometer equipped with a 2.5 mm probe (spin rate 33.3 kHz). The spectra were acquired with a single-pulse sequence using a ~15° pulse, *i.e.* under quantitative conditions.[29] All spectra were referenced to a 1M aqueous solution of $Al(NO_3)_3$. Multiple Quantum Magic Angle Spinning (MQMAS) NMR spectra were acquired on the 16.7 T Bruker spectrometer with the shifted-echo pulse sequence with acquisition and processing of the full echo[30] using radio-frequency fields of 150 kHz and 5 kHz for 3Q excitation/reconversion and selective π pulse respectively. The 1D spectra were analysed using the Extended Czjzek model, recently described by Le Caër and co-workers[31] which allows drawing a continuous evolution between a perfectly defined site (defined by a given set of the quadrupolar coupling constant C_Q and asymmetry parameter η_Q) and a statistical disorder. The DMfit program[32] was used. A purely statistic disorder model such as the Gaussian Isotropic Model (Czjzek, d=5) model[33] has also been used as it is seen to give the best results.

Simulation calculations **-** The simulation method used is based on the minimization procedure of the energy of the considered system. This method is based on the setting of a model of potentials defining the energy of the considered system as a function of atomic coordinates; in this contest it is also possible to evaluate the presence of defects.[34,35] Solid oxides are generally well described using the Born model, that distinguishes between the long range interactions (treated according to the Coulomb law) and short range interactions (for which overlapping of electron

density and Van der Waals interactions are considered). Short range interactions are treated using Buckingham potential, Φ, defined as

$$\Phi = A_{ij}\, exp\left(-\frac{r}{\rho_{ij}}\right) - \frac{C_{ij}}{r^6} \qquad (2.4)$$

Where A_{ij}, ρ_{ij} and C_{ij} are interaction parameters between atoms i and j at the distance r. These parameters can be optimized with a best-fit procedure starting from experimental structural data. The quality of the fit is evaluated considering the difference between the experimental and calculated structural parameters.
In order to consider the polarizability of the ions, the Dick and Overhauser shell-model is considered,[36] it couples to the core (with mass and charge $X|e|$) a shell (with charge $Y|e|$ but no mass) trough a isotropic spring defined by a constant k in such a way that $(X+Y)|e|$ corresponds to the total charge of the ion.
Static lattice simulations based on energy minimization techniques described above embodied in the GULP code[35] were used to calculate the minimum energy configuration of the perfect lattice characterized by different local arrangements of the La and Sr cations. For this purpose, simulation boxes containing approximately 4000 atoms and treated in $P1$ symmetry were used. In particular, the results related to three distributions and the one related to the average model will be compared:

- Ordered distribution. Ordered arrangement of alternating La and Sr cations in each direction (named *ordered structure* in the following);

- Pseudo-random distribution. Pseudo-random distribution of the La and Sr cations in each direction (named *disordered structure* in the following), where a certain

degree of disorder has been introduced manually in the perfect distribution of La and Sr of the ordered system;

- Random Distribution. Random distribution of the La and Sr cations in each direction (named *random structure* in the following), where a binomial distribution of La and Sr on site *A* has been obtained by a random numbers generation.

- Average Distribution. For the sake of completeness, a simulation box with the same dimension but treated in space group *I*4/*mmm* with partial occupancy of the La/Sr site (named *average structure* in the following) was also constructed to represent the average structure obtained by analysis of the diffraction data.

The large size of the simulation boxes was chosen in order to obtain a statistical representation of different local environments for the Al site. It should be acknowledged that such a large number of La and Sr cations ideally sharing the same site give origin to a huge number of possible configurations for this system, consisting of different dispositions of the La and Sr cations on the available sites. The average structure observed experimentally is interpreted as a spatial average of the local arrangements corresponding to different energetically accessible energy minima. The exploration of all the possible energetically accessible energy minimum configurations was beyond the scope of the present work and only a limited number of configurations were considered, with the aim to provide only qualitative information to support the experimental evidences of the study.
The lattice energy minimization was carried out under constant pressure, where the energy of the system is minimized with respect to ionic coordinates and unit cell dimensions. These

calculations take no explicit account of thermal motions within the materials, *i.e.* all the calculations are carried out at 0 K. Table 2.3 reports the potentials and shell model parameters used for the calculation for the $LaSrAlO_4$ system in the *I*4/*mmm* and *P*1 space groups. Starting structural parameters were those derived by the combined X-ray/neutron diffraction refinement in this study (Table 2.1).

2.3 – RESULTS AND DISCUSSION

2.3.1 –Diffraction analysis

The synthesis of the compound was carried out according to sol gel method and checked through laboratory XRD as described in the methods section. To obtained detailed and quantitative structural information, room temperature neutron and synchrotron X ray powder diffraction measurements were collected and analyzed. Figure 2.3a shows the Rietveld refined room-temperature neutron diffraction pattern of $LaSrAlO_4$. The pattern can be unequivocally indexed in the tetragonal *I*4/*mmm* space group, without any detectable deviations from this symmetry.
There are no spurious reflections, indicating the single-phase nature of the synthesized compound. Analysis of the X-ray powder diffraction pattern (Figure 2.3b) confirms this result. In particular, due to the complete absence of superstructure peaks or anomalies in the expected peaks intensities, no long range ordering of the La and Sr sites can be deduced from the available data, therefore confirming a random distribution of La and Sr in the average structure.

The structural parameters derived from the combined X-ray/neutron pattern refinement are listed in Table 2.1 together

with reliability factors. These are in very good agreement with those previously determined for this composition from single crystal X-ray diffraction[13] and give a detailed description of the long-range structure of this system represented in Figure 2.2.

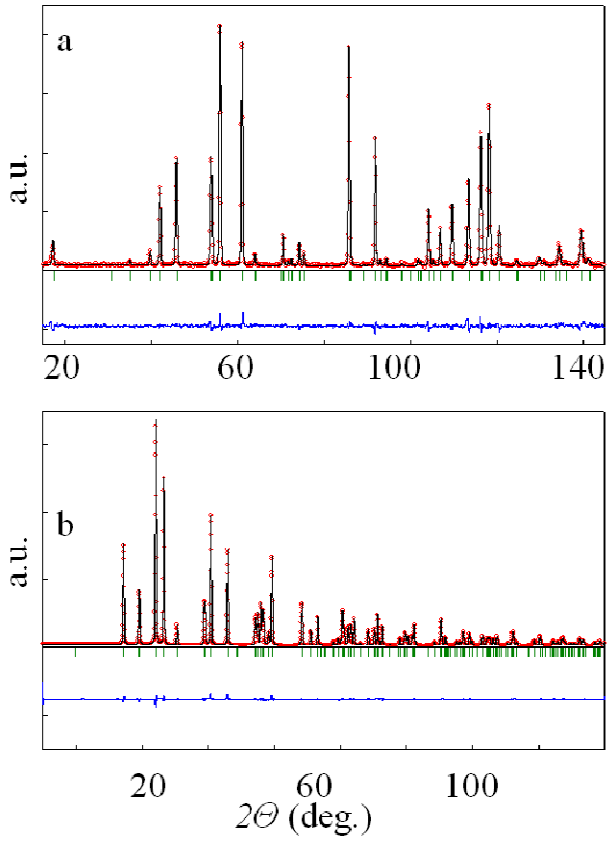

Figure 2.3 – Rietveld refinement of room temperature a) neutron diffraction powder data; b) synchrotron X ray diffraction powder data for $LaSrAlO_4$ sample. Experimental data (red), calculated profile (black), Bragg peaks positions (green) and difference profile (blue).

Atom	*x*	*y*	*z*	*Biso (Å²)*
Al	0	0	0	0.62 (4)
La/Sr	0	0	0.358 (1)	0.53 (1)
O1	0	0.5	0	0.51 (4)
O2	0	0	0.163 (2)	0.84 (5)

Atomic couple	*Distance (Å)*
Al-O1	1.878 (1)
Al-O2	2.057 (1)
Al- Sr/La eq	3.204 (1)
Al- Sr/La ax	4.527 (1)

Table 2.1 – Refined lattice parameters and atomic coordinates for $LaSrAlO_4$ structure for combined X-ray and neutron powder diffraction data analysis. Space group: I4/mmm, cell parameters: a = 3.75576 (5) Å, c = 12.6377 (2) Å , V = 178.264 (4) Å³ ;reliability factors: (a) neutrons: R_p 13.6; R_{wp} 10.2; X^2 =1.81. (b) X ray: R_p 5.13; R_{wp} 5.89; X^2 =1.91; In the bottom panel selected inter atomic distances.

2.3.2 – NMR study

As was already underlined, in the structure there is a source of disorder that is the mixed occupancy site, which is formally occupied by La and Sr in the same quantity. To complete the structural characterization of the system further investigations are needed, particularly to determine the local deviation from the average structure caused by particular disposition of La and Sr. These two cations can distribute over the site with different arrangements, potentially giving origin to different local situations for the Al. In order to completely define also the local environment of aluminum, solid-state NMR measurements were performed. ^{27}Al solid-state NMR is a good tool to investigate possible local deviations from the average structure in crystalline

materials. In fact, ^{27}Al has a nuclear spin I = 5/2, and a relatively high electric quadrupole moment (14.7 fm^2), so its MAS spectra are normally dominated by the 2-nd order electric quadrupolar interaction which is a good probe of the local order, as discussed in Chapter 1.[37] Moreover, the ^{27}Al quadrupolar coupling constants, C_Q, are not excessively large (of the order of a few megahertz) which generally allows to obtain reliable chemical shift information. In particular, in the case of aluminum oxides – both crystalline and amorphous – it is possible to discriminate between tetrahedral (chemical shift, $\delta > 50$ ppm) and octahedral ($\delta \sim 0$ ppm) Al coordination.[37,38]

As quadrupole Hamiltonian strongly depends on the applied magnetic field, as discussed in Chapter 1, measurements at different field were collected to better evaluate structural models. Figure 2.4 shows the 1D MAS spectra of $LaSrAlO_4$ obtained at 9.4 T and 17.6 T, respectively.

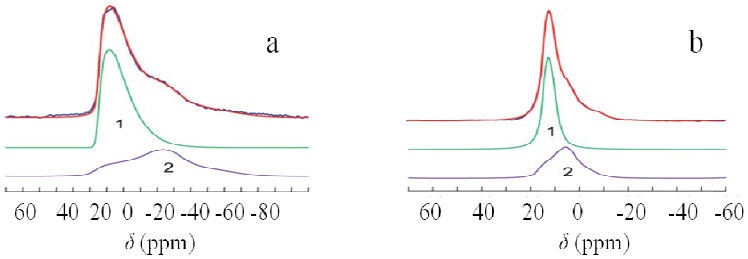

Figure 2.4 – ^{27}Al one pulse MAS NMR spectrum a) at 9.4 T and b) 17.6 T. Experimental data (blue), best fit (red), site 1 component (green), site 2 component (violet).

Figure 2.5 shows the 2D MQMAS spectrum obtained at 17.6 T. From the isotropic axis of the MQMAS spectrum we can appreciate the presence of two non-equivalent aluminum sites in the crystalline structure even if still partially overlapped.

According to this, both the 1D and the 2D spectra were fitted with the model above described, and the best-fit parameters are reported in Table 2.2.

Experiment	δ_{iso} *(ppm)*	$\Delta\delta_{iso}$ *(ppm)*	C_Q *(MHz)*	ΔC_Q *(MHz)*	η_Q	*Int (%)*
			Site 1			
1D 9.4 T	15.1	3.4	4.25	1.02	0.2	56
1D 17.6 T	15.5	3.2	4.77	2.79	0.5	59
MQMAS	15.5	2.1	4.40	_	_	50
			Site 2			
1D 9.4 T	17.0	3.8	7.55	1.11	1.0	44
1D 17.6 T	17.0	7.2	7.55	1.11	1.0	41
MQMAS	18.0	3.8	6.29	2.27	0.9	50

Table 2.2 Best fit parameters for experimental data presented in Figure 2.4 and 2.5.

Under the assumption that the spectra are dominated by two contributions very satisfactory simulations for all spectra were obtained, showing a good consistency among the 1D and the 2D experiments. Those experiments hence strongly support the existence of two octahedral aluminum sites: site 1 is characterized by an isotropic chemical shift of ~15.5 ppm, and a quadrupolar coupling constant, C_Q ~ 4.5 MHz. Site 2 is characterized by an isotropic chemical shift of ~17 ppm, and a quadrupolar coupling constant, C_Q ~ 7.5 MHz (those parameters are to be understood as mean values of a Gaussian distribution). All these parameters are retrieved from the quantitative 1D experiments, the MQMAS experiment being known to favor sites with moderate quadrupolar coupling constants with respect to large ones, so leading to an underestimation of the latter.

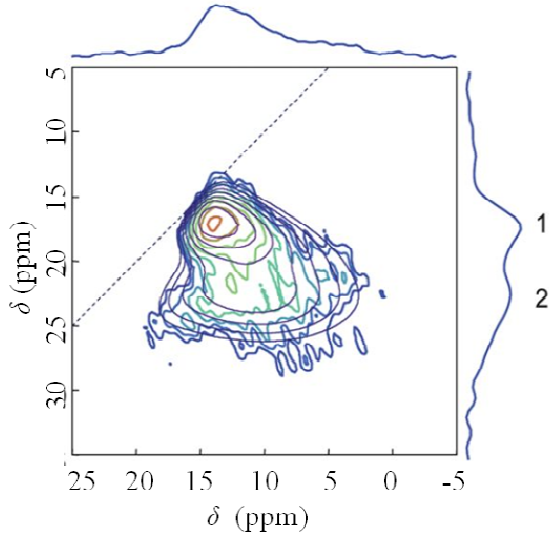

Figure 2.5 – ^{27}Al MQMAS NMR spectrum at 17.6T. Experimental (colored) and best fit (black). Direct dimension on horizontal axis and indirect dimension (isotropic) in the vertical axis.

The MQMAS spectrum, on the other hand, confirms the difference in line shape between the two sites: as clearly seen from the 9.4 T 1D experiment, site 1 (small C_Q) displays a line shape with a sharp left edge and a long decaying right tail typical of the purely statistic disorder model used for accounting for ^{27}Al spectra in glasses.[31,39] Moreover, it is for this site that the largest deviation in C_Q is seen between the 9.4 T and 17.6 T, and this potentially points to a complex line shape consisting of several distinct overlapping sites with close-to-identical δ_{iso} values. In the 9.4 T experiment, site 2 is characterized by a large C_Q value which determines its structured shape. Generally speaking, the unusually large quadrupolar coupling constant values observed here for six-fold

coordinated aluminum are noteworthy, as they call for octahedra with appreciably distortions. This is especially true for site 2 for which the asymmetry parameter η_Q is close to 1.0, evidencing hence a strong deviation from the cylindrical local symmetry of this octahedral site. Concerning the relative intensities, the quantitative 1D spectrum at 750 MHz gives a ratio 56:44 between sites 1 and 2. However, a ~10% error should be accounted for due to baseline distortions.

The task to understand the structural features underlying these two NMR sites is not trivial. In fact, the ^{27}Al NMR spectrum of a K_2NiF_4-type aluminum compound is here reported for the first time, so direct information for peaks assignment are not available. At the same time, it was not possible to prepare single-phase reference compounds with different La/Sr ratios, since varying the La:Sr ratio in order to increase the La content in the sample resulted in a La_2O_3 secondary impurity phase, as already reported in the literature.[40] Therefore, the proposed assignments are based on NMR studies performed on other Al/La and Al/Sr oxide compounds. Multinuclear NMR studies on LaNaY zeolites[41] and La–Si–Al–O–N oxynitride glasses[42] were recently reported. In particular, Hunger et al.[41] showed that the substitution of La^{3+} for Na^+ in the SI′ position of the sodalite cage gave origin to a broad Gaussian component shifted upfield by about 15 ppm with respect to the ^{27}Al peak in tetrahedral coordination. This chemical shift was attributed to the strain of the Al-O-T (where *T* is a metal ion) bonds induced by the La^{3+} cations. The effects of strontium as aluminum neighbours on ^{27}Al NMR spectra have been studied in fluoroapatite glasses and glass ceramics for biomedical applications,[43] magnetoplumbite-like structures,[44] and other strontium aluminates.[47] In all cases, no significant effects have been recognized. In particular, Hill et al.[43] reported that complete Sr for Ca substitution did leave the ^{27}Al MAS NMR spectrum substantially unchanged.

Coming back to Figures 2.4 and 2.5, the existence of two peaks with different quadrupolar coupling constants and chemical shifts is related to a significantly different distortion of the AlO_6 octahedra, that is likely to be the result of different arrangements of the La/Sr ions in the proximity of the Al site. As shown in the right part of Figure 2.2, 10 La/Sr sites represent the next-nearest neighbors of Al and are assumed to directly influence the AlO_6 octahedral distortion. Based on the average structure reported in Table 2.1, each AlO_6 octahedron has the same distortion, with four Al-O^1 bond lengths of 1.878 Å and two Al-O^2 bond lengths of 2.057 Å. On a local scale, however, the NMR spectrum predicts the presence of at least two different Al environments characterized by different octahedral distortions. The problem of local structure in $AA'AlO_4$ system has been already deeply investigated by the means of EPR technique on single crystal samples of very similar composition. EPR lines on single crystal $LaSrAlO_4$:Co present significant broadening at any orientation of the crystal due to the local distortion of the crystal field at the site of Co (substituting Al) related to the random distribution of Sr/La.[45] Similar studies were performed also on single crystal of $YCaAlO_4$: Fe and $LaCaAlO_4$: Fe with iron on the site of Al. Also in this case different configurations of Y/Ca cause broadening of the EPR line and the presence of different EPR lines in place of the single line expected from a single crystallographic site.[10,46] For these cases it has been stressed the presence of different possible configurations of the two cations on the *A* site, with different radius and charge, on the same crystallographic position, as source of fluctuating crystal field at the site of aluminum. Differences between ordered and disordered configuration of cations around the aluminum site can change the local symmetry of his sites leading to the presence of different lines in the EPR spectrum. Furthermore, also local deviations from the average ratio 1:1 of the two *AA'* cations can be present leading to further complications.[46]

2.3.3 – Pair Distribution Function analysis

Further information about local situation can be obtained by *PDF* analysis. Figure 2.6 shows the experimental *PDF* obtained from the total scattering data of the system under investigation up to 10 Å together with the results of the fit obtained using as starting model the average structure summarized in Table 2.1. Fitted parameters were the scale factor, the correlation parameters (which takes into account the correlated motion of atomic pairs at low *r*), lattice parameters, atomic positions and isotropic atomic displacement parameters (*adp*).

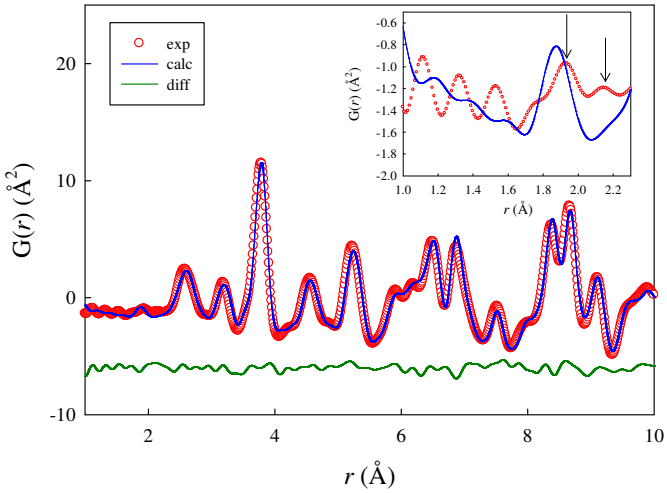

Figure 2.6 – Experimental PDF of $LaSrAlO_4$ with fitting based on the average structure model.

As can be appreciated from Figure 2.6, the average structure model well reproduces the experimental PDF in most of the *r* range considered (R_{wp} for this refinement is 11.7%). However, as highlighted in the inset of Figure 2.6, the average model fails to

describe, in terms of both position and intensity, the peaks at low *r* indicated with an arrow. We recall here that in Figure 2.6 all the peaks at *r* lower than 1.8 Å, whose intensity clearly decays with distance, can be safely attributed to ripples due to the truncation of the *G*(*r*) at finite *Q*. The two peaks indicated with arrows are instead representative of the shortest bond lengths in the samples. These, according to the fitted average structure model, pertain to the first Al coordination sphere, *i.e.* Al-O^1 and Al-O^2 distances, and appear to be largely different from the average model itself. However, analysis of the data reported in Figure 6 does not allow to independently suggest or support at this stage the experimental NMR evidence of the existence of at least two differently Al distorted environments at the local scale. The direct experimental evidence that can be extracted from the inspection of Figure 6 is only that the local structure (1-3 Å) cannot be properly described by the average structural model.

2.3.4 - Calculations

In order to search for the right interpretation of the experimental data, atomistic simulation calculations were performed. Table 2.3 reports the Buckingham potentials and shell model parameters used for calculation. From the relaxed atomic coordinates, calculated radial distribution functions (*RDFs*) for the Al-O bond pairs have been derived using a step Δr = 0.05 Å. As shown in Figure 2.7, these differ significantly for the four configurations we considered. In particular, for the average structure the first peak is centered at 1.95 Å and the second peak is centered at 2.1 Å; the intensity ratio between the two peaks is approximately 2:1. This is consistent with the average structure model, where each Al octahedron is characterized by four shorter Al-O^1 bonds and two longer Al-O^2 bond lengths. However, this intensity ratio of 2:1 is not representative of the intensity ratio in

the experimental *PDF*. In the experimental case reported in Figure 2.6 the intensity ratio is approximately 4:1.

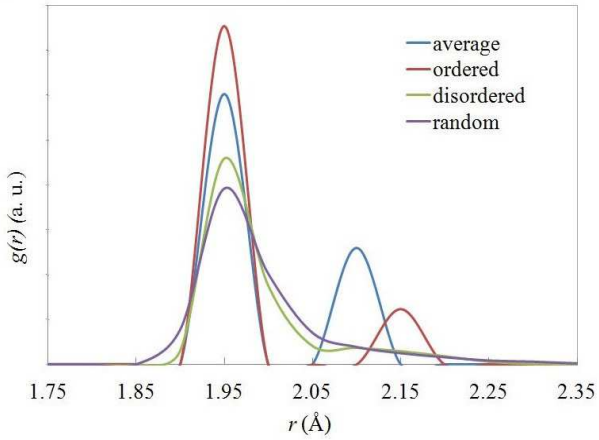

Figure 2.7 – Calculated Al-O radial distribution functions for the average (blue), ordered (red), disordered (green), random (purple) structural models.

For the ordered, the disordered and the random models, the intensity ratio between the two peaks is considerably different from 2:1. In fact, it is close to 5:1 for the ordered model, and close to 3:1 for the disordered and the random ones, respectively, as estimated on the basis of rough deconvolutions.

Atomic couple	***A (eV)***	***ρ (Å)***	***C (eV)***	***Y (e)***	***K (eV/ Å$_2$)***
La^{3+} - O^{2-}	1655.30	0.359	0	-0.25	750
Sr^{2+} - O^{2-}	1400.00	0.35	0	1.33	21.43
Al^{3+} - O^{2-}	1329.82	0.3087	0	2.04	196.3
O^{2-} - O^{2-}	22764.3	0.149	43	-2.239	42

Table 2.3 – Buckingham potential and shell model used for GULP calculation.

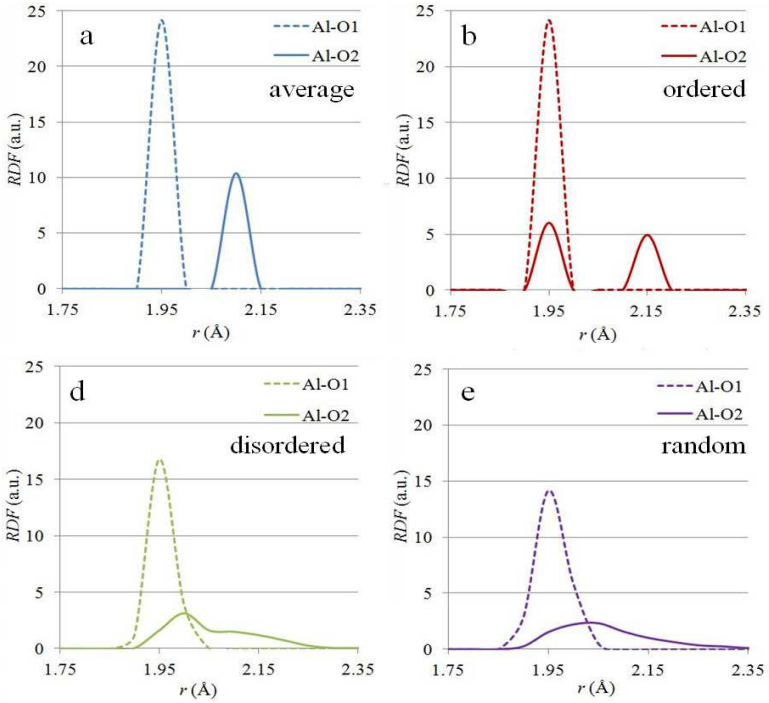

Figure 2.8 – Calculated partial Al-O1 and Al-O2 radial distribution functions for the average (a), ordered(b), disordered (d), random(e) structural models.

It is reasonable to conclude that in these cases part of the apical Al-O^2 bond pairs have distances comparable to the Al-O^1 bond contributing therefore to the first peak. This has been proven from the analysis of the calculated partial Al-O^1 and Al-O^2 radial distribution functions presented in Figure 2.8.

Investigation of the Al-O bond lengths in the ordered system (Figure 2.8b) shows that two distinct sets of Al-O^2 apical distances

are present (1.95 Å and 2.15 Å), while the Al-O^1 equatorial distances are all equal (1.95 Å). From the analysis of the AlO_6 environment in the calculated structure, it was possible to distinguish that when La is present in a position labeled ***a*** in Figure 2.2, the closest apical Al-O^2 distance becomes sensibly longer than the distance present in the average structural model (~ 2.15 Å *vs* 2.075 Å) while if Sr is present in a position labeled ***a*** in Figure 2.2, the apical Al-O^2 distance becomes sensibly shorter than the distance present in the average structural model (1.95 Å *vs* 2.075 Å) and close to the Al-O^1 value.

The computational results obtained for the ordered model suggests that:

- La^{3+} attracts the oxygen ion in apical positions more than Sr^{2+} thanks to the charge effect;
- In this system, Sr in positions ***a*** will in general promote the existence of more regular AlO_6 environments;
- the cations placed in the positions labeled ***a*** in Figure 2.2 have the largest effect on the structural distortion of the AlO_6 octahedra respect to the effect of different cations in ***b*** position;
- the possible different degrees of distortions of the AlO_6 octahedra, as revealed by NMR measurements, are mainly related to the spread in the Al-O_2 bond lengths. This should be expected, not only because of the highly regular disposition of La and Sr in the ordered model, but rather because the equatorial O^1 positions are shared between AlO_6 units to form the perovskite-type layers (see Figure 2.1 and 2.2) and, as a consequence, have less "freedom" of shift compared to the apical O^2 positions that point towards the rock-salt layer. Similar considerations were

made to explain EPR lines and line broadening in related systems.[10,46]

This aspect may be reasonably transferred to the other models. Because of the regular disposition of La and Sr ions in the ordered model, even though the Al-O^2 bond pairs are split in two sets, all of the AlO_6 octahedra present the same distortion, which would result in a single NMR peak. Moreover, the ordered arrangement of La/Sr ions at long range should result in superstructure reflections which are not visible at all in the diffraction patterns and that were never evidenced for such systems.[10,46] This La/Sr ordered superstructure is therefore incompatible with the experimental evidences, but its analysis has been useful to identify trends and consequences in the local arrangement of the oxygen atoms in a relatively simple model, if compared to the disordered or the random ones.

Figure 2.7 shows that the spread in calculated bond lengths for the disordered model is much higher than that observed for the ordered system, although two main broad peaks, the first one being highly asymmetric, can still be discriminated. The first peak has a maximum at approximately 1.95 Å and the second centered at approximately 2.1 Å. As shown in Figure 2.8c, all the Al-O^1 bond pairs (peak maximum at 1.95 Å) and approximately half of the Al-O^2 bond pairs (peak maximum at 2.0 Å) contribute to the first peak. Only Al-O^2 bond pairs fall under the second broad peak.

Finally, as shown in Figure 2.8d, for the random model the Al-O^2 bond pairs are represented by a broad and asymmetric single-mode distribution with peak maximum at approximately 2.05 Å.

As previously stated, the different degrees of distortions of the AlO_6 octahedra in the $LaSrAlO_4$ system will be mainly related to the spread in the Al-O^2 bond lengths. It is therefore important to highlight here that, compared to the random model, the

disordered model gives rise to a bimodal distribution of bond lengths, which should result in a bimodal distribution of octahedral distortions. This is consistent with the NMR data that show the existence of two main local environments characterized by different octahedral distortions. In contrast, the single-mode distribution of Al-O[2] distances of the random model (obtained, as previously stated, by generating a binomial distributions of the Sr and La cations) would result in a broad single-mode distribution of octahedral distortions, in disagreement with the NMR findings.

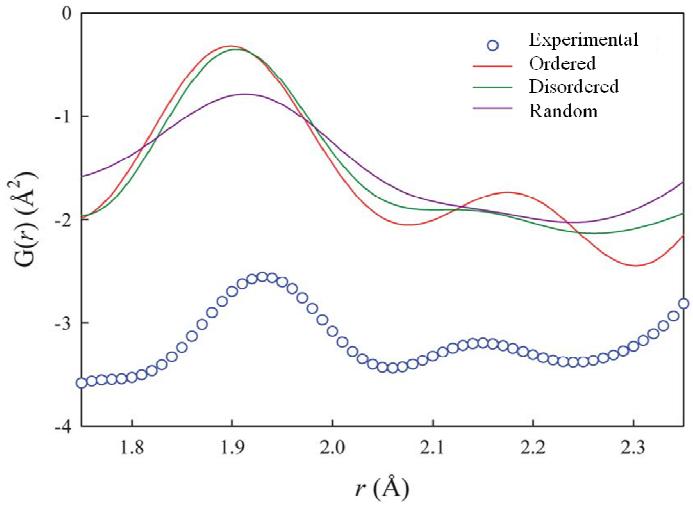

Figure 2.9 – Experimental PDF data (blue dots) and calculated pair distribution functions for ordered (red) disordered (green) random (violet) models.

On the basis of the abovementioned considerations, the NMR site 1 can be likely assigned to AlO_6 octahedra with predominantly couples Sr-Sr in ***a*** positions (low distortion), whereas the site 2 can be due to La-La couples (high distortion). This could also justify the relative intensities of the two peaks (see Table 2.2). The

distribution of C_Q values should account for the more populated mixed configurations. In order to confirm the assignments proposed above, we have performed *ab-initio* calculations of NMR parameters with the Gaussian0334 software. A simple cluster of the form (La,Sr) O^2-Al$(OH)_4$ has been used to investigate the effect of the presence of either La or Sr nearby the apical oxygens O^2. A complete C_{4v} symmetry has been kept with aluminum-oxygen distances fixed to those known from the structural elucidations, *i.e.* d(Al-O^1) = 1.903 Å, d(Al-O^2(Sr)) = 1.921 Å, d(Al,O^2(La)) = 2.113 Å, and with d(Sr-O) = 2.511 Å and d(La-O) = 2.451 Å. A 6-311+G(d) basis set has been used for Al, O and H atoms whereas the Electronic Core Potential LanL2DZ is used for Sr and La. The ^{27}Al C_Q is found to be 8.0 MHz for the (Sr,Sr) cluster, increases to 13.9 MHz for the mixed (Sr,La) one and reaches a value of 19.4 MHz for the (La,La) environment. The isotropic shielding decreases by 2.8 ppm going from (Sr,Sr) (642.9 ppm) to (Sr,La) (640.0 ppm) and further more by 12.3 ppm for (La,La) (627.7 ppm).

Even though the simplicity of the clusters prevents us from discussing those numbers (*e.g.* C_Q is clearly overestimated), the trends can be trusted as markers of the structure/NMR parameters relationship. They are fully consistent with the above assignments of the experimental lines: increase of the isotropic chemical shift δ_{iso} and quadrupolar coupling constant C_Q upon substituting Sr atoms by La atoms on the apical positions.
Figure 2.9 shows a comparison between the experimental and the calculated PDFs for the completely ordered, disordered and random cation distribution, respectively. The calculated relaxed coordinates have been used as input for the generation of the calculated PDF to be compared with the experimental PDF data within the same software. Due to the extremely large number of parameters for the super-cells in *P*1 symmetry, with the exception of the average structure model (Figure 2.2), it was not possible to

fit the experimental data against the calculated models; experimental and calculated data were simply compared in the range of 1.75 - 2.35 Å. To this end, the calculated *PDFs* were generated with the same resolution found for the experimental *PDFs* and by assigning to the atoms an isotropic thermal factor U_{iso} = 0.003, which is a reasonable value expected at room temperature for similar systems.
We recall here that the data presented in Figure 2.7 were not affected by thermal vibration, being the result of lattice energy minimizations carried out under constant pressure at 0 K. As can be appreciated from the comparison of the *PDFs* presented in Figure 2.9, the experimental data are clearly characterized by the presence of two distinct peaks located around 1.92 Å and 2.15 Å. Two distinct sets of bond pairs are found in the ordered model for the first coordination shell. The disordered and the random models are characterized as well by two groups of bond pairs but with different relative intensities and peaks positions with respect to the totally ordered model. A quantitative assessment of the relative intensities of the experimental PDFs could not be reliable due to the low-*r* position and low intensities of the two first peaks in the PDF. However, we may qualitatively observe that the peak positions and relative intensities seem to fall in between the completely ordered and the random cation distribution models suggesting that, most probably, the real situation can be represented by a partially ordered (or non-random) one. This conclusion is also supported by the average structure analysis and by NMR data.

2.4 - CONCLUSIONS

In this study the differences between the average and the local structure of $LaSrAlO_4$ were investigated by the combined use of neutron and synchrotron X-ray diffraction as space-averaged

probes, pair distribution function analysis (*PDF*) and ^{27}Al MAS-NMR as local probes.

It was possible to highlight that, while the average structure predicts the presence of a single AlO_6 octahedral environment, at least two distinct Al sites, characterized by different distortions, have been experimentally observed.

This is not the first observation of a difference between average and local structure in K_2NiF_4-type compounds, in particular with reference to the *B* site. However, there is a relevant and important difference between this and the previous study on $La_{2-x}Sr_xCuO_{4-d}$,[9] where the existence of two distinct Cu sites was evidenced through NMR. In fact, in $La_{2-x}Sr_xCuO_{4-d}$ this result was attributed to electronic effects on the Cu site itself (hyperfine interactions). In this case, much more subtle differences between distinct Al sites which experience different next-nearest neighbor atoms (La or Sr), have been observed through a sophisticated 2D NMR experiment.

Thanks to the use of atomistic modeling techniques, it was possible to show that the AlO_6 octahedral distortion is mainly influenced by the spread in Al-O_2 (apical) distances introduced when the structure deviates from the ideal average structure model. These distances are largely dependent on the distribution of La and Sr in the first cation coordination sphere around Al. In particular, La in apical position will promote the existence of more distorted (elongated) AlO_6 octahedra compared to Sr. This is mainly attributed to a charge effect, as La and Sr have similar ionic radii (r_{La} =1.216 Å; r_{Sr} = 1.31 Å).

By combining the experimental and computational results, we have determined that the average structural model, based on partial occupancy of the La/Sr site, is not able to reproduce the structure at the local scale: the symmetry operations of the space group don't allow to take into account local distortions due to the La and Sr distribution over the available site. Structural models with long range ordering of La and Sr are to be excluded because

of the absence of superstructure peaks in the diffraction patterns; moreover, a long-range order of La and Sr in each crystallographic directions predicts the presence of a single Al environment resulting in a single NMR peak. A random distribution of La and Sr throughout the structure, although compatible with the diffraction data, is not able to represent the NMR data because the resulted single-mode distribution of octahedral distortions is expected to produce a single broad NMR peak. A disordered arrangement of La and Sr over the available sites, *i.e.* a situation in between the ordered and the random model, is instead shown to be compatible with all the experimental data, in particular with the presence of two ^{27}Al NMR peaks. The number of possible disordered configurations compatible with the experimental data is extremely large and, based on the available results, it is not possible to clearly identify the precise configuration that represents the experimental situation. However, the results presented in this study confirm that La and Sr are, on average, randomly distributed throughout the structure, but imply that the situation is considerably more complex at short range. The most probable situation is a pseudo-random distribution of the two cations over the available crystallographic sites that give rise to at least two different local Al environments: one, more distorted, where the AlO_6 octahedra have mainly La in apical positions and another where Sr is predominant.

The combined use of powerful experimental techniques has allowed us to gain significant insights into the structural properties of this material, a representative example of a class of compounds with K_2NiF_4-type structure that presents numerous interesting physical properties and relevant technological applications. In particular, we have highlighted differences between the average and local structure of a crystalline material, which only the combination of structural techniques with different

length scales can produce. This work also shows the increasing importance of the combined use of experimental and computational techniques in the study of complex oxide systems.

2.5 - REFERENCES

1. S.N. Ruddlesden, P. Popper, *Acta Crystallogr.,* 10 (1957) 538.
2. S.N. Ruddlesden, P. Popper, *Acta Crystallogr*., 11 (1957) 54.
3. J.A. Kafalas, J.M. Longo, *J. Sol. State Chem.,* 4 (1972) 55.
4. P. Ganguli, C.N.R. Rao, *J. Sol. State Chem.*, 53 (1984) 193.
5. A. Chrineos, R.V. Vovk, I.L. Goulatis, *J. Alloys and Comp*., 494 (2010) 190-195.
6. J. B. Goodenough, *Rep. Prog. Phys*.,67 (2004) 1915.
7. I.B. Sharma, D. Singh, *Bull. Mater. Sci.,* 21 (1998) 363-371.
8. T. He, C. Jiazhong, T.G. Galvarese, M.A. Subramanian, *Sol. State Scie.*, 8 (2006) 467-469.
9. R. Ang, Y.P. Sun, X. Luo, C.Y. Hao, X.B. Zhu, W.H. Song, *J. Phys*, 103 (2008) 103707.
10. S.K. Misra, S.I. Andronenko, *Phys. Rev. B*, 65 (2002) 104435.
11. I. Bozovic, G. Logvenov, I. Belca, B. Narimbetov, I. Sveklo, *Phys. Rev. Lett*., 89 (2002) 107001.
12. P. Aleshkevych, M. Berkowski, W. Ryba-Romanowsky, *Phys. Stat. Sol*., 218 (2000) 521-526.
13. R.D. Shannon, R.A. Oswald, J.B. Parise, B.H.T. Chai, P. Byszewski, A. Pajaczkowska, R. Sobolewski, *J. Solid State Chem*.,98 (1992) 90.
14. I. Humlicek, R. Henn, M. Cardona, *Phys. Rev. B: Condens. Matter Mater. Phys*.,61 (2000) 14554.
15. M. Sanchez-Andujar, M.A. Senaris-Rodriguez, *Solid State Sci*., 6 (2004) 21.
16. R. Ang, Y.P. Sun, X. Luo, C.Y. Hao, W.H. Song, *J. Phys. D: Appl. Phys.*,41 (2008) 045404.
17. J.E. Millburn, M.J. Rosseinsky, *J. Mater. Chem*.,8 (1998) 1413.
18. I. Zvereva, Y. Smiernov, J. Choisnet, *Mater. Chem. Phys*., 60 (1999) 63.
19. M.A. Kennard, Y. Song, K.R. Poeppelmeier, W.P. Halperin, *Chem. Mater*., 3 (1991) 672.

20. A. Magrez, M. Cochet, O. Joubert, G. Louarn, M. Ganne, O. Chauvet, *Chem. Mater*., 13 (2001) 3893.
21. A.P. Hammersley, S.O. Svensson, M. Hanfland, A.N. Fitch,D. Hausermann, *High Pressure Res*., 14 (1996) 235.
22. T. Egami, S.J.L. Billinge, "*Underneath the Bragg Peaks: Structural Analysis of Complex Materials*", Pergamon, Amsterdam/Boston, (2003).
23. X. Qiu, J.W. Thompson, S.J.L. Billinge, *J. Appl. Crystallogr*., 37 (2004) 678.
24. C.L. Farrow, P. Juhas, J.W. Liu, D. Bryndin, E.S. Bozin, J. Bloch, Th. Proffen, S.J.L. Billinge, *J. Phys.: Condens. Matter*,19 (2007) 335219.
25. H.M. Rietveld, *Acta Crystallogr*.,22 (1967) 151.
26. H.M. Rietveld, *J. Appl. Crystallogr*.,2 (1969) 65.
27. J. Rodriguez-Carvajal, *Abstracts of the Satellite Meeting on Powder Diffraction of the XVth Congress of the International Union of Crystallography*, Toulose (1990) p. 127.
28. FullProf manual, http://*www.ill.eu/sites/fullprof/*.
29. D. Fenzke, D. Freude, T. Fröhlich, J. Haase, *Chem. Phys. Lett*., 111 (1984) 171.
30. D. Massiot, B. Touzo, D. Trumeau, J.-P. Coutures, J. Virlet, P. Florian, P.J. Grandinetti, *Solid State Nucl. Magn. Reson*., 6 (1996) 73.
31. G. Le Caër, B. Bureau, D. Massiot, *J. Phys.: Condens. Matter*, 22 (2010) 065402.
32. D. Massiot, F. Fayon, M. Capron, I. King, S. Le Calvè, B. Alonso, J.-O. Durand, B. Bujoli, Z. Gan, G. Hoatson, *Magn. Reson. Chem*., 40 (2002) 70.
33. G. LeCaër, R.A. Brand, *J. Phys.:Condens.Matter*, 10 (1998) 10715.
34. Gulp manual, http://*projects.ivec.org/gulp/*.
35. J.D. Gale, *J. Chem. Soc., Faraday Trans*., 93 (1997) 629.
36. B.G. Dick, A.W. Overhauser, *Phys. Rev*., 112 (1958) 90.

37. See, for example, G. Engelhardt, D. Michel, "*High Resolution Solid-State NMR of Silicatesand Zeolites*", J. Wiley & Sons, Chichester (1987).
38. C. Leonelli, G. Lusvardi, M. Montorsi, M.C. Menziani, L. Menabue, P.Mustarelli, L. Linati, *J. Phys. Chem*., 105 (2001) 919.
39. D.R. Neuville, L. Cormier, D. Massiot, *Geochim. Cosmochim. Acta*, 68 (2004) 5071.
40. E.S. Raj, S.J. Skinner, J.A. Kilner, *Solid State Sci*., 6 (2004) 825.
41. M. Hunger, G. Engelhardt, J. Weitkamp, *Microporous Mater.*, 3 (1995) 497.
42. E. Leonova, A.S. Hakeem, K. Jansson, B. Stevensson, Z. Shen, J. Grins, S. Esmaeilzadeh, M. Edèn, *J. Non-Cryst. Solids*, 354 (2008) 49.
43. R.G. Hill, A. Stamboulis, R.V. Law, A. Clifford, M.R. Towler, C. Crowley, *J. Non-Cryst. Solids*, 336 (2004) 223.
44. L.-S. Lin-Shu, J.F. Stebbins, *J. Phys. Chem. B*, 108 (2004) 3681.
45. P. Aleshkevych, M. Berkowki, W. Ryba-Romanowski, *Phys. Stat. Sol. B*, 218 (2000) 521.
46. S.K. Misra, S. Andronenko, *Phys. Rev.* B, 67 (2003) 024425.
47. M. Capron, F. Fayon, D. Massiot, A. Douy, *Chem. Mater*., 15 (2003) 575.
48. M.J. Frisch, G.W. Trucks, H.B. Schlegel, G.E. Scuseria, M.A. Robb, J.R. Cheeseman, J.A. Montgomery, Jr, T. Vreven, K.N. Kudin, J.C. Burant, J.M. Millam, S.S. Iyengar, J. Tomasi, V. Barone, B. Mennucci, M. Cossi, G. Scalmani, N. Rega, G.A. Petersson, H. Nakatsuji, M. Hada, M. Ehara, K. Toyota, R. Fukuda, J. Hasegawa, M. Ishida, T. Nakajima, Y. Honda, O. Kitao, H. Nakai, M. Klene, X. Li, J. E. Knox, H.P. Hratchian, J.B. Cross, C. Adamo, J. Jaramillo, R. Gomperts, R.E. Stratmann, O. Yazyev, A.J. Austin, R. Cammi, C. Pomelli, J.W. Ochterski, P.Y. Ayala, K. Morokuma, G.A. Voth, P. Salvador, J.J. Dannenberg, V.G. Zakrzewski, S. Dapprich,

A.D. Daniels, M.C. Strain, O. Farkas, D.K. Malick, A.D. Rabuck, K. Raghavachari, J.B. Foresman, J.V. Ortiz, Q. Cui, A.G. Baboul, S. Clifford, J. Cioslowski, B.B. Stefanov, G. Liu, A. Liashenko, P. Piskorz, I. Komaromi, R.L. Martin, D.J. Fox, T. Keith, M.A. Al-Laham, C.Y. Peng, A. Nanayakkara, M. Challacombe, P.M.W. Gill, B. Johnson, W. Chen, M. W. Wong, C. Gonzalez, J.A. Pople, *Gaussian03*, Revision B.04, Gaussian, Inc., Pittsburgh PA (2003).

Chapter 3
The melilite series
$LaSr(Ga/Al)_3O_7$

3.1 – THE MELILITE STRUCTURE

Oxides with general formula $ABT^1{}_{(1)}T^2{}_{(2)}O_7$ belong to the large family of tetragonal melilite-like structure (space group $P\text{-}42_1m$). In this layered structure, reported in Figure 3.1, T^1 and T^2 are distinct tetrahedrally coordinated sites, whereas *A* is a large divalent alkali earth, *B* a trivalent lanthanide, both on the same eight-fold coordinated site. The T^1 site is usually occupied by divalent or small trivalent cations, whereas T^2 site can host divalent, trivalent, tetravalent or pentavalent cations. The two dimensional layers are composed by corner sharing T^1O_4 and T^2O_4 tetrahedra forming five-fold tunnels thanks to the particular connection; these layers are spaced by slabs of $(A/B)_2$ cations accommodated at the top and bottom of the tunnels.

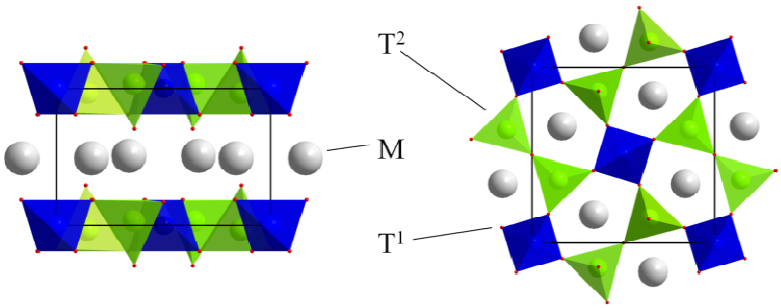

Figure 3.1 – Melilite structure view along y axis (left) and along z axis (right). T^1 site in blue, T^2 site in green, M site in grey, O sites in red.

The layered structure allows high degree of substitution, doping and exchange of cations on all the cationic sites *A*/*B*, T^1 and T^2. This makes the properties of these systems highly tunable with the introduction of proper substitutions and compositions leading to a wide variety of melilite structure compounds with interesting and relevant properties for application in many different fields.

As an example, $A_2MgSi_2O_7$ (*A* = Ba, Sr, Ca) is a class of materials characterized by high thermal and chemical stability accompanied by good biocompatibility.[0] The ease in accommodating rare earths (Eu, Dy) into the structure[0,2] gives origin to luminescence effects, making these materials good candidates for a wide range of applications such as materials for tunable solid state lasers, phosphors, photo-luminescence, mechano-luminescence, and LED technology.[0-3] Al-containing compounds such as $Ca_2Al_2SiO_7$ and $CaYAl_3O_7$ also present similar properties.[4,5] The $Ba_2MgGe_2O_7$ compound shows unusual nonlinear laser cascade effects and was therefore suggested for Raman laser frequency converters.[6] The refractive indices and the optical dispersion of these Mg/Ge oxides can be controlled by substitutions on all the three cation sites, leading to the possibility of new classes of non-linear optical materials.

The $A_2CoSi_2O_7$ (*A* = Ca, Sr) series shows a large magneto-capacitance, which indicates a strong coupling between magnetic and dielectric properties. This effect is directly related to a peculiar 2D tetrahedral networking between SiO_4 and CoO_4 units. In fact, the $Ba_2CoSi_2O_7$ composition, that has the same general formula but a different crystallographic structure, is characterized by other properties.[7]

$LaSrGa_3O_7$ is currently under study as a possible electrolyte for solid oxide fuel cells (SOFCs)[8,14] and as substrate for epitaxial films of HT superconductors and laser material when doped.[16,17] This compound becomes an interstitial oxide ion conductor when excess oxygen is introduced within the structure by modifying the

cation stoichiometry to $La_{1+x}Sr_{1-x}Ga_3O_{7+\delta}$, ($\delta = x/2$) where $x \leq 0.5$ and 0.6 were explored.[15,18] The structure undergoes a phase transition from tetrahedral to orthorhombic symmetry when x exceeds 0.5. The interstitial oxygen ions are accommodated between the layers within the five-fold channels. The average structure has been investigated and completely defined; on the other hand the characterization of the local structure and the relative distortions introduced by the presence of defects still need to be explained. Different techniques have been used and different models has been proposed[13,14,18] but both composition and electrical performance of this material remain controversial.

Al-based melilites find application in the field of optic technologies.[4-8,19] Adjustable optical properties can be obtained by proper doping with rare-earth[20,21] and substitution on the *A*/*B* site. Also substitution on the T^1 and T^2 sites is possible and leads to the huge family of the Al-Si melilite. This family of compounds also finds application in the field of solid state laser, phosphors, photo luminescence, mechano-luminescence and LED technology.[22]

The Al-Si system is relevant also in the geophysics science.[23] Study of Al-Si based compounds has always received great attention as aluminosilicates are the constituent of many relevant materials in different field (clay minerals, zeolite, concrete materials)[24,25] and their study and comprehension is fundamental for several technological applications. As in the case of melilite, the family based on Al and Si has been widely investigated;[4,26] the gehlenite $Ca_2Al_2SiO_7$ compound has received great attention over the past few decades and recently has been deeply analyzed to better understand the particular ordered $Ca_2Al(AlSi)_2O_7$ structure characterized by specific constrains for the linkage between Al and Si tetrahedral.[27]

Considering these examples, it is clear that structure and properties of melilite-type compounds are dominated by the peculiar anisotropy of the structure and the presence of defects,

substitutions and the specific local order. For a better knowledge of the melilite family and its related properties it is essential to deepen the analysis of the system, particularly by addressing the aspect of differences between local and average structure as disclosed by spectroscopic and diffraction techniques, respectively.

From the point of view of the local structure, solid-state NMR is a powerful tool for the structural analysis of highly disordered and/or compositionally very complex systems, where diffraction techniques, as well as other spectroscopies (*e.g.* IR and Raman) undergo failure or do not provide sufficient details. Moreover, recent developments of the Gauge Including Projector Augmented Wave method (GIPAW) especially devised for the computation of NMR parameters in extended solids (described within periodic boundary conditions, plane wave basis sets, and density functional theory (DFT-GIPAW)[28,29] allowed the successful prediction of chemical shifts and quadrupolar coupling constants of various crystalline and amorphous solids.[29-35] Thus, it is not surprising that the combination of one-dimensional and two-dimensional NMR spectroscopy with periodic DFT-GIPAW calculations can provide relevant information on complex solid phases.[36- 40]

In this chapter, we present the analysis of the $LaSr(Ga/Al)_3O_7$ series, proposed here for the first time. The first part of the chapter will be devoted to the accurate analysis of the $LaSrAl_3O_7$ end member of the series; the complete structural analysis will be performed thanks to a combined experimental/ computational approach. Such an approach has been recently applied to K_2NiF_4-type[41] and melilite[27] structures by choosing ^{27}Al as the main NMR nuclear probe. As already stated, ^{27}Al (I=5/2) is a quadrupolar nucleus characterized by a manageable electric quadrupolar

moment, Q (14.7 fm^2). This enables high-resolution measurements of chemical shifts and provides deep insight into the details of local ordering, such as the cation distribution around the position of interest. At the same time, the best model for the representation of the structure of the system will be identified and used in the second part of the chapter for the analysis of the whole series of mixed Ga/Al samples. The analysis of the series will be carried out by combining long range and short range techniques (*e.g.* neutron diffraction and solid state NMR), in order to better address the complexity of the system and the different sources of disorder. The NMR analysis of the mixed samples is not trivial. Two NMR active nuclei are available, ^{69}Ga and ^{71}Ga, both $I = 3/2$. ^{69}Ga is characterized by the highest natural abundance but has also the highest Q (19 fm^2), while ^{71}Ga is only 40% of natural abundance but has lower Q (12 fm^2). Gallium is chemically similar to aluminum, however well resolved gallium spectra are very difficult to obtain because its second order quadrupolar broadening of the central transition, for a given *EFG*, exceeds that of aluminum of a factor of ~ 11. We acquired both ^{27}Al and ^{71}Ga spectra in order to have a better insight into the local structure of the mixed samples. At the same time an accurate characterization of the long range structure was performed with the acquisition and refinement of neutron diffraction data; the use of neutron diffraction, in fact, can address the problem of the distribution of the two crystallographic sites as Al and Ga have significantly different neutron cross sections. The accurate selection of different techniques and their combined use can lead to the complete structural characterization of complex disordered crystal systems.

3.2 – EXPERIMENTAL SECTION

Synthesis - Syntheses were performed according to a modified sol-gel procedure. Polycrystalline powder samples of the series

$LaSrGa_{3-x}Al_xO_7$ with x = 0, 1, 1.5, 2, 3 were prepared starting from a stoichiometric amount of La_2O_3 (Sigma, 99.9% previously heated overnight at 1000°C in order to eliminate absorbed water and carbon dioxide), Ga_2O_3 and $Sr(NO_3)_2$ (Sigma, >99.0%) and $Al(NO_3)_2{\cdot}9H_2O$ (Sigma, 98.0%). La_2O_3 and Ga_2O_3 were dissolved in a solution of concentrated nitric acid at ~100°C and vigorously stirred. Proper amounts of $Sr(NO_3)_2$ and $Al(NO_3)_2{\cdot}9H_2O$ were then added to the suspension together with an excess of citric acid, as the chelating agent, and ethylene glycol as the gelation agent. Mixing at 100°C was carried out until a stable gel was obtained under continuous stirring. After complete evaporation of the water, the gel was heated at 1000°C overnight to eliminate the organic components and the nitrogen residue. The resulting powder was pressed and heated at 1200°C for 20 h, 1400°C for 6 h with intermediate grinding.

Several attempts for solid state route synthesis of the series were also performed but never gave the desired phase, as the synthesis involved the use of Al_2O_3, requiring thermal treatments in excess of 1500°C. On the other hand, classic sol-gel Pechini method was not possible since soluble Ga salts with known stoichiometry were not available. We selected Ga_2O_3 as the starting reagent for a modified sol gel synthesis and dissolved it in a concentrate solution of nitric acid in order to obtain a fine dispersion. Also $La(NO_3)_3{\cdot}6H_2O$ was replaced by La_2O_3 for the uncertainty on the hydration states of the salt. The component of the series $LaSrGa_{x-3}Al_xO_7$ will be named Ga (x = 0), Ga2Al1 (x = 1), Ga1.5Al1.5 (x = 1.5), Ga1Al2 (x = 2) and Al3 (x = 3).

Diffraction analysis - The X Ray Diffraction (XRD) patterns of the samples were collected at room temperature using a Bruker D8 powder diffractometer (Cu-Kα radiation) operating in Bragg-Brentano θ-θ geometry. The data were recorded in the 2θ range 10-100° with a step size of 0.02 (2θ) and a constant counting time

of 10 s per step. Room temperature neutron diffraction data were acquired on the high-resolution powder diffractometer SPODI at Forschungs–Neutronenquelle Heinz Maier-Leibnitz (FRM II) in Garching, near Munich (Germany). The samples were investigated at room temperature using an automatic sample changer, which is a carousel hosting up to six vanadium sample cans. As the coherent scattering cross section of vanadium is close to zero, the scattering power of vanadium is practically negligible compared to the samples. The data were collected in the angular range of 0-160° with 0.05° stepwidth and a wavelength of 1.5483 Å using a Germanium(551) monochromator.
The patterns of both X ray and neutron diffraction data were analyzed according to Rietveld refinement method[42,43] with the use of the FullProf software package.[44] Refined parameters were zero shift, scale factor, background, lattice parameters, atomic positions and isotropic thermal factors (XRD) and anisotropic thermal factor (nD).

Solid state NMR - Solid-state ^{27}Al Magic Angle Spinning (MAS) NMR spectra were collected both on a 700 MHz (16.4 T) spectrometer (Bruker) equipped with a 2.5 mm probe, operating at the Larmor frequency of 182.4 MHz, and on a 1 GHz (23.5 T) spectrometer (Bruker) equipped with a 2.5 mm probe, operating at the Larmor frequency of 260.6 MHz. All the spectra were collected at room temperature, and the chemical shifts were referenced to a standard aqueous solution of $Al(NO_3)_3$ 0.1 M. Both static and MAS spectra (25 kHz) were recorded using both one pulse and rotor-synchronized spin-echo sequences with a 90° pulse of 1.76 μs (ν_1 = 47 kHz) and 64 scans were acquired with a recycle delay 15.0 s.
In order to account for the effects of non-ideal excitation of NMR signals from large and small C_Q sites several MAS ^{27}Al NMR spectra were acquired with a variety of *RF* fields and pulse tip angles, reported in Figure 3.2.

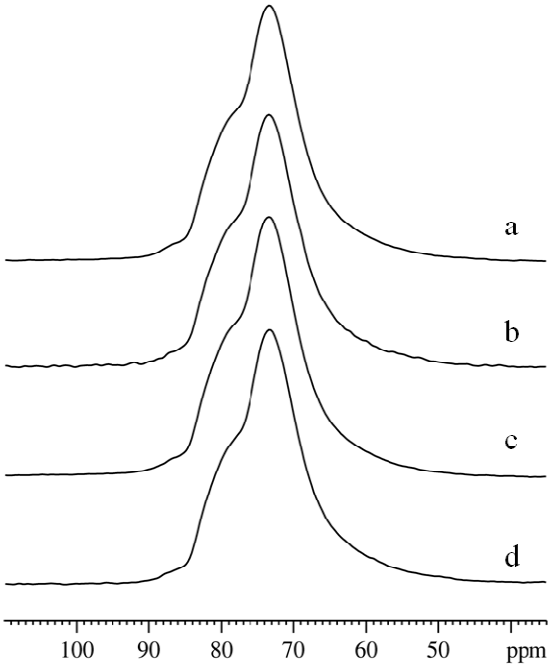

Figure 3.2 – ^{27}Al MAS solid-state NMR spectra of $LaSrAl_3O_7$ acquired using different RF field strengths and pulse tip angles. a) 1.7 μs low power (20 W) CT selective 90° pulse; b) a low power CT selective 10° pulse of 0.2 μs; c) high power (200 W) 0.53 μs selective 90° pulse; d) high power CT selective 10° pulse. The CT selective 10° pulses should provide the most uniform excitation of NMR signals from sites with near-zero and appreciable C_Q values. The similarity of the spectra acquired with CT selective 10° and 90° pulses suggests that signals from sites with a large range of C_Q values are uniformly excited under all experimental conditions. All spectra were acquired with a 25 kHz sample spinning rate and 30 s recycle delays to ensure relaxation of large and small C_Q sites. A double resonance 2.5 mm MAS NMR probe was employed.

The line shape of the spectra was insensitive to both the pulse tip angle and *RF* field, suggesting that the excitation efficiency does not strongly depend upon C_Q under the experimental conditions employed. A 2D rotor-synchronized split-t_1 (constant time)[45] 3Q-MAS spectrum, presented in Chapter 1, was acquired at 16.4 T. "Hard pulses" (ν_1 = 208 kHz) were used for the creation and conversion of triple quantum magnetization and a soft CT selective refocusing π-pulse (3.52 μs, ν_1 = 47 kHz) was employed. The 2D spectrum was acquired with 48 scans in the direct dimension and 112 increments in the indirect dimension, with the t_1 increment equal to one rotor period (40 μs).

^{71}Ga MAS NMR spectra were collected on a 1 GHz (23.5 T) spectrometer (Bruker) equipped with a 2.5 mm probe, operating at the Larmor frequency of 305.007 MHz. All the spectra were collected at room temperature, and the chemical shifts were referenced to a standard aqueous solution of $Ga(NO_3)_3$ ~ 1 M. MAS spectra (30 kHz) were recorded using one pulse sequence with the use of pulses of 2 μs; 1k-2k scans were acquired with a recycle delay 10 s.

All the spectra were processed using TopSpin™ 3.1 (Bruker). The spectra were best-fitted with both TopSpin™ 3.1 SOLA (Bruker) and QuadFit packages.[46] The latter one was employed in order to explore different types of models for the distribution of quadrupolar parameters. Namely, Gaussian and Czjzek distributions were investigated.

Both Gaussian and the Czjzek distribution models[47] consider a continuous distribution of the quadrupolar parameters for a single site but, while the former simply allows to consider a distribution of both asymmetry η_Q and C_Q parameters, the latter is a joint distribution of the V_{ii}, the diagonal elements of the *EFG* tensor, and the η_Q parameters. These approaches enable the accurate simulation of the asymmetric line-shapes typical of disordered polycrystalline materials. In the case of ^{27}Al NMR spectra, these

distributions accurately reproduced the high field "tail" feature of the spectra.[48] In the case of Czjzek distribution fitting, the spectra were simulated by keeping the Czjzek parameter $d = 5$.

DFT calculations - Simulations were performed in P_1 symmetry on 2x2x4 super-cells containing approximately 250 atoms. Due to the practical limitations of the super-cell dimensions, and in order to assure a good statistic treatment, six disordered distributions of the La and Sr cations on the available crystallographic sites were generated and analyzed, while maintaining the overall $LaSrAl_3O_7$ composition. All the distributions were obtained by means of a simple pseudo-random number generation routine.
A Gaussian-like behavior of the cations distribution was found for both sites: the majority (36%) of Al^1 sites are surrounded by 4 La and 4 Sr atoms, 36% of Al^2 sites are surrounded by 3 La and 3 Sr. The distributions of La/Sr cations around Al^1 and Al^2 sites of the six structural models are reported in Figure 3.3. The six structural models were optimized by means of density functional theory (DFT) calculations using the CASTEP code,[49] and the NMR parameters were obtained by using PAW[50] and GIPAW[51] formalisms. The generalized gradient approximation (GGA) PBE functional [52] was employed, and the core-valence interactions were described by ultra-soft pseudopotentials.

For ^{17}O, the *2s* and *2p* orbitals were considered as valence states with a core radius of 1.3 Å; for ^{27}Al, a core radius of 2.0 Å was used with *3s* and *3p* valence orbitals; for Sr, a core radius of 2.0 Å was used with *4s*, *4p* and *5s* valence states while for La, a core radius of 2.0 Å was used with *5s*, *5p*, *6s* and *5d* valence states and a core radius of 1.6 Å was used for the *4f* valence state.

All calculations were performed at the Γ point since several tests have shown that it provides converged results for systems having side boxes larger than 13 Å (as in this case, where the supercell has

side boxes between 15 and 16 Å).[33-35,53] Wave functions were expanded in plane waves with a kinetic energy cutoff of 600 eV, a value which has been already demonstrated to be suitable for total energy and NMR chemical shift convergence.[54]

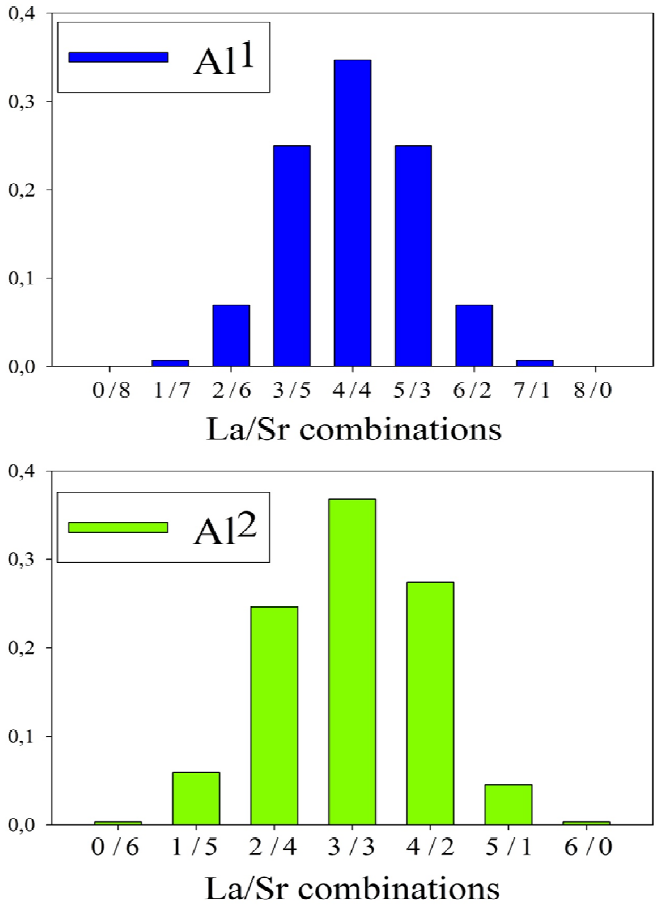

Figure 3.3 – Relative populations of La/Sr distributions around Al^1 and Al^2 sites in the six computational structural models considered.

It is well known that standard GGA/DFT is not recommended for elements with localized *d* or *f* empty states since it provides energy levels too stabilized; these generate excessive covalent interactions with anionic *p* states and, as consequence, incorrect electronic properties such as the DOS, band gaps, and NMR parameters of oxygen connected to these elements are generated. For example, recent investigations have shown that it is necessary to add an on-site Hubbard correction on the *3d* and *4f* orbitals of Sr and La to adjust their position relative to Sr (*4p*)[55] and La(*5d*) levels.[56] In this work this problem has been solved by artificially shifting the local potentials of Sr^{2+} ($4d^0$) and La^{3+} ($4f^0$) to higher energy compared to the default definition proposed by the Material Studio Package, as previously proposed by Profeta et al.[57] for the Ca^{2+} ion ($3d^0$), and by Sadoc et al.[58] for Sc^{3+} ($3d^0$) and La^{3+} ($4f^0$).

Following Profeta's procedure, the *3d* and *4f* energy levels of Sr^{2+} and La^{3+} have been empirically shifted by 2.49 and 20.4 eV, respectively. These are the values for which the chemical shifts of ^{17}O in SrO and La_2O_3 oxides match the experimental values previously (reported by Turner et al.).[59] The variation of the isotropic chemical shifts of ^{17}O with respect to the $3d^0$ and $4f^0$ energetic shift are reported in Figure 3.4a and 3.4b

The calculation of the density of states (DOS) of La_2O_3 using the PBE functional with the original and shifted PPs have been compared (Figure 3.5) with the one obtained by using the hybrid PBE0 functional,[60] which provides a better description of the covalency in these system as well as band gaps in good agreement with the experimental ones.[61]

In the PBE0 calculations norm-conserving pseudopotentials (NCPP) with a higher energy cut-off value (1000 eV) have been proposed and used because USPP are not yet supported with hybrid functionals.

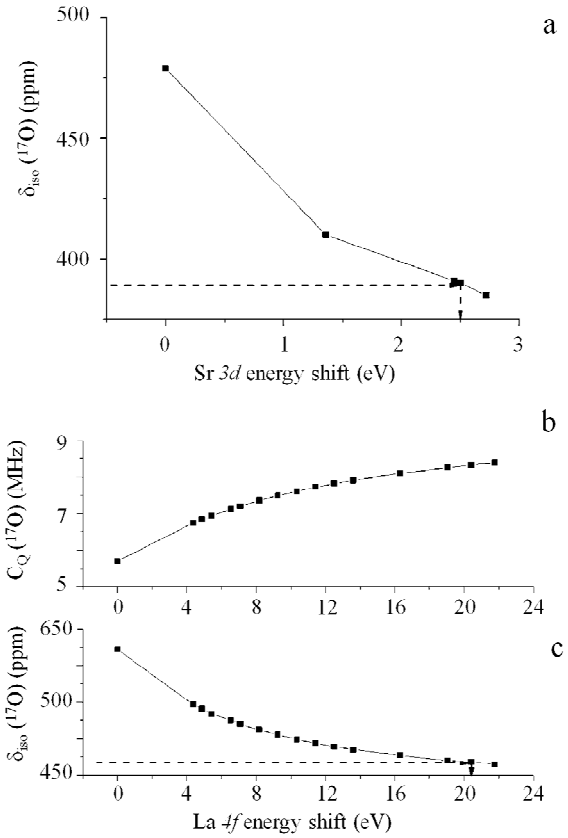

Figure 3.4 – a) The isotropic chemical shift of ^{17}O in SrO as a function of the applied energy shifts on the 3d orbitals of Sr. The dotted line shows that the experimental isotropic chemical shift is computed for a shift of 2.49 eV. b) the quadrupolar constantof ^{17}O and c) the isotropic chemical shift of ^{17}O constant of ^{17}O in site 1 of the crystalline La_2O_3 crystal as a function of the applied energy shifts on the 4f orbitals of La. The dotted line shows that the experimental isotropic chemical shift is best computed with an energy shift of 20.4 eV.

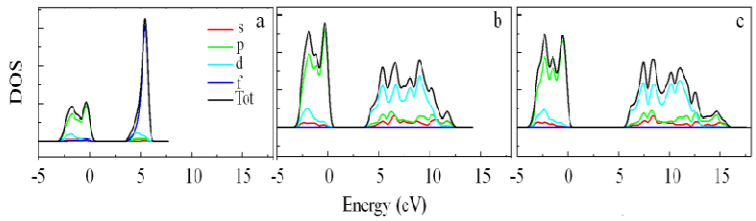

Figure 3.5 - The density of states (DOS) for La_2O_3 using the PBE functional (a), the PBE functional with a 4f-shift of 20.4 eV for La (b) and the PBE0 hybrid functional (c). The colored curves represent the partial density of states projected on the s, p, d and f orbitals. The experimental band gap is 5.7 eV.

4f energy shift	***δ_{iso} (ppm)***	***C_Q (MHz)***
0.0	9.3	0.11
20.4	10.0	0.12

Table 3.1 - Isotropic chemical shift and quadrupolar coupling constant of ^{27}Al in crystalline $LaAlO_3$ crystal as a function of the 4f energy shift. The value of the shift minimally affects the calculated aluminum NMR parameters.

As expected the PDOS computed with the shifted potential is in very good agreement with those obtained by using the PBE0 functional. The effect of the shift applied on the *4f* orbitals is clearly observed in the conduction band; the shape of the La_2O_3 conduction band having mostly a La *4f* character for the not-shifted potentials becomes closer to the one obtained using the hybrid functional, where *4f* orbitals do not contribute at all. The band gap of La_2O_3 is mainly imposed by the position of La (*5d*) states in the conduction band and is respectively calculated to 3.77

eV using the PBE functional with shifted potentials. As expected, the use of the hybrid functional gives a higher band gap value of 5.7 eV which is exactly equal to the experimental one.[62]
However, it is worth noting that although the energy shift heavily affects the ^{17}O isotropic shift further tests on the $LaAlO_3$ crystal structure reported in Table 4.1 have shown that they do not affect the chemical shift and electric field gradients of Al ions.

Outputs of DFT-GIPAW calculations were processed by the fpNMR package.[63,64] This code allows the simulation of NMR spectra (MAS, MQMAS) under various experimental conditions, and the statistical analysis of the NMR parameters. Isotropic chemical shifts (δ_{iso}^{calc}) were evaluated from the calculated isotropic magnetic shielding, σ_{iso}^{calc}, using the formula $\delta_{iso}^{calc} = -(\sigma_{iso} - \sigma_{ref})$. For ^{27}Al nucleus, σ_{ref} = 555.19 ppm was determined using Corundum as the reference crystalline solid phase.[34,54] Quadrupolar coupling constants, C_Q, of ^{27}Al were calculated with a scaled quadrupole moment (Q) of 140.4 mB. This value was obtained by multiplying the accepted "experimental value" of 146.6 mB[65] by a scaling factor calculated via linear fitting of the plot of experimental and theoretical ^{27}Al C_Q values in crystalline Anorthite ($CaAl_2Si_2O_8$), as described in ref. 66.

3.3 – $LaSrAl_3O_7$: Results and discussion

3.3.1 –Diffraction analysis

Figure 3.6 presents the X-rays powder diffraction pattern of $LaSrAl_3O_7$ refined by means of the Rietveld method. The pattern can be indexed in the tetragonal *P*-42$_1$*m* (no. 113) space group. It is possible to observe a spurious reflection at 34°. Other less intense extra-peaks are observed at 23.5° and 48°, which can be associated with the $LaAlO_3$ phase. A two-phase refinement was therefore

applied with the aim to quantify the impurity phase, which was shown to be approximately 3%. The results of this refinement are reported in Table 3.2

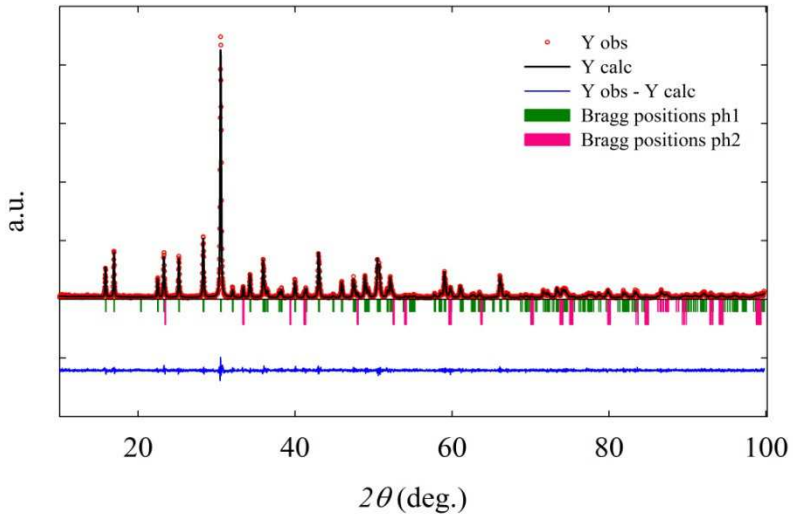

Figure 3.6 - Rietveld-refined X ray powder diffraction data for $LaSrAl_3O_7$ showing the observed (red), calculated (black), difference (blue) profiles and Bragg positions for the two phases, $LaSrAl_3O_7$ (green) and $(La/Sr)AlO_3$ (pink).

The average structure of $LaSrAl_3O_7$ (Figure 3.7a) is described by a tetragonal symmetry already outlined at the beginning of the chapter. In this structure, two distinct crystallographic sites for Al are present (named Al^1 and Al^2) and three different O positions are available (named O^1, O^2 and O^3 in the following), while La and Sr are distributed over the same crystallographic site.
The structure is composed of AlO_4 tetrahedra. Each Al^1O_4 tetrahedron is linked to other four Al^2O_4 units by four bridging oxygens (BO), whereas Al^2O_4 tetrahedra are linked to other three

AlO_4 polyhedra (two Al^1O_4 and one Al^2O_4 units), leading to an overall multiplicity of the Al sites of 1 Al^1 : 2 Al^2.

Atom	*x*	*y*	*z*
Al1	0.0	0.0	0.0
Al2	0.8582 (6)	0.6418 (6)	0.036 (2)
La/Sr	0.6621 (2)	0.8379 (2)	0.4911 (6)
O1	0.5	0.0	0.830 (4)
O2	0.863 (1)	0.637 (1)	0.704 (2)
O3	0.913 (1)	0.835 (1)	0.189 (2)

Table 3.2 – Refined crystallographic parameters for $LaSrAl_3O_7$, space group $P\text{-}42_1m$, a = 7.8966 (1) Å, c = 5.23145 (9) Å, B_{iso} = 0.348, R_{exp} = 15.23, R_{wp} 16.1, R_p 11.5.

A relevant feature of the Al^2O_4 unit is the presence of a non-bridging oxygen (NBO) along the *c* direction. The tetrahedral network extends in the *ab* plane; along the *c* axis these layers are spaced by La/Sr cationic slabs, where a single crystallographic position, *M*, is available for both La and Sr. Figure 3.7b illustrates in greater detail that the Al^2O_4 tetrahedra are surrounded by six La/Sr positions in the first cationic coordination sphere, whereas the Al^1O_4 tetrahedra are surrounded by eight La/Sr positions. The average structure derived from the diffraction data treats the *M* site with mixed occupancy, *i.e.* the single site is occupied by the two different cations La^{3+} and Sr^{2+} with the same occupancy probability (0.5) and an associated formal charge +2.5. This implies that all the Al^1O_4 units are characterized by only one value for all the Al^1-O^3 distances. Al^2O_4 tetrahedra, in contrast, present three

distinct bonds with oxygens in different crystallographic positions (Figure 3.7b).

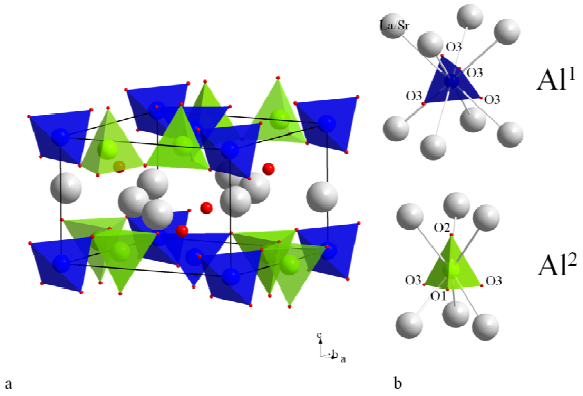

Figure 3.7 – a) $LaSrAl_3O_7$ crystal structure. (Al^1 green, Al^2 blue, O red, La/Sr pink); b) representation of the first cationic coordination sphere for the two aluminum sites. Al^1O_4 neighbors eight cation sites and Al^2O_4 neighbors six cation sites and different coordination with O^1, O^2 and O^3 species.

3.3.2 – NMR study

Referring to the above description of the average structure, on the local scale, however, La and Sr may be non-randomly distributed, and their reciprocal arrangements may induce local distortions and deviations from the ideal average structure; this will be reflected in the local environment of the individual Al sites, as already found for the $LaSrAlO_4$ system presented and discussed in the previous Chapter. ^{27}Al solid-state NMR is one of the techniques of choice to investigate this aspect. Both the lineshape of the NMR spectrum and the apparent chemical shift are related to *EFG* at the nuclear site, which in turn is related to

the degree of spherical symmetry about the nucleus.[67] Furthermore, the existence of structural disorder results in additional broadening due to distribution of the quadrupolar parameters, and the coupling constant, C_Q, and the asymmetry parameter, η_Q. Since the ^{27}Al C_Q values are generally on the order of a few MHz, both 1D and 2D NMR spectra can be obtained at high magnetic fields due to the favorable scaling of the quadrupolar interaction. It is usually possible to establish good correlations between the isotropic chemical shift and the Al coordination number in the structure. In particular, in the case of the aluminum oxides, the atomic coordination IV, V and VI are well-resolved and related to different chemical shift ranges, i.e. 50 to 80 ppm, 30 to 40 ppm and -10 to 15 ppm, respectively.[67]

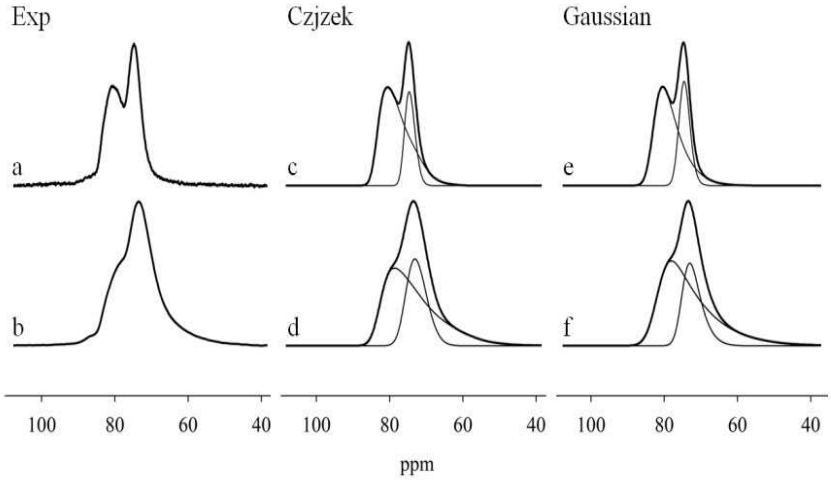

Figure 3.8 – 1D MAS ^{27}Al spectra: experimental spectrum at 23.5 T (a) and at 16.4 T (b); 23.5 T data fitted in terms of the Czjzek distribution (c) and 16.4T data fitted in terms of the Czjzek distribution (d); 23.5 T data fitted in terms of the gaussian distribution (e) and 16.4 T data fitted in terms of the gaussian distribution (f).

Figure 3.8 shows the 1D ^{27}Al MAS spectra of the sample $LaSrAl_3O_7$ acquired at room temperature at 23.5 T (a) and 16.4 T (b), with a standard spin-echo sequence. The first information that can be extracted from the spectra is the presence of two distinct Al sites in the structure. This is particularly clear in the 23.5 T spectrum. The observed chemical shift range (60-80 ppm) confirms the tetrahedral coordination of both sites.

Although the two crystallographic sites are quite similar, which is reflected by the partial overlapping of the two NMR peaks, a striking difference between them is related to the presence of a NBO in Al^2. The spectra do not show the features characteristic of 2nd order quadrupolar broadening, rather they exhibit an asymmetric shape with a steep edge at low field (more evident in the 23.5 T spectrum) with a tail at high field. This last feature is generally associated with disorder and the presence of a distribution of the quadrupolar parameters, C_Q and η_Q.[68]

As stated, the experimental spectra were fitted using different models for the distribution of the quadrupolar parameters, in order to identify the better procedure for the analysis of the whole series. Particularly, Czjzek and Gaussian distribution were evaluated. The results are reported in Figure3.8 and Table 3.3. The Czjzek model was initially developed for the simulation of quadrupolar spectra of disordered systems, like glasses and amorphous materials, as this model is based on the assumption of statistical invariance by rotation of the considered system, and thus on the validity of the application of the central limit theorem for the *EFG* tensor.[47] At the same time, the robustness of the model was demonstrated using it for the evaluation and simulation of the local disorder in crystal solids like Al_2O_3.[69] The considered $LaSrAl_3O_7$ sample is highly crystalline, as demonstrated by the X ray powder diffraction analysis. At the same time, at a local scale, the distribution of La and Sr on the same crystallographic position

does introduce a source of disorder around the Al site. This can give the rationale for the application of Czjzek model for addressing the local disorder in the crystal.

B_0	Site	C_Q range (MHz)	σ (MHz)	Area (%)	δ_{iso} (ppm)	Ag. Fac. (%)
			Czjzek model			
23.5 T	Al^1	-	0.6	26.0	75.6	97.7
	Al^2	-	0.9	74.0	84.2	
16.4 T	Al^1	-	0.6	33.5	76.0	96.7
	Al^2	-	0.7	66.5	83.8	
			Gaussian model			
23.5 T	Al^1	2.0 - 5.5	-	31.7	75.4	96.9
	Al^2	2.2 - 11.5	-	68.3	82.3	
16.4 T	Al^1	2.0 – 6.0	-	29.5		97.7
	Al^2	2.3 – 12.0	-	70.5		
			DFT			
	Al^1	5.0*	-	33.3	75.6	-
	Al^2	7.1*	-	66.7	81.8	

*Table 3.3 – NMR parameters obtained by the best-fit of the spectra of Figure 3.8. * = average of the values reported in Figure 3.8.*

The results, reported in Table 3.3, showed a good agreement between the values obtained at the two magnetic fields. The parameter σ, which is the only parameter optimized in the Czjzek distribution,[69] controls the width of the distribution of the *EFG* elements and the width of the distribution of the asymmetry parameter η_Q. The extraction of the mean values and the distribution widths of the quadrupolar parameters are not trivial. We performed some sensitivity tests on the C_Q maximum value (the minimum one being kept at 0.1 MHz), and found that its effect becomes negligible when the higher values given by DFT calculations (see below) are reached.

The Gaussian model provides a more simple approach, as for this fitting procedure it is possible to obtain directly the mean C_Q and η_Q values with the amplitude and the center of the parameters distribution and at the same time is based on correct assumption and hypothesis. The fitted spectra are presented in Figure 3.8, panel e and f and the corresponding results are reported in Table 3.3.

The comparison between the results obtained for the two models indicates that both of them can give good results in the fitting of the two peaks and in evaluating the characteristic line shape. In particular, both of them can accurately describe the tail at high field. In this particular case, therefore, Gaussian model seems to be more useful in the view of finding a correlation between NMR and structural quantities. The local disorder given by a non-random cation distribution is likely not enough to require a more sophisticated treatment such as the one given by Czjzek model.

At the same time, in order to obtain more detailed information on the distribution of the quadrupolar parameters and to find the correlation with the local structure features, as well as to assign the two NMR peaks to the two non-equivalent crystallographic sites, the combination of more sophisticated 2D NMR experiments (MQMAS) and DFT calculations is mandatory.

3.3.3 – DFT calculations

Figure 3.9 reports the δ_{iso} vs. C_Q correlations obtained from DFT calculations for the two Al sites with all the possible combinations of the Sr and La cations. Al^1 and Al^2 yield well-separated (δ_{iso}, C_Q) distributions and thus they should be easily distinguished in the MQMAS spectra.
It is noteworthy that Al^1 distribution is much more isotropic than Al^2, irrespective of the stochastic distribution of cations around both the Al tetrahedra. This calls for a relevant role of the NBO in determining the (δ_{iso}, C_Q) correlation (see below).

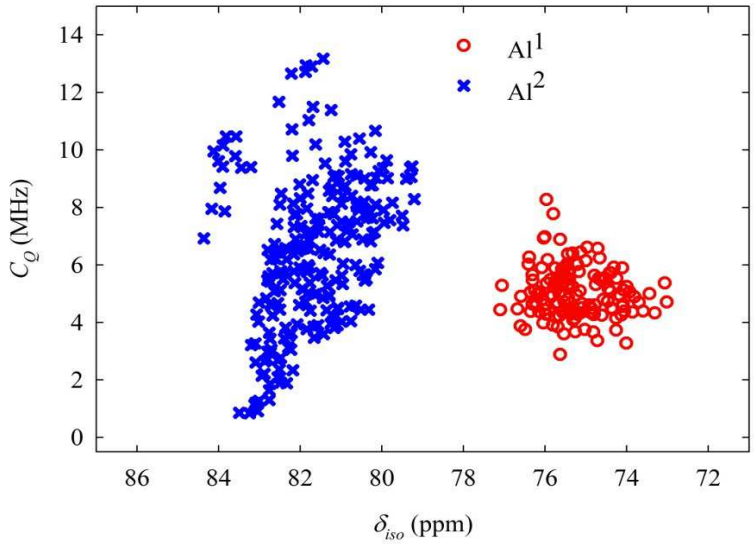

Figure 3.9 - Theoretical (δ_{iso}, C_Q) distributions for the Al^1 and Al^2 sites in the six computational structural models investigated.

In agreement with the simulations of the 1D MAS ^{27}Al solid-state NMR spectra and the DFT calculations, the MQMAS ^{27}Al NMR spectrum reported in Figure 3.10 clearly shows two sites. Isotropic

chemical shifts of 76.5 ppm and 84 ppm were obtained from simulations of the direct dimension slices with maximum intensities. However, the two sites are characterized by very different quadrupolar broadening.

From the MQMAS spectra, assignment of the two peaks to the two Al sites is straightforward: the peak at lower chemical shift is characterized by a relatively narrow C_Q distribution, in the range ~3 to ~5 MHz, whereas the one at higher chemical shifts is characterized by a broader C_Q range (~4-8 MHz).

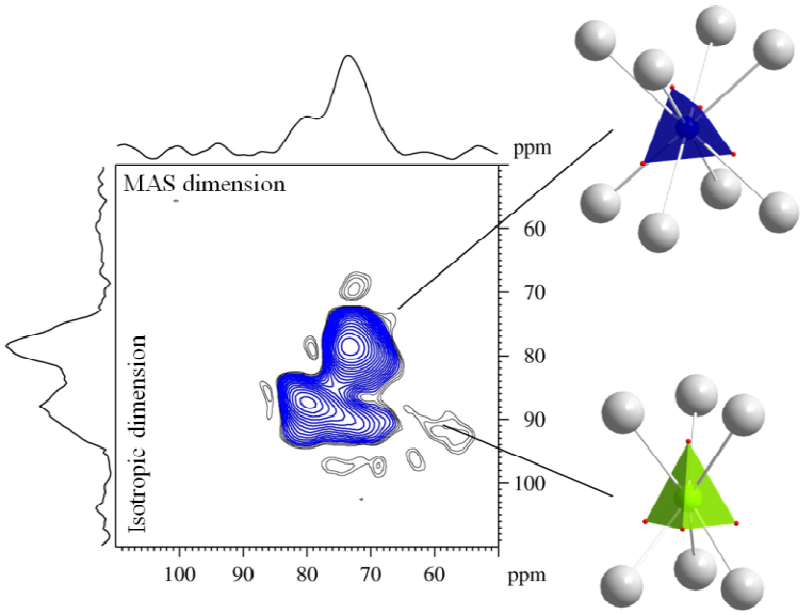

Figure 3.10 - Experimental 3Q MAS spectrum recorded at 700MHz field. The 2D spectra clearly indicates the presence of two distinct sites with significantly different C_Q.

Therefore, we can conclude that the broader peak at lower field is due to the Al^2, whereas the sharper peak at higher field is the signal of the Al^1 site.

While the MQMAS experiment allowed a clear separation of the two sites, it must be stressed that an accurate determination of the distribution of the quadrupolar parameters, as well as of the relative peak intensities (which are related to the sites multiplicity) must be obtained from simulations of the 1D MAS spectrum (Figure 3.8), because the MQMAS spectrum is less accurate in describing sites affected by large C_Q values and it requires specific treatments.[70]
Having assigned the NMR features to the two distinct Al crystallographic sites, the next step is to correlate the local, and possibly the medium-range structure, of the sites (*i.e.* deviations from tetrahedral symmetry, non-bridging oxygens, next-neighbours nature, etc.) with the observed quadrupolar parameters and their distributions. In the case of ^{27}Al NMR, several parameters were previously proposed to quantify the local order, including bond lengths- and bond angles-based tetrahedral distortions parameters.[67] However, because of the lack, in the case of ^{27}Al NMR, of clear-cut relationships among direct geometric features and NMR observables, first-principles quantum mechanical calculations are mandatory to model the system at the local level.

As stated before, both sites are in tetrahedral coordination and face cationic La/Sr planes. The cationic coordination sphere is constituted by La/Sr positions at an average distance of ~4 Å for all the AlO_4 units. All the tetrahedral units are linked to each other by forming a plane through bridging oxygen ions, and the two sites are expected to have similar NMR isotropic chemical shift and quadrupolar asymmetry because of similar first coordination spheres and coordination geometries. Despite the similarities of

the two Al sites, however, significant differences in C_Q are expected for the following reasons:

i) the crystallographic position of coordinating oxygens. In fact, Al^1 is surrounded only by oxygens in O^3 position, whereas Al^2 is coordinated by two oxygens in position O^3, one in position O^1 and one in position O^2;

ii) the presence of non-bridging oxygens. Being coordinated only to O^3 positions, Al^1 is always surrounded by oxygen co-shared with other tetrahedral units. In contrast, Al^2 is bound to a non-bridging oxygen in O^2 position aligned with the *c* axis;

iii) the number and nature of ions in the first cationic coordination sphere. Al^1O_4 tetrahedra are surrounded by 8 La/Sr positions, while Al^2O_4 units are coordinated to 6 La/Sr sites. Since C_Q is related to the *EFG* at the nucleus position, it is very sensitive to local structural distortions and, as outlined above, this explains why two distinct ranges of C_Q are experimentally observed for the two distinct Al sites.

The distortion, Δ_{tetra}, of the tetrahedral Al sites was calculated according to the following expression for each of the GIPAW DFT calculated structures with different La/Sr substitution patterns

$$\Delta_{tetra} = \frac{1}{4}\sum_{i=1}^{4}\left(\frac{l_i - l_m}{l_m}\right)^2 \qquad (3.1)$$

where l_i is the single Al-O distance within the tetrahedron, and l_m is the average Al-O distance within the same tetrahedron.[71]

Figure 3.11 shows the calculated structural distortions plotted against the calculated C_Q for each Al site. The upper panel reports the data related to the Al^1 sites, whereas the lower panel refers to the Al^2 ones.

The first clear information that can be extracted from the visual inspection of these plots is that the Al^1O_4 tetrahedra are characterized by a smaller distribution of distortions (0.00-0.02 range) and by a relatively small distribution of calculated C_Q values (3-8 MHz range). Conversely, for Al^2O_4 tetrahedra, the calculated tetrahedral distortions range approximately from 0.0 to 0.055 and the calculated C_Q from 1 to 13 MHz.

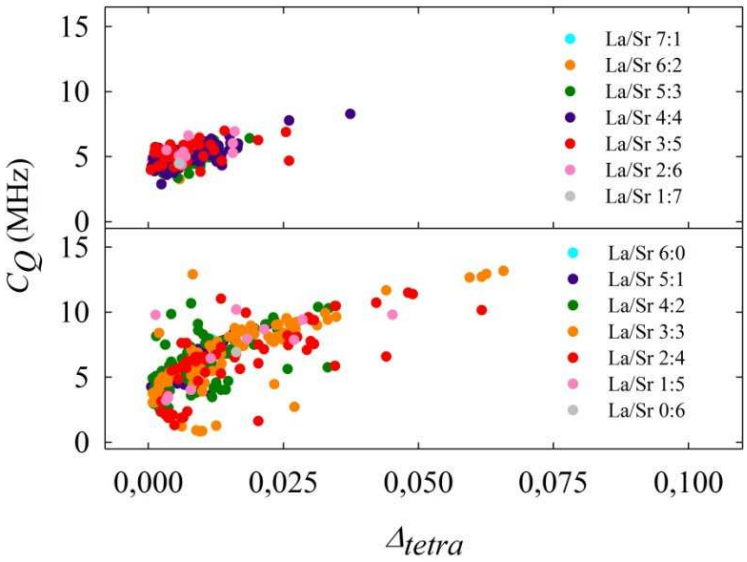

Figure 3.11 – Theoretical C_Q values vs. tetrahedral distortion parameter, Δ_{tetra} for Al^1 (top panel) and Al2 sites (bottom panel).

A linear trend can be observed between the tetrahedron distortion and the corresponding C_Q value, with larger distortions leading to larger values of C_Q. We also tried to correlate the Δ_{tetra} parameter with the nature of the surrounding cations in the first cationic coordination shell. To clarify this correlation, different colors were associated to different La/Sr ratios in Figure 3.11 (see labels).

La/Sr distribution	*Population*	δ_{iso} *(ppm)*	C_Q *(MHz)*	η_Q
		Al^I		
1La-7Sr	0.01	76.7	4.46	0.33
2La-6Sr	0.07	76.1	5.53	0.28
3La-5Sr	0.24	75.6	5.21	0.41
4La-4Sr	0.36	75.2	5.17	0.42
5La-3Sr	0.24	75.0	4.68	0.47
6La-2Sr	0.07	74.1	4.33	0.50
7La-1Sr	0.01	74.8	4.27	0.45
		Al^{II}		
6Sr	0.01	84.5	7.23	0.11
1La-5Sr	0.05	83.2	7.11	0.27
2La-4Sr	0.26	82.1	6.15	0.41
3La-3Sr	0.36	81.5	6.73	0.36
4La-2Sr	0.26	81.2	6.37	0.37
5La-1Sr	0.06	81.2	6.41	0.27
6La	0.00	-	-	

Table 3.4 - Theoretical NMR parameters and population of La/Sr distributions around Al^1 and Al^2 found over the considered six simulation boxes.

Unfortunately, it was not possible to find a clear-cut correlation between the degree of distortion and the La/Sr ratio in the first cationic coordination shell. For example, in the case of Al^2 site, the distortions of the La/Sr 3:3 combination are well distributed in the range 0 - 0.055, with the corresponding C_Q values spanning from ~1 to more than 12 MHz. A more detailed information is reported in Table 3.4.

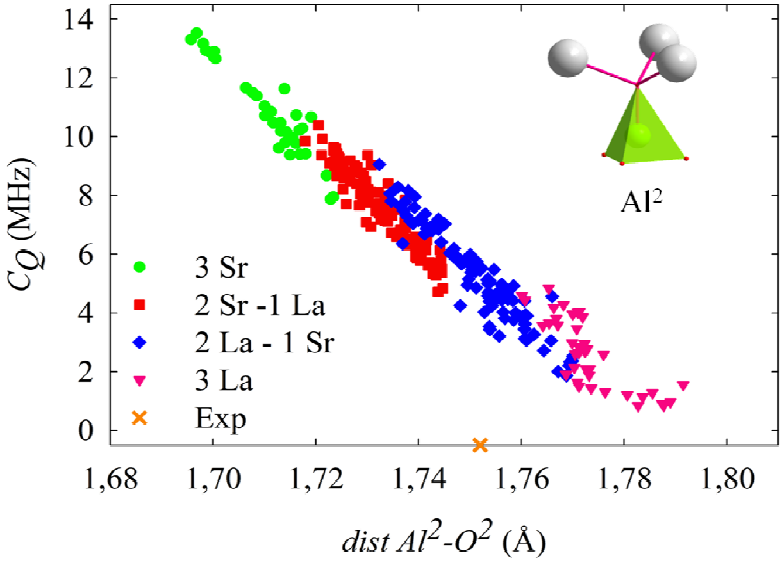

Figure 3.12 – Theoretical C_Q values vs. Al^2-O^2 distance. The different colors are related to different cationic coordination for the non-bridging oxygen O^2. Green: three Sr ions, Red: two Sr and one La ions, Blue: two La and one Sr ions, Pink: three La ions. The orange cross on the horizontal axis indicates the experimental Al^2-O^2 distance obtained from Rietveld refinement of diffraction data.

In contrast, a clear relationship emerges if one considers the position of the La/Sr atoms with respect to NBOs. Figure 3.12

shows the correlation plot between the C_Q values calculated for the Al^2O_4 tetrahedra and the Al^2-O^2 distance, *i.e.* the bond length involving the NBO.

The plot shows a clear linear correlation between these two parameters. In particular, the most distorted tetrahedra (*i.e.* the ones with the largest C_Q) are those characterized by the smallest Al^2-O^2 bond lengths. As already stated, each NBO is near to three La/Sr cations in apical positions above it (see Figures 3.7 and 3.12). When the various combinations of cations are marked with different colors, we observe well-defined islands in the correlation chart of Figure 3.12. In particular, the shortest Al^2-O^2 bond lengths, which correspond to the largest tetrahedron distortions (and C_Q values), are found when three Sr cations occupy the positions above the NBO. In contrast, the longest bond lengths are observed when only La cations are present. Intermediate bond lengths were found in case of mixed cations distributions. This result confirms that La^{3+} attracts the O in the apical non-bridging position more than Sr^{2+} due to the charge effects, as previously suggested for the $LaSrAlO_4$ system.[41] From Figure 3.12 it is also clear that the large C_Q spread observed for Al^2 sites is mainly due to the cation speciation in the NBO apical position.

The presence of NBOs is, therefore, an important feature to introduce possible elements of disorder in an anisotropic, particularly layered structures, where different cations can be differently arranged around them. In the case of stochastic cation distributions, like in the present case, this could lead to interesting applications, for example in thermoelectric materials where one of the optimization strategies is the decoupling of the phonons spectrum from the electronic spectrum.[72] In other cases, it could be possible to force a non-random cations distribution and particular cations ordering, so giving rise to a "two-phases" material, at least from the NMR point of view.

3.4 – LaSr(Ga/Al)$_3$O$_7$ SERIES: RESULTS AND DISCUSSION

3.4.1 –Diffraction analysis

Figure 3.13 presents the neutron diffraction patterns for all the samples of the series $LaSrGa_{3-x}Al_xO_7$ with x = 0, 1, 1.5, 2, 3. The diffraction patterns reveal the presence of a single phase for all the samples; all the pattern can be indexed with the use of space group n.113 and no evident distortions or deviations from the tetragonal symmetry are present, as already evidenced for the Al3 sample analyzed in the first part of this Chapter. The samples are generally single phases; only for composition Ga1Al2 and Al3 a small amount of impurity was found. From a first inspection of the patterns it is possible to observe a clear trend of both peaks positions and intensities with composition as reported in the lower panel of Figure 3.13. The sol-gel procedure has lead to the formation of the complete solid solution between the two end members Ga3 (pure Ga) and Al3 (pure Al). The synthesis of the compounds were carried out without the necessity of an empirical extra amount of Ga, as reported in literature for solid-state reaction.[10,73] Particularly, the pure-Ga sample can be synthesized according to this sol-gel procedure starting from stoichiometric amount of Ga. In fact, the solid state route was the only synthetic strategy considered for the preparation of $LaSrGa_3O_7$ and related compounds but the use of extra-amounts of initial Ga_2O_3 reagent were needed in order to compensate the gallium volatilization during the prolonged high-temperature treatments, required to complete the reaction.[12] These initial extra quantities of Ga were found empirically and they were found to depend on the overall composition of the samples and to the duration of the treatment above 1400°C. The sol gel approach allowed us to reduce the length of the final step at high temperature and, at the same time, to prepare up to 4 g of sample in a single synthesis batch.

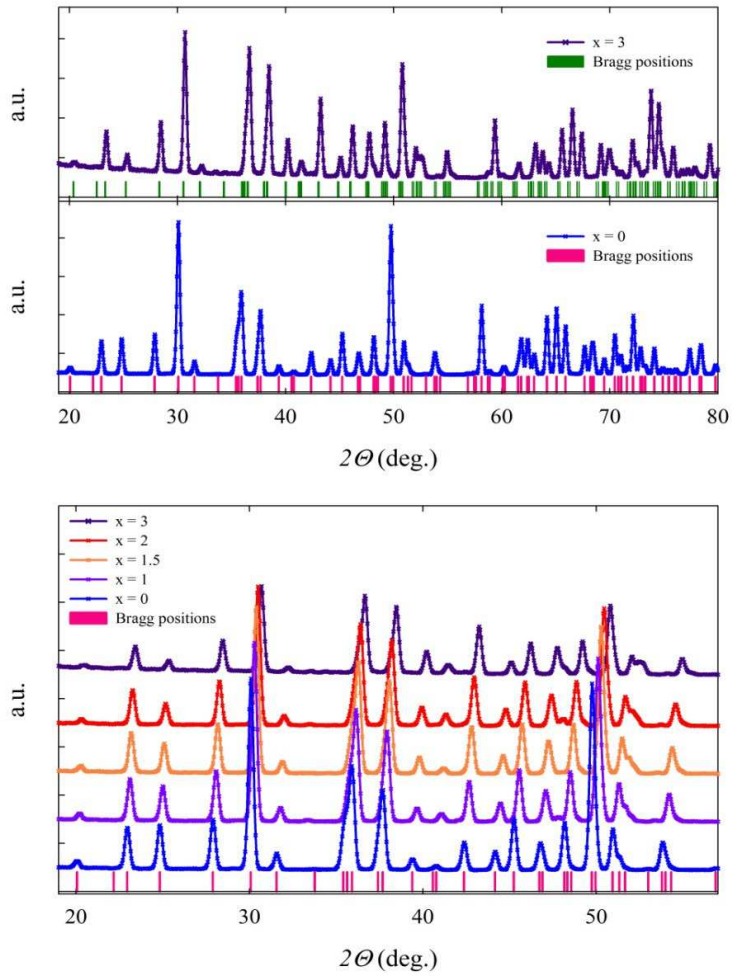

Figure 3.13 – Room temperature powder diffraction pattern for all the sample of the series $LaSrGa_{3-x}Al_xO_7$ x = 0, 1, 1.5, 2, 3. Zoom in the range 20-60° (right panel) highlights the trend in peaks positions and intensities with composition. Bragg positions refer to the x = 0 composition.

Change in symmetry and deviations from the purely tetragonal structure have been observed observed when the La/Sr ratio is modified. Lanthanum and strontium, as described above, occupies the same site, *M*, with mixed occupancy (see Figures 3.1 and 3.7). The deviation of the La/Sr ratio from 1:1 implies the formation of defects in the structure in order to compensate the change in the average charge of the *M* site; also the change in the average dimension of the *M* site can lead to the creation of distortions. The change in the average size and charge of the *M* site, together with the presence of the introduced defects, can actually lead to changes in the symmetry. Particularly, for the case of La/Sr >1 ($La_{1.6}Sr_{0.4}Ga_3O_7$ composition) a phase transition from the tetrahedral structure to a pseudo-orthorhombic cell was observed with the splitting of the h, k ≠ l tetragonal reflections.[73] For the $LaSr(Ga/Al)_3O_7$ series this splitting is not revealed for any sample. The variation of the Ga/Al does not affect the average charge of the tetrahedral *T* sites, but it implies only a variation in the average ionic radius of the *T* sites, helping in maintaining the same cell symmetry.

In order to obtained detailed structural information, Rietveld refinements were performed. For the sample Ga1Al2 and Al3 extra peaks at ~ 33°, 41°, 71° and 85° were found; it was possible to identify this second phase as $(La,Sr)AlO_3$; the perovskite structure was already found to be present as secondary phase in the synthesis of $LaSrGa_3O_7$ system.[10,73,74] A small shoulder at 42.2° is visible for the samples Ga2Al1 and Al3 and can be associated with the [110] reflection of the vanadium sample holder; as it is very weak it was neglected in the refinements. To improve the structural analysis, two-phases refinements were performed for these compositions and they leaded to estimate the amount of the second phase as approximately 2%. The presence of this small amount will be neglected in the further discussion.

The analysis for sample Ga3 and Al3 led to the characterization of the average structure, presented in Figure 3.7. The detailed description of the structure was reported previously for the pure aluminum samples and it is also representative for the pure gallium sample.

The analysis of the data for intermediate compositions x = 1, 1.5, 2 is not trivial as the structure presents two distinct crystallographic sites for Ga and Al, *2a* and *4e*, with multiplicity ratio 1:2 and thus more than one possibility for the ordering of the two ions on the two sites are available.

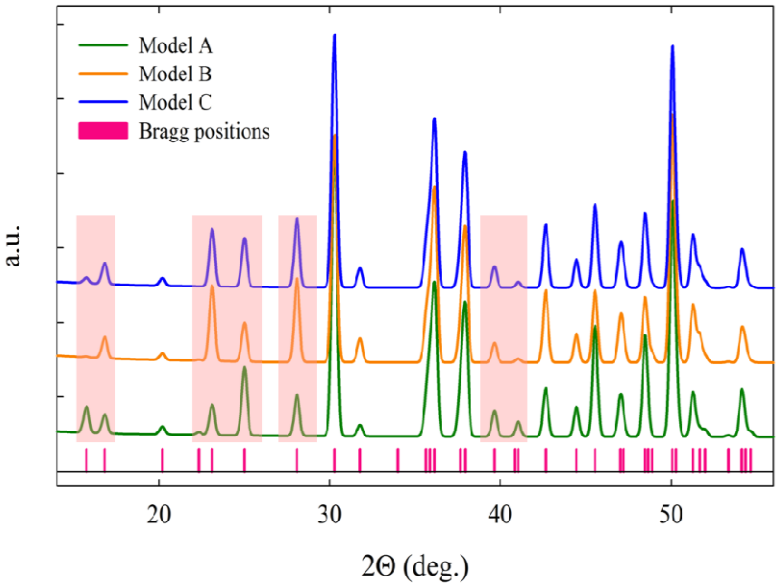

Figure 3.14 – Simulated diffraction patterns based on model A, B and C for the Ga2Al1 composition. Pink rectangles evidence the reflections interested by biggest change in intensities.

The two sites are very similar as they are both tetrahedral with co-shared oxygen ions and thus a perfect ordering with a strong preference of one cation for one site is difficult to obtain. At the same time, melilite structure is known for the constraints in the connectivity of tetrahedral sites and restrictions in the 2D network linkage. Systems such as $Ca_2CoSi_2O_7$ and $Sr_2CoSi_2O_7$ present large magnetoresistance properties and a strong coupling between magnetism and dielectricity; the presence of these properties has been directly connected to the particular network of tetrahedra in the melilite structure and to the ordering of Co and Si on the two sites.[7] Similar restrictions were also found in $A_2Al_2SiO_7$ system for which the "Loewenstein rule", predicting that (AlO_3)-O-(AlO_3) linkages are forbidden, is valid.[27,75] Based on these considerations, all the possible configuration arrangements of the two ions were evaluated. Four distinct models are possible. For example, for the sample Ga2Al1 the different models taken into account are:

- *Model A*. Ga on site 4e with occupancy equals to 1, Al on site 2a with occupancy equals to 1
- *Model B*. Ga on site 4e and 2a with occupancy 0.5, Al on site 4e with occupancy 0.5
- *Model C*. Ga and Al occupy both sites randomly. Occupancy of Ga for both sites is 0.67, for Al is 0.33
- *Model D*. Starting from model C, occupancy are refined.

The same models were transferred also to the compositions Ga1.5Al1.5 and Ga1Al2 while maintaining the nominal Ga/Al stoichiometric ratio. Models A and C represent the extreme cases. Model A is the most ordered as it considers a net preference of Ga and Al for a specific site, while C considers the totally random distributions. From the refinements of data using different structural models it is possible to identify the actual average arrangement of atoms in the sample.

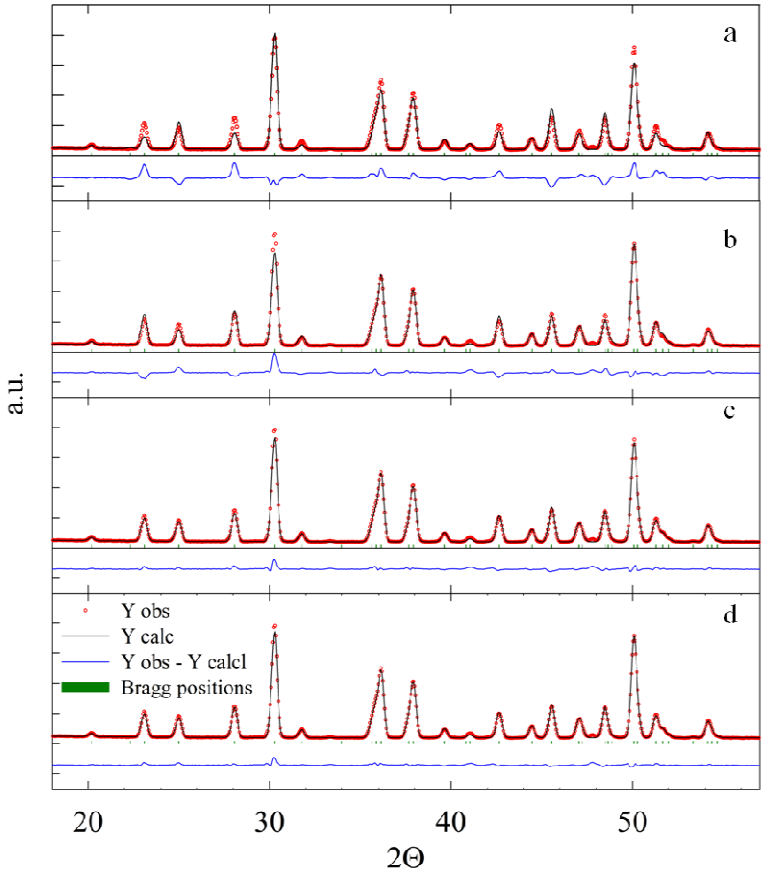

Figure 3.15 – Refinement of powder pattern of $LaSrGa_2Al_1O_7$ according to the Model A (a), Model B (b), Model C (c) and Model D (d). Agreement factor for different models: Model A R_{wp} 10.8 , R_p 8.02, X^2 79.8; Model B R_{wp} 6.528 , R_p 5.14 , X^2 31.7; Model C R_{wp} 4.76 , R_p 3.49 , X^2 16.9; Model D R_{wp} 3.24 , R_p 2.52 , X^2 8.45.

Peaks intensity is strongly dependent on the atomic species present in the lattice plane that generate the reflections. As Ga and Al have significantly different neutron cross-sections (^{69}Ga 7.88 fm, ^{71}Ga 6.40 fm, ^{27}Al 3.45 fm), the different models are expected to originate different diffraction patterns. Simulations of the diffraction patterns for composition x =1 based on different models are reported in Figure 3.14.

The main peak at ~ 30° does not show significant changes in intensity while the intensity of peaks at 15.6°, 16.7°, 23.1°, 28.2° and 41°, highlighted in pink in Figure 3.14, is predicted to be significantly affected by different arrangements of the Ga/Al cations on the two available sites. Similar results were obtained for the samples Ga1.5Al1.5 and Ga1Al2.

The Rietveld refined patterns for Ga1Al2 according to the four different models are presented in Figure 3.15. From the analysis of these data it is possible to choose the best structural model. Ordered models (A and B) lead to big discrepancies between calculated and experimental intensities while random models (C and D) correctly fit the intensities of the whole pattern. Very similar results have been obtained for the samples Ga1.5Al1.5 and Ga1Al2. This implies that for the whole solid solution no selective preference of Ga and Al for one site was found. Model D differs from model C for the refinement of the occupancies of the *2a* and *4e* sites. The refinements lead to a small difference with respect to the purely random arrangement of model C. For all the samples a preference of Ga for site *2a* and a consequent preference of Al for site *4e* were evidenced; the difference with respect to the random distribution is however within the 5% and therefore considered not significant.

Average structural data (cell parameters, inter atomic distances, anisotropic thermal factors) obtained from the Rietveld refinements were analyzed as function of composition. Results are

graphically reported in Figure 3.16 and 3.17. The data for the two end members are in good agreement with literature data.[9,14,73]

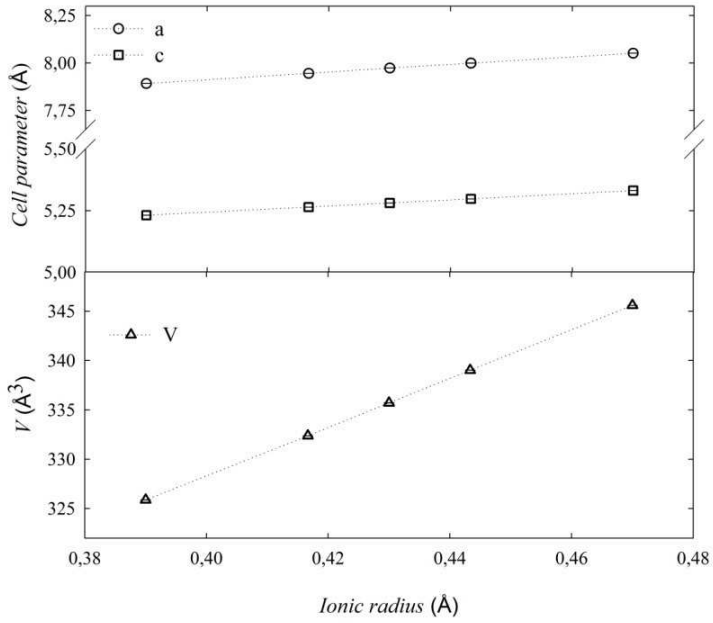

Figure 3.16 - Cell parameter (upper panel) and volume (lower panel) of the whole series of the sample as a function of the calculated average ionic radius of the tetrahedral sites obtained from Rietveld refinements. Error bars for experimental values are within the dimension of the symbols.

A clear trend of the cell parameters (*a*, *c* and *V*) was found with composition. The cell parameters clearly increase when the Ga ($r_{GaIII(IV)}$ = 0.47 nm) content increases with respect to the Al ($r_{AlIII(IV)}$ = 0.39 nm) one. The overall variation is ~ 2% for *a* and *c* and 5% for the volume. This effect is purely due to the dimension of the two

ions as they have the same charge and changes in oxidation state are not possible. The trend in cell parameters reflects the trend in interatomic distances T-O that shows a linear correlation with the composition as reported in Figure 3.17.

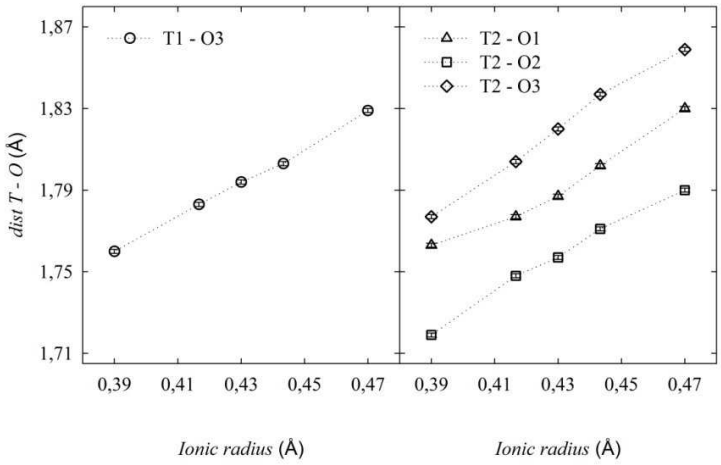

Figure 3.17 - Inter atomic T-O distances obtained from Rietveld refinements as function of the calculated average ionic radius of the tetrahedral sites. Error bars for experimental values are within the dimension of the symbols.

3.4.2 – NMR study

From the analysis of the average structure the complexity of these materials is highlighted; particularly this analysis evidences the presence of two independent sources of disorder (*i.e.* La/Sr and Ga/Al mixed site occupancy) that might create severe discrepancies between the average and the local structure. In order to investigate the repercussions of the disorder on a local scale, solid-state NMR is mandatory.

Figure 3.18a presents the 1D ^{27}Al solid-state NMR spectra for all the samples of the series; the chemical shift range (85-70 ppm) confirms the tetrahedral coordination of the aluminum sites. For the pure Al sample two distinct peaks are observed even if not completely resolved and characterized by different broadening; with the increasing of Ga content the contribution at highest field is significantly de-shielded, while the peak at lower field seems to be less affected by the variation in the composition of the samples. The attribution of the NMR signals has been already performed for the $LaSrAl_3O_7$ system in the previous part of this Chapter together with an extensive investigation on the correlation between quadrupolar parameters and local structural features.

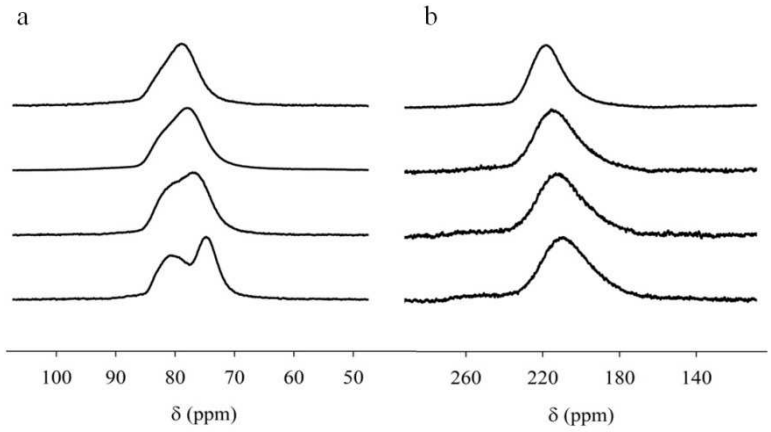

Figure 3.18 – a) ^{27}Al spectra for the series of sample; b) ^{71}Ga spectra (x = 0 on the top, x = 3 on the bottom).

The peak at around 76 ppm, which is characterized by a C_Q range between 3 and 6 MHz, has been attributed to the T^1 site, while the broader peak (C_Q 2-12 MHz) at around 83 ppm has been attributed to the T^2 site; the main difference between the two tetrahedral

units is the presence of a non bonding oxygen (NBO) in the coordination sphere of the T^2 site. A substantial linear correlation between the C_Q values and the distance Al^2-O^2 was found together with a correlation between the Al^2-O^2 distance and the cationic (La/Sr) coordination of the O^2 ions. From the NMR point of view, the T^2-O^2 bond has been found to be the main source of *EFG* at the T^2 site, giving origin to a broad distribution of C_Q values. The ultimate source of the distribution in the T^2-O^2 bond length is the cationic coordination of O^2 and the La/Sr local composition.

This is considered as the starting model for the further analysis of the $LaSr(Ga/Al)_3O_7$ and for best-fit of the spectra in order to obtain the quadrupolar parameters and the real isotropic chemical shift values. Results are reported in the Table 3.5.

Sample x	***Site***	δ_{iso} ***(ppm)***	C_Q ***(MHz)***	η	***Int. (%)***
3	Al2	83.3	0.2-11.5	0.5	68.3
	Al1	75.4	0.5-5.5	0.5	31.7
2	Al2	83.5	0.2-12	0.5	74.2
	Al1	77.6	0.5-70	0.5	25.8
1.5	Al2	83.8	0.2-12.5	0.5	67.8
	Al1	78.7	0.5-7.2	0.5	32.4
1	Al2	84.3	0.2-12.5	0.5	66.9
	Al1	79.7	0.5-7.2	0.5	33.1

Table 3.5 – Quadrupolar parameters from the fitting analysis of the 1D ^{27}Al spectra. The agreement factors are above 95% for all the fitting.

The chemical shift of Al^1 peak has a strongest dependence on the

sample composition with respect to the chemical shift variation for Al^2 peak. This general trend can be explained considering the de-shielding effect of the more electronegative gallium respect to aluminum. The T^1 site is connected to four tetrahedra while each T^2 site is connected to only three units, thus the contribution to the shift is higher for the T^1 site that can experience a largest number of Ga ions in the cationic coordination sphere. The local environment with the first coordination sphere of Ga/Al and La/Sr is reported in Figure 3.19.

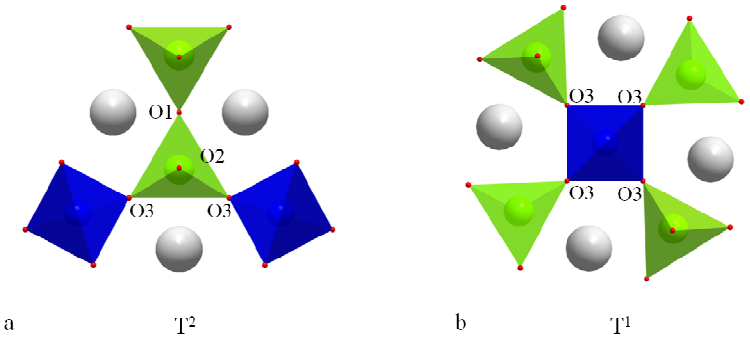

Figure 3.19 – Local environment of T^2 site (a) and T^1 site (b), the central tetrahedral are surrounded from the first La/Sr cationic sphere (grey ions) and Ga/Al unit (T^1 sites in blu, T^2 sites in green).

The variations in chemical shift and quadrupolar coupling constant ranges can be understood by considering both the anionic and the cationic coordination spheres of the two sites. Site T^1 is bonded to four O^3 oxygen; no NBOs are present in the T^1 unit. Around the T^1 polyhedron, four T^2 position are found together with 8 La/Sr sites. The distance T^1-(La/Sr) is always larger than the distance T^1-T^2 of ~1 Å for all the mixed samples Ga1Al2, Ga1.5Al1.5, Ga2Al1, thus the *EFG* is mainly attributable to the Ga/Al dispersion in the first cationic sphere; this can explain the strong effect both in chemical shift and in the variation in the C_Q

ranges with respect to the pure aluminum sample. The situation is different for the T^2 site, the coordination of which includes the presence of a NBO. The cationic coordination sphere is made up of three *T* units (one T^2 and two T^1) and 6 La/Sr positions. In this case the bond distances T^2-(La/Sr) and T^2-T are more similar (differences below 0.4 Å for all the samples Ga1Al2, Ga1.5Al1.5, Ga2Al1, with T^2-(La/Sr) shorter than T^2-T distance) and the C_Q ranges are dominated by the presence of the NBO and thus by the related La/Sr distribution. This can explain the small changes in chemical shift and C_Q values as they are related mainly to the La/Sr ratio, and only to a less extent to the Ga/Al composition.
In order to complete the analysis, also the ^{71}Ga solid state NMR was considered. Figure 3.18b presents the 1D ^{71}Ga spectra for all the samples. Contrary to what is observed for Al, in this case it is not possible to observe two distinct peaks for the two sites. It is very difficult to obtain well-resolved spectra of ^{71}Ga because of the second order quadrupole broadening of the central transition.
The chemical shift range confirms the tetrahedral coordination of the gallium ions.[76] The ^{71}Ga observed chemical shift is in good agreement with the shift obtained from the correlation relationship between ^{71}Ga and ^{27}Al shift.[77] However, on the basis of the accurate investigation on the ^{27}Al spectra it is possible to interpret the poorly resolved Ga signals. Also in this case a clear relation between the peak position and the composition of the samples is found. The observed variation of the chemical shift is opposite to the one observed for the Al spectra; this is coherent with the de-shielding effect of increasing amount of Ga and consequent shielding effect of Al.

3.5 - CONCLUSIONS

In this chapter we presented the $LaSr(Ga,Al)_3O_7$ series together with a new synthesis approach and we addressed the problem of local *vs*. average structure in the layered $LaSr(Ga,Al)_3O_7$ melilite-

like compounds. The use of both average (diffraction) and local experimental techniques (NMR), combined with DFT calculations, allowed us to obtain a detailed description of the system. Particular attention was devoted to the end member $LaSrAl_3O_7$, as a model system. The main results of this study on the end member can be summarized as follows:

- Two distinct Al tetrahedral sites are expected from the average crystal structure. The 1D and 2D NMR experiments confirmed the presence of these two Al moieties, but highlighted a significant difference in the distribution of C_Q for the two sites.

- DFT calculations allowed us to highlight a linear trend between the distortion parameter, Δ_{tetra}, and the C_Q distributions. Experimental and calculated C_Q values were in very good agreement.

- The presence of a NBO in the Al^2O_4 tetrahedra was the main cause of the differences in C_Q distributions for the two Al sites. In particular, the wide range of Al^2-O^2 bond lengths were due to the speciation of La/Sr cations around the O^2 position. We found a clear correlation between the Al^2-O^2 bond lengths and the O^2 cationic coordination, with the smallest Al^2-O^2 distances being related to the unique presence of Sr, whereas the largest ones are due to all La cations.

Moving to the entire system, we can state that local disorders can be conveniently modeled in terms of a Gaussian distribution of the quadrupolar parameters. More sophisticated approaches, such as the Czjzek distribution, do not offer a significant improvement of the fit quality, while leading to a less "physical" meaning of the best-fit parameters.

We also can state that combination of average and local experimental approaches with DFT calculations is a very powerful tool to investigate the subtle differences between local and average order in complex oxides. The importance of our results is made clearer considering that such structural details often strongly influence the functional properties of these materials.

3.6 - REFERENCES

1. H. Zhang, H. Yamada, N. Terasaki, C.N. Xu, *J. Electrochem. Soc.*, 155 (2008) J55.
2. C.K. Chang, T.M Chen, *Appl. Phys. Lett.*, 90 (2007) 161901-161903.
3. S. Yao,Y. Li, L. Xue, Y. Yan, *J. Am. Ceram. Soc*., 93 (2010) 3793–3797.
4. N. Kodama, Y. Tanii, M. Yamaga, *J. Lumin.,* 1076 (2000) 87–89.
5. M. Yamaga, Y. Tanii, N. Kodama, T. Takahashi, M. Honda, *Phys. Rev. B*, 65 (2002) 235108.
6. A.A. Kaminskii, L. Bohaty, P. Becker, J. Liebertz, P. Held, H.J. Eichler, H. Rhee, J. Hanuza, *Laser Phys. Lett*., 5 (2008) 845–868.
7. M. Akaki, J. Tozawa, D. Akahoshi, H. Kuwahara, *J. Phys. Conference Series*, 150 (**2009)** 042001.
8. A. Bao, C. Tao, H. Yang, *J. Mater. Sci.: Mater. Electr.*, 19 (2008) 476-481.
9. M. Rozumek, P. Majewski, L. Sauter, F. Aldinger, F., *J. Am. Ceram. Soc.,* 87*(* 2004) 662.
10. M. Rozumek, P. Majewski, H. Schluckwerder, F. Aldinger, K. Kunstler, G. Tomandl, *J. Am. Ceram. Soc.,* 87 (2004) 1795.
11. E.S. Raj, S.J. Skinner, J.A. Kilner, *Solid State Ionics,* 176 (2005) 1097.
12. X. Kuang, M.A. Green, H. Niu, P. Zajdel, C. Dickinson, J.B. Claridge, L. Jantsky, M.J. Rosseinsky, *Nat. Mater.*, 7 (2008) 498.
13. C. Tealdi, P. Mustarelli, M.S. Islam, *Adv. Funct. Mater.*, 20 (2010) 3874–3880.
14. A. Mancini, C. Tealdi, L. Malavasi, *Intern. J. of Hydrogen*

Energy, 37 (2012) 8073-8080.
15. M.R. Li, X.Kuang, S.Y. Chong, Z. Xu, C.I. Thomas, H. Niu, J.B. Claridge, M. J. Rosseinsky, *Angew.Chem. Int. Ed*. 49 (2010) 2362-2366.
16. M. Rozumek, P.Majewki, H. Schluckwerder, F. Aldinger, *J. Am. Ceram. Soc.*, 87 (2004) 1795-1798]
17. W. Ryba-Romanowsy, S. Golab, W.A. Pisarski, G. Dominiak-Dzik, M.Berkowski,A.Pajaczkowska, J. *Phys.Chem.Sol.*, 58 (1997) 639-645.
18. X. Kuang, M.A. Green, H. Niu, P. Zajdel, C. Dickinson, J.B. Claridge, L.Jantsky, M.J. Rosseinsky, *Nat. Mater*. 7 (2008) 498-504.
19. I. Pracka, W. Giersz, M. Swirkowicz, A.Pajaczkowska, S.Kaczmarek, Z.Mierczyk, K. Kopczynski, *Mater. Sci. Eng. B*, 26 (1994) 201.
20. B. Simondi-Teisseire, B. Viana, A.M. Lejus, D. Vivien, *J. Lumin.*, 971 (1997) 72-74.
21. S.I. Kubota, M. Izumi, H. Yamane, M. Shimada, *J. Alloys Comp*., 283 (1999) 95-101.
22. Q. Zhang, J. Wang, M. Zhang, Q. Su, *Appl. Phys. B: Laser Opt*., 92 (2008) 195.
23. G. Engelhardt, D. Michel, "*High Resolution Solid State NMR of Silicates and Zeolites*" Wiley& Sons, (1987).
24. R.A.Kinsley, R.J. Kirkpatrick, J. Hower, K.A., Smith, E.Oldfield, *Amer. Mineralogist*. 50 (1985) 537.
25. J-P. Gilson, G.C. Edwards, A.W. Peters, K. Rajagopalan, R.F. Wormsbecher, T.G. Roberie, M.P. Shatlock, *J. Chem. Soc. Chem. Comm.*, 91 (1987).
26. N. Kodama, T. Takahashi, M. Yamaga, Y. Tanii, J. Qiu, K. Hirao, *Appl. Phys. Lett*., 75 (1999) 1715.
27. P. Florian, E. Veron, T.F.G. Green, J.R. Yates, D. Massiot, *Chem. Mater.*, 21 (2012) 4068–4079.
28. C.J. Pickard, F. Mauri, *Phys Rev B*, 63 (2001) 245101.

29. M. Profeta, F. Mauri, C.J. Pickard, *J. Am. Chem. Soc.*, . 125 (2003) 541-548.
30. M. Profeta, M. Benoit, F. Mauri, C.J. Pickard, *J. Am. Chem. Soc.*, 126 (2004) 12628-12635.
31. F. Tielens, C. Gervais, J.F. Lambert, F. Mauri, D. Costa, *Chem. Mater.*, 20 (**2008)** 3336-3344.
32. G. Ferlat, T. Charpentier, A.P. Seitsonen, A. Takada, M. Lazzeri, L. Cormier, G. Calas, F. Mauri, *Phys. Rev. Lett*., 101 (2008) 065504.
33. A. Pedone, T. Charpentier, M.C. Menziani, *J. Mater. Chem.*, 22 (2012) 12599-12608.
34. A. Pedone, E. Gambuzzi, G. Malavasi, M.C. Menziani, *Theor. Chem. Acc.*, 131 (2012) 1147-1157.
35. A. Pedone, E. Gambuzzi, M.C. Menziani, *J. Phys. Chem. C*, 115 (2012) 14599-14609.
36. J.V. Hanna, M.E. Smith, *Solid State Nuclear Magnetic Resonance*, 38 (2010) 1-18.
37. T. Charpentier, M.C. Menziani, A. Pedone, *RSC Advances* 2013.
38. A. Pedone, T. Charpentier, G. Malavasi, M.C. Menziani, *Chemistry of Materials*, 22 (**2010)** 5644-5652.
39. S.E. Ashbrook, D.M. Dawson, *Acc. Chem. Res.,* DOI: 10.1021/ar300303w.
40. C. Bonhomme, F. Babonneau, C. Coelho, F. Pourpoint, T. Azaïs, S.E. Ashbrook, J.M. Griffin, J.R. Yates, F. Mauri, C.J. Pickard, *Chem. Rev.*, 112 (2012) 5733–5779.
41. C. Tealdi, C. Ferrara, L. Malavasi, P. Mustarelli, C. Ritter, A. Spinella, D. Massiot, P. Florian, *Journal of Materials Chemistry*, 22 (2012) 10488-10495.

42. H.M. Rietveld, *Acta Crystallogr*., 22 (1967) 151-152.

43. H.M. Rietveld, *J. Appl. Crystallogr*., 2 (1969) 65-66.

44. J. Rodriguez-Carvajal, *Abstracts of the Satellite Meeting on Powder Diffraction of the XVth Congress of the International Union of Crystallography, Toulose* (1990) 127.

45. P. Brown, S. Wimperis, *J. Magn. Reson.,* 128 (1997) 42-61.

46. T.F. Kemp, M.E. Smith, *Sol. St. Nuc. Mag. Res*., 35 (2009) 243-252.

47. For a detailed analysis, see G. Le Caër, B. Bureau, D. Massiot, *J. Phys.: Condens. Matter*, 22 (2010) 065402.

48. P. Florian, N. Sadiki, D. Massiot, J.P. Coutures, *J. Phys. Chem. B*, 111 (2007) 9747–9757.

49. M.D. Segall, P.J.D. Lindan, M.J. Probert, C.J. Pickard, P.J. Hasnip, S.J. Clark, M.C. Payne, *Journal of Physics: Condensed Matter*, 14 (2002) 2717-2744.

50. P.E. Blöchl, *Phys. Rev. B*, 50 (1994) 17953-17979.

51. J.R. Yates, C.J. Pickard, F. Mauri, *Phys. Rev. B*, 76 (2007) 024401.

52. J.P. Perdew, K. Burke, M. Ernzerhof, *Phys. Rev. Lett*., 77 (1996) 3865-3868.

53. J.K. Christie, A. Pedone, M.C. Menziani, A. Tilocca, *J. Phys. Chem. B*, 115 (2011), 2038-2045.

54. M. Choi, K. Matsunaga, F. Oba, I. Tanaka, *The Journal of Physical Chemistry C*, 113 (2009) 3869-3873.

55. G. Hautier, S. Ping Ong, A. Jain, C.J. Moore, G. Ceder, *Phys. Rev. B*, 85 (2012) 155208.

56. J.K. Lang, Y. Baer, P.A. Cox, *J. Phys. F: Metal Phys*., 11 (1981) 121-138.

57. M. Profeta, M. Benoit, F. Mauri, C.J. Pickard, *J. Am. Chem. Soc*., 126 (2004) 12628-12635.

58. A. Sadoc, M. Body, C. Legein, M. Biswal, F. Fayon, X. Rocquefelte, F. Boucher, *Phys. Chem. Chem. Phys.* 13 (2011) 18539-18550.

59. G.L. Turner, S.E. Chung, E. Oldfield, *J. Magn. Reson*., 64 (1985) 316-324.

60. C. Adamo, V. Barone, *J. Chem. Phys*., 110 (1999) 6158-6170.

61. B. Civalleri, D. Presti, R. Dovesi, A. Savin, *Chem. Modell.*, 9 (2012) 168-185.

62. "*Alternative Gate Dielectrics for Microelectronics*", Edited by G. Wilk and R.M. Wallace, Special Issue of *Mat. Research Soc. Bull.*, 3 (2002) 27.

63. T. Charpentier, P. Kroll, F. Mauri, *J. Phys. Chem. C*, 113 (2009) 7917-7929.

64. A. Pedone, T. Charpentier, M.C. Menziani, *Phys Chem Chem Phys*, 12 (2010) 5064-6066.

65. V. Kellö, A.J. Sadlej, P. Pyykkö, D. Sundholm, M. Tokman, *Chem. Phys. Lett*., 304 (1999) 414–422.

66. E. Gambuzzi, A. Pedone, M.C. Menziani, F. Angeli, D. Caurant, T. Charpentier, Accepted on *Geochimica et Cosmochimica Acta.*

67. K.J.D. Mackenzie, M.E. Smith, "*Multinuclear solid state NMR of inorganic materials"*, Oxford: Pergamon (2002).

68. A.P.M. Kentgens, *Geoderma*, 80 (1997) 271-306.

69. J.-B. D'Espinose de Lacaillerie, C. Fretigny, D. Massiot, *J. Magn. Reson*., 192 (2008) 244-251.

70. D.L.A.G. Grimminck, B. van Meerten, M.H.W. Verkuijlen, E.R.H. van Eck, A.P.M. Kentgens, , *J. Magn. Reson.,* 228 (2013) 116-124

71. M.E. Fleet, *Mineral. Mag*., 40 (1976) 531-533

72. G.J. Snyder, E.S. Toberer, *Nat. Mat.s*,7 (2008) 105-114

73. C.I. Thomas, X. Kuang, Z. Deng,H. Niu, J.B. Claridge, M.J., Rosseinsky, *Chem. Mater*., 22 (2010) 2510-2516.

74. C.Ferrara, C. Tealdi, A. Pedone, M.C. Menziani, A. Rossini, G. Pintacuda, P. Mustarelli, accepted on *J. Phyc. Chem. C.*

75. J.R. Goldsmith, F.Z. Laves, *Kristallogr.* 106 (1955) 213.

76. D. Massiot, T. Vosegaard, N. Magneron. D. Trumeau, V. Montouillout, P. Berthet, T. Loiseau, B. Bujoli, Sol. St. Nucl. Magn. Res., 15 (1999) 159.

77. K.J.D. Mckenzie, M.E. Smith, "*Multinuclear solid state NMR of inorganic materials"*, Pergamon (2002).

Chapter 4
The orthosilicates series
Li_2MSiO_4

4.1 – THE ORTHOSILICATE SYSTEM

Lithium-based rechargeable batteries are of growing interest among the electrochemical devices for energy storage thanks to the high gravimetric and volumetric energy density, the low toxicity, high stability and the possibility of being scaled from small portable devices to more demanding applications, such as automotive and smart grids.[1,2]

The great versatility of these devices is principally due to the possibility of tune the electrochemical properties by choosing proper anode, cathode and electrolyte materials. It is well known that the energy density in these systems is function of the specific capacity and potential of the electrodes. Carbonaceous systems (graphite) are well established as anode materials, whereas liquid organic mixtures or gels are currently used as the electrolyte. Many efforts have been done for the research of good cathode materials. It should be stressed that raw materials are the major contribution to the cost of large-scale lithium ion batteries and at present the cathode is the most expensive component.

The first commercial devices were based on $LiCoO_2$.[3] Starting from this system, a wide variety of related materials have been investigated:[4-6] doped and substituted $LiCoO_2$ phases, analog compound with the same crystallographic structure as $LiNiO_2$,[7] $LiNi_{0.5}Mn_{0.5}O_2$.[8] These systems are known as intercalation oxides and suffer for problems related to the low charge/discharge rates, high cost, toxicity. No further dramatic improvements in energy

densities are expected with the optimization of existing materials, thus the research for new materials is of central importance. Phosphate materials, particularly the olivine $LiMPO_4$ with *M* transition metal ions, have been proposed as valid alternative thank to their structural stability (due to the strong P-O bonds network), the reduced costs and high performances.[9-11] More recently, a new type of polyoxyanion structure has been proposed, with general formula Li_2MSiO_4 with *M* transition metal ion.[12-14] The orthosilicates are particularly attractive for their enhanced stability related to Si-O bonds, the low cost and environmental benignity due to the presence of Si. The key feature of these compounds is the possible extraction of two lithium ions per formula unit related to the M^{2+}/M^{3+} and M^{3+}/M^{4+} redox processes.
Fe-based systems have been widely studied thank to the good and promising electrochemical performances;[15,16] the Mn- based materials are even more promising thanks to the high potential of the $Mn^{2+/4+}$ couple respect to the Li^0. At the same time, the preparation of this material is not trivial due to the presence of secondary phases, impurities as MnO, $MnSiO_3$, Li_2SiO_3.[17-18] Also the structural stability under working conditions has been found to be a critical issue. The practical application of pure Li_2MnSiO_4 as cathode material is also limited by the low electronic conductivity ($5 \cdot 10^{-16}$ Scm^{-1}, about 5 order of magnitude smaller than that one observed for the $LiFePO_4$ system).[19] Many strategies were developed to enhance the electrical properties (carbon coating, nano-structures). Another strategy is the research for substitution and doping that, at the same time, can improve the structural stability under working conditions, maintain the advantages related to the presence of the high-voltage couple $Mn^{2+/4+}$ species and enhance the electronic conduction. For these reasons, many series of samples $Li_2M_xM'_{1-x}SiO_4$ (with *M* transition metal ions) were been explored, with particular attention for the couple Fe/Mn.[20,21]

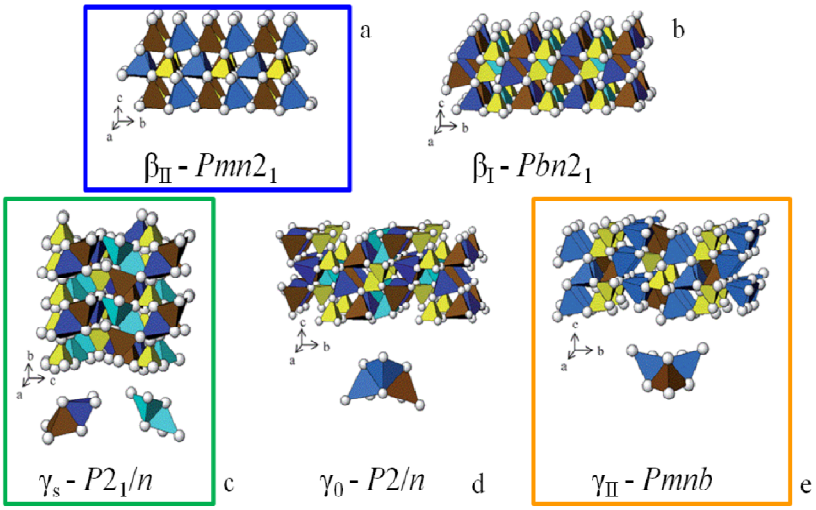

Figure 4.1 – β and γ polymorphs for the silicates system;[25] SiO_4 (yellow); MO_4 (brown); LiO_4 (blue); light and dark blue tetrahedra represent crystallographically distinct lithium sites. (a) β_{II} structure; all the tetrahedra point in the same direction, perpendicular to the plane of the packing; tetrahedra are linked trough corners (bridging oxygens); (b) β_I structure, all tetrahedra are oriented along the same direction; chains of alternating LiO_4 and MO_4 tetrahedra along a direction are alternated and parallel to chains of alternating LiO_4 and SiO_4 tetrahedra; (c) γ_s structure, half tertahedra point in opposite directions; pairs of LiO_4/MO_4 and LiO_4/LiO_4 edge-sharing tetrahedra are found, (d) γ_0 structure, the tetrahedra are arranged in subgroup of three units with the central tetrahedron pointing in the opposite direction to the outer two; the group of 3 edge-sharing tetrahedra are sequences of Li–Li–M; (e) γ_{II} structure, units of 3 edge-sharing tetrahedra compose a sequence of Li–M–Li.
Only β_{II}, γ_s and γ_0 structures are found for Mn/Fe compositions.

Despite of the number of different works and approaches to the study of this class of compounds, still many structural issues are unclear. The polymorphism, due to the small energy differences between the different polymorphs, is maybe the most critical issue: the problem of different possible phases exists for the pure composition (only one transition metal) and is exacerbated by the presence of more than one transition metal species in the structure. It has been found that the presence of a particular polymorph depends on the synthetic route, the composition, the sintering temperature, the heating/cooling rate. Different polymorphs exhibit very similar structure but a potentially different functional behavior. A complete study and comprehension of this class of compounds is needed as preliminary step for further investigation.

The orthosilicates have tetrahedral structure;[22-24] This structure is based on the disposition of oxygen ions in tetragonally-packed arrangements; here, cations occupy only one half of the tetrahedral site available so a network of tetragonal units linked trough corners (and not trough face sharing) is obtained. Different sites are available for cations, which gives rise to structural distortions and small changes in symmetry that are reflected in the rich polymorphism above mentioned. The different classes of polymorphs can be divided into two main groups, called β and γ, which are stable at different temperature.

The two classes chiefly differ because in the β structure (stable at lower temperature) all the polyhedra point along the same direction, while in the γ phases (more frequent at higher temperature) the tetrahedra are found in groups of three units with the central one pointing in the opposite direction with respect to the other two.

Where both β and γ forms exist for each composition, the phase transition from β to γ implies the inversion of half sites. Many different structures have been identified and related to these two

categories, and many controversial determinations have been proposed.

The problem related with the accurate structural characterization is due to the wide number of possible crystal structures and to the great similarities between all of them. Standard diffraction techniques are not able to address completely this point, since very similar structures generate very similar diffraction patterns; this give rise to ambiguous and non-unique indexing of the patterns. The presence of impurities, the possibility of obtaining a mixing of two polymorphs, the presence of more than one transition metal ion in the mixed composition samples greatly exasperate the problems related to the use of diffraction. The main strategy in the structural determination of these compounds is the use of local probes, as the major differences and critical issues are found in a local scale. Therefore, solid-state NMR is an essential tool for the structural determination in this field, as already proposed and established in the literature.[13,17,20] Since the average structure of the different polymorphs chiefly differs in connectivity between tetrahedra, local distortions and changes in relative orientations of different units, the study of local environments of different nuclei becomes essential.

Many different studies focus the attention on the use of lithium NMR, as lithium ions are directly involved in the electrochemical reaction and thus of primary interest. In this frame, ^{6}Li has been by far the most investigated nucleus, thanks to the possibility of obtaining good resolution (albeit it is a quadrupolar nucleus, *I=1*), in spite of serious problems related to its low natural abundance (7.59%) and then low sensitivity. The ^{6}Li studies have led to a strong correlation between chemical shift values and the different polymorphs, so stating that NMR is of a great help in the study of such materials. At the same time, scarce ^{7}Li NMR studies have been performed due to more intense coupling of quadrupolar and paramagnetic interactions.

Here we propose the use of ^{7}Li NMR, maintaining the high resolution given by ^{6}Li and bypassing the problems related to low sensitivity, and also the use of ^{29}Si NMR, which is attempted for the very first time on isotopically-enriched samples, in order to obtain more information also on the structure backbone.

4.2 – Experimental section

Synthesis **-** The $Li_2Mn_{1-x}Fe_xSiO_4$ (x = 0, 0.25, 0.5, 0.75, 1) samples were prepared by sol-gel synthesis. $FeC_2O_4{\cdot}2H_2O$ (Aldrich 99.99+%) or $Mn(CH_3COO)_2{\cdot}4H_2O$ (Aldrich 99+%), $LiCOOCH_3{\cdot}2H_2O$ (Fluka >99%) and ^{29}Si enriched TEOS in stoichiometric ratios were dissolved in ethanol and the solution was stirred at 50°C until the solvent evaporation. The precursor was dried in a muffle at 80°C overnight, and then treated in argon atmosphere at 700°C for 8 hours. This procedure was carried out in a dry-box under Argon atmosphere, and leaving the initial solution to evaporate in this atmosphere. In the following, the samples will be named Mn1 (x = 0), Mn075 (x = 0.25), Mn05 (x = 0.5), Mn025 (x = 0.75) and Fe1 (x = 1).

Diffraction analysis **-** In-house X-ray powder diffraction measurements were performed using a Bruker D5005 diffractometer with the Cu-Kα radiation, graphite monochromator and scintillation detector. The patterns were collected with a step size of 0.02° and counting time of 10 seconds per step in the angular range 15-80°. Rietveld structural and profile refinement was carried out by means of TOPAS V3.0 program.[26] During the refinement, lattice parameters, isotropic thermal factors, atomic positions were allowed to vary. The weight percentage of the impurity phases was also determined.

Solid state NMR - The ^{7}Li MAS NMR data were acquired with a Bruker Avance III spectrometer at a field of 11.7 T, operating at a

Larmor frequency of 194 MHz, equipped with an HX 1.3 mm probe. The spectra were recorded under 60 kHz MAS using a double-adiabatic spin-echo sequence employing a pair of tanh/tan short high-powered adiabatic pulses (SHAPs),[27] each of duration 50 μs and radiofrequency field amplitude 455 kHz. The chemical shift scale was referenced relative to the ^{7}Li resonance in LiF. The time constants T_2' describing the homogeneous decay of the transverse magnetization were determined using the same pulse sequence. The spectra correlating the spinning sideband manifolds against the isotropic shifts were obtained using the recently-published aMAT sequence.[27] The evolution time was 20 rotor periods (333.33 us), and a spectral width of 384.6 kHz in the indirect dimension that was sampled with 128 increments acquired according to the echo/anti-echo protocol. 64 scans per increment were obtained.

The ^{29}Si MAS NMR data were acquired with a Bruker Avance III spectrometer at a field of 11.7 T, operating at a Larmor frequency of 99.362 MHz, equipped with an HX 1.3 mm probe. The spectra were recorded under 60 kHz MAS using a double-adiabatic spin-echo sequence employing a pair of tanh/tan short high-powered adiabatic pulses (SHAPs), each of the duration 50 μs with radiofrequency field amplitude of 227 kHz. The chemical shift scale was referenced relative to the ^{29}Si resonance in TMS. The time constants T_2' describing the homogeneous decay of the transverse magnetization were determined using the same pulse sequence. The aMAT spectra were acquired with a evolution time of 7 rotor periods (116.67 us), and a spectral width of 870 kHz in the indirect dimension that was sampled with 100 increments acquired according to the echo/anti-echo protocol.
The best-fits were performed with the Sola routine of Topspin (Bruker), by including the isotropic peaks and the spinning sidebands pattern.

4.3 – RESULTS AND DISCUSSION

4.3.1 –Diffraction analysis

The series of sample $Li_2Mn_{1-x}Fe_xSiO_4$ (x = 0, 0.25, 0.5, 0.75, 1) has been prepared in small quantities (few hundreds milligrams) according to a sol gel procedure. Many different synthetic approaches have been proposed and it appears difficult to find a unique optimum synthesis procedure independent from the composition. Solution syntheses were found to be the best route to obtain these compounds, particularly the hydrothermal method in controlled atmosphere was widely used.[28,28] In this work we propose the sol gel procedure in controlled atmosphere for the preparation of all the samples of the series. This route was already presented in the literature as a possible alternative to hydrothermal methods.[20]

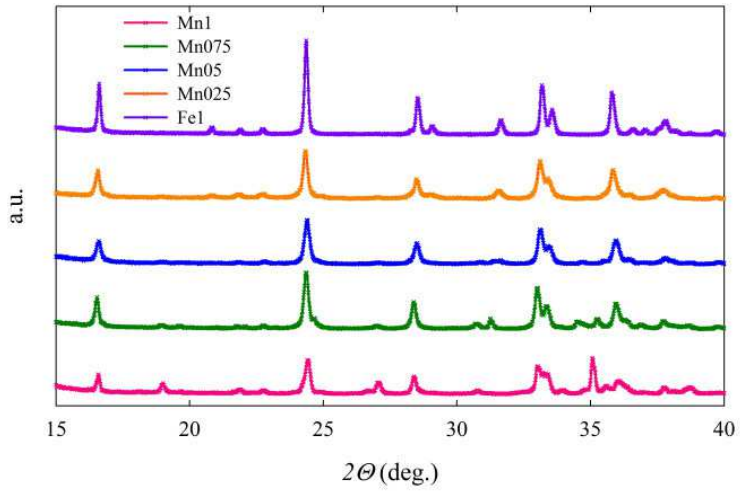

Figure 4.2 – X ray powder diffraction patterns for the whole series of samples.

The synthesis products were routinely checked trough X-ray powder diffraction measurements, and the results are presented in Figure 4.2.

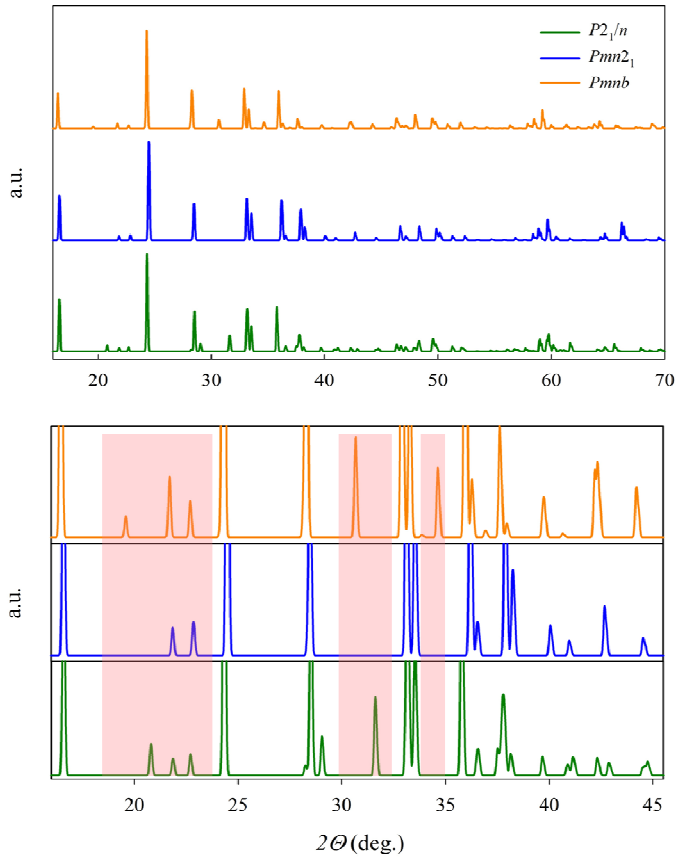

Figure 4.3 – Simulated X ray diffraction patterns normalized to the intensity of the principal peak for the Pmnb (orange) $Pmn2_1$ (blu) and $P2_1/n$ (green) phases obtained for the Li_2FeSiO_4 composition in the angular range 15°- 70° (upper panel) and zoom in the angular range 15°-46° (lower panel).

The powder patterns clearly indicate the change of the symmetry with composition and the possibility of the presence of more than one phase in any sample. Rietveld refinements were performed for all the samples. Considering the well-known and rich polymorphism that affects this class of compounds, all the possible known structures were considered during the refinement process. At the same time, unambiguous indexing is still a problem since, as already stated, many structures differ from each other only for distortions or small changes in the symmetry elements and thus generate very similar diffraction patterns.

The possible know phases for the silicates family are reported in Figure 4.1. For the Mn/Fe samples it was found that only one low temperature structure can be obtained, *i.e.* the β_{II} phase; similarly, only γ_S and γ_0 are obtained at higher temperature. The diffraction patterns originated from these structures are then considered.
The simulated patterns are very similar, having most of the reflections at the same positions and with comparable intensities, as reported in Figure 4.3. Particularly the main peak is found at the same position for all the patterns, and also the relative intensities of the other main peaks are found to be very similar.
Considering the range 15° - 46°, it is still possible to identify some features which are useful for the identification of a single polymorph. The zone in the range 18° - 23° presents a different number of reflections with significantly different positions. Similar considerations can be done for the region 29° - 32° and 34° - 35°. These zones can be considered the fingerprint of the different polymorphs. The discrimination between the $P2_1/n$ and the *Pmnb* and between the $P2_1/n$ – $Pmn2_1$ phases seems to be possible based on the analysis of the mentioned reflections, in contrast a unique identification of the *Pmnb* and $Pmn2_1$ cannot be performed only with the use of diffraction measurements as the $Pmn2_1$ phase has few reflections, and most of them are superimposable to the pattern originated by the *Pmnb* one.

Furthermore, it is necessary to consider that experimentally many terms can affect the broadening of the reported simulated peaks (thermal motion of ions, disorder, presence of defects, grain size, instrumental factors). If impurities or a mixture of different polymorphs are present, the analysis is further complicated. From this analysis is evident that the structural characterization of this class of compounds must be carried out with the combined used of different techniques.

In the next sections we will start with a discussion on the NMR Hamiltonian of the different systems with a particular focusing on the paramagnetic terms, in order to better understand the NMR signals of the different samples. The effects of substitution from Mn to Fe will be discussed. In the second part, each sample will be considered individually and the structural characterization will be attempted by combining diffraction and NMR data. We will start with the results obtained for the two end members, Mn1 and Fe1, as they can be considered the two models for the understanding of the mixed samples and will constitute a good starting point for the successive discussion.

4.3.2 – NMR study

Paramagnetic Hamiltonian

Paramagnetic interaction takes place between the nuclear spin and the spins of localized unpaired electrons related to the presence of transition metal ions. A detailed general discussion is presented in the Chapter 1 (section 1.4.7 and 1.5.3), here only the main equations will be recalled. The electron spin resonance Hamiltonian in the case of the high temperature limit can be expressed with the following formula

$$H_{ESR} = -\gamma B_0 \cdot (1 - \sigma_{orb}) \cdot I + \mu_B B_0 \cdot g \cdot \langle S \rangle \qquad (4.1)$$

$$+\langle S\rangle \cdot A \cdot I + \langle S\rangle \cdot D \cdot \langle S\rangle$$

Where all the terms have been presented and discussed in the previous Chapter 1, Section 1.4.7.
The hyperfine shift can be rewritten according to the following expression

$$\delta_{HF} = \frac{S(S+1)\mu_B}{3kT\gamma} g \cdot A \qquad (4.2)$$

Where the hyperfine interaction between the nucleus and the electronic spin can be seen as a sum of different terms

$$A = A_{FC} + A_{SD} + A_{PC} + A_{SD,2'} + A_{AS} \qquad (4.3)$$

where A_{FC} is the Fermi contact contribution, A_{SD} is the dipolar coupling between I and S, A_{PC} is the pseudo contact term, $A_{SD,2'}$ is the second order term of the dipolar coupling, A_{AS} is the anti-symmetric component of the tensor.

The hyperfine term is different in the case of a spin-only or a spin-orbit systems; the first two terms of the above expression for A tensor are necessary to describe the spin only system, while for spin-orbit coupled systems the whole expression must be considered. The two end members of the silicates series, Mn1 and Fe1, are model examples for these two situations. The Hamiltonian for these two cases is now considered together with the effect of the ^{29}Si and ^{7}Li spectra.

Spin only system – Mn^{2+}

The pure manganese sample Mn1 contains only Mn^{2+}, with electronic configuration d^5 and thus can be considered as a spin only system. In this case the hyperfine term is simplified in the sum of only two contributions: the Fermi contact term, resulting in the paramagnetic shift, and the dipolar interaction between the

nucleus and the electrons spin resulting in the anisotropy and thus in the sideband pattern. The ^{29}Si spectra can be analyzed according to this picture. Both the Fermi contact and dipolar coupling terms are of the same order of magnitude: paramagnetic shifts are of the order of thousand of ppm, the same is for the anisotropy

$$A_{Mn^{2+}} = A_{FC} + A_{SD} \tag{4.4}$$

The broadening of the sidebands can be due to the presence of temperature gradients inside the rotor, due to the friction generated by the *UFMAS*. In fact, the temperature is a function of the spinning speed, ν_r, and the temperature difference between the temperature of the gas and the temperature of the samples has been related to the viscosity of the gas, η_s, the radius R of the spinner and the thermal conductivity λ of the gas by the equation[29]

$$T_{sample} - T_{inlet} = \frac{3\pi^2 \eta_s R^2 \nu_r^2}{\lambda} \tag{4.5}$$

Therefore, the raising of the temperature generates temperature gradients that still need a full characterization. The hyperfine shifts has inverse temperature dependence, and small changes in temperature can give very different anisotropies. Thus, crystallites in different positions can be affected by different broadenings, which are very difficult to simulate.

The effect of these interactions of the ^{7}Li spectra is pretty different. In lithium orthosilicates, the Fermi contact term for the lithium is considerably smaller respect to that of ^{29}Si: the observed shifts are in the range of 0 - 200 ppm. This is a measure of the small spin density on the site of the lithium ions, which reveals an inefficient Fermi contact mechanism. In both cases, there are two chemical bonds between the paramagnetic center and the considered nuclei: Li-O-Mn and Si-O-Mn; the difference between the two cases can

be explained considering the different character of the chemical bond, that is predominantly ionic for lithium while is strongly covalent for silicon. The anisotropy is related to the presence of the dipolar coupling interaction that gives origin to broadening of thousands ppm.

Spin orbit system – Fe^{2+}

The Fe^{2+} ion has electronic configuration d^6, the spin-orbit interaction must be considered, and thus the shift is likely due to the Fermi contact and pseudo-contact terms. Similarly, the sideband pattern contains contributions from the dipolar interaction to the first and second order.
The whole expression of A is needed for an accurate description of the system and of the ^{29}Si signals

$$A_{Fe^{2+}} = A_{FC} + A_{SD} + A_{PC} + A_{SD,2'} + A_{AS} \qquad (4.6)$$

At the same time, for similar systems and from calculations[31] it was evident that the contributions from the terms raising from the spin-orbit interaction are negligible with respect to the shift and anisotropy given by the spin-only terms (around 1%) and thus the spectra shifts can be efficiently evaluated considering only the main Fermi contact interaction. For the evaluation of the anisotropy, in contrast, the term arising from the dipolar coupling due to the spin-orbit interaction cannot be neglected. Also in this case, however, the intensities of the sideband patterns are heavily affected by the temperature dependence introduced by temperature gradients and a corrected quantitative analysis is very difficult.

The lithium spectra for the iron-containing samples can be explained considering the Fermi contact and the pseudo-contact shifts that have similar relevance. The Fermi contact interaction with lithium ions can be treated according to consideration similar

to those valid for the manganese case. From the computational point of view, the calculation of the pseudo-contact contribution is very demanding, and the expectation values for lithium shifts in spin-orbit coupled systems are still not available, although studies in this sense are currently underway.
On the basis of these general considerations, the analysis of the whole series of samples is proposed below.

4.3.3 - Li_2MnSiO_4

The pure manganese composition was found to be difficult to obtain as the synthesis often leads to the formation of impurities, mainly Li_2SiO_3 and Mn_2SiO_4.[32,33] The optimal synthetic route that allows to isolate a pure polymorph is not yet identified and many different procedures have been proposed.[18,31,34] At least three different polymorphs are reported to exist as products of synthesis at ambient pressure:[35] the *Pmn*2$_1$ and *Pmnb* orthorhombic phases and the monoclinic *P*2$_1$/*n* one. The two orthorhombic polymorphs seem to be more stable than the monoclinic form that can be obtained only from quenching from 900°C heating treatment. The same polymorphs are also obtained as the result of different heating treatments after hydrothermal synthesis (pressure ~ 10 bar).[34] Solid state reaction followed by heating at 700°C leads to the formation of *Pmn*2$_1$ phase together with intermediate products that react completely at 900°C.[33] At the same time, Politaev et al. found that the synthesis can be completed, obtaining *P*2$_1$/*n* phase, only up to 1150°C.[18] Starting from the sol gel procedure, it was found that heating treatment at 600°C lead to a mixture of *Pmn*2$_1$ phase and unreacted materials while treatments up to 800°C give the desired composition together with impurities (Li_2SiO_3 and Mn_2SiO_4 as found following also other procedures), the effective temperature is 700°C that leads to the most pure sample.[32]
It seems evident that the synthesis of this particular composition is extremely dependent on the experimental conditions, and it is

very difficult to isolate a unique polymorph. In this context the use of diffraction analysis is often not decisive, as previously discussed in this chapter. From the analysis of the literature data, *Pmn*2$_1$ and *P*2$_1$/*n* polymorphs can be expected. The experimental powder pattern revealed also the presence of impurities as Li_2SiO_3 and MnO; the experimental data are found to be compatible with more than one combination of different phases.

At the same time, a deep and detailed analysis of the ^{6}Li spectra was performed for the identification and attribution of the different pure-Mn polymorphs; particularly, the chemical shifts and anisotropies of the different phases were reported.[34] The ^{7}Li NMR spectra are thus essential for the structural characterization of this sample.

The 1D spectrum (Figure 4.4) shows a complex pattern with several different contributions. The signals around 0 ppm can be related to diamagnetic impurities such as the lithium silicates also observed with XRD.[36] Signals at unusual shifts are observed at ~36 and ~ 77 ppm; these signals must be related to a paramagnetic phase, since the ^{7}Li chemical shift range for diamagnetic samples is usually in the range of +5, -5 ppm.[37] XRD powder diffraction measurements reveal the presence of MnO and no other lithium containing impurities. Therefore, it is possible to hypothesize the presence of lithium defects in the MnO and Mn_2SiO_4 phases or Mn defects in the Li_2SiO_3 that can explain the presence of the two shifted signals in the positive ppm region.

It is not possible to quantify the amount of impurity from the NMR measurements as the T1 of the different diamagnetic and paramagnetic phases can be different and thus the measurements are not quantitative. On the contrary, it is still possible to correctly estimate the amount of the different polymorphs, since all of them are affected by the paramagnetic interaction which translates into very short T1. The T1 of the polymorphs was 730 μs, similar values were obtained for related systems.

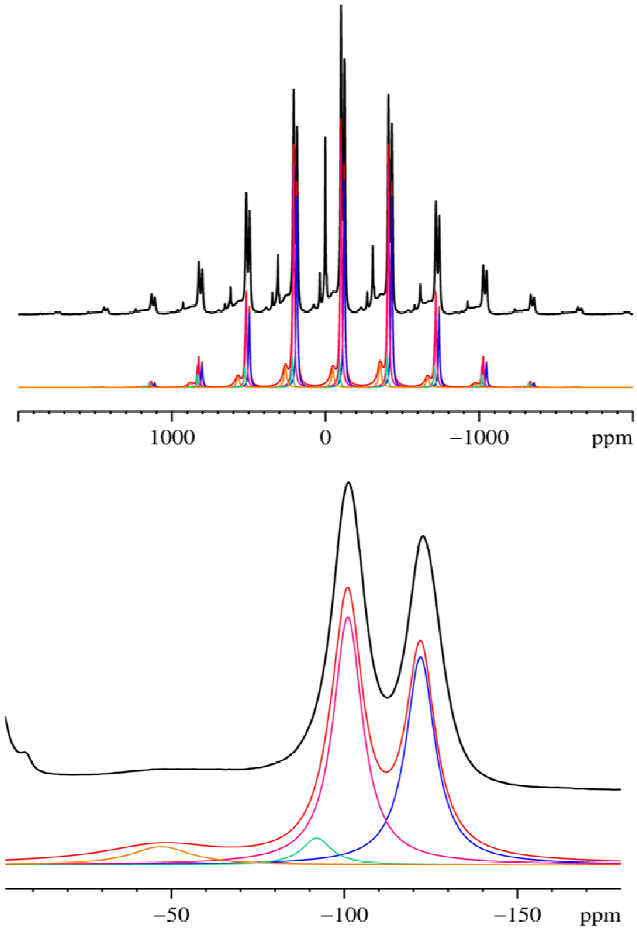

Figure 4.4 – Mn1 ^{7}Li 1D experimental spectrum (black) and fitted pattern (red) with components for $Pmn2_1$ (blue), Pmnb (pink), $P2_1/n$ (green and orange) lithium sites.

The peaks in the chemical shift range -40; -160 ppm can be associated to different polymorphs. Figure 4.4 shows the best-fit of the central band.

The spectrum can be interpreted with the use of four distinct contributions: the peaks at -122 ppm and at -101 ppm were attributed to the *Pmn*2$_1$ and *Pmnb* phases respectively.[34] The two smallest contributions at -93 and -47 ppm are assigned at the two lithium sites of the *P*2$_1$/*n* phase. A mixture of three different polymorphs must be therefore considered.

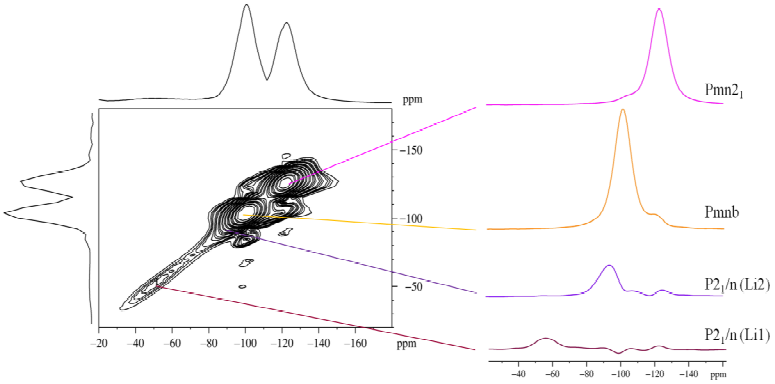

Figure 4.5 – Mn1 ^{7}Li 2D aMAT spectrum with slices extracted from the indirect dimension; contributions from Pmn2$_1$ (pink), Pmnb (orange), P2$_1$/n (light and dark violet) lithium sites have been extracted.

This analysis is confirmed also by the evaluation of the anisotropies of the sideband patterns. In the *Pmn*2$_1$ and *Pmnb* structures the lithium ion is surrounded by four manganese ions at the corners of slightly distorted tetrahedra; in the *P*2$_1$/*n* structure two lithium ions are present, both surrounded by four manganese positions but, in this case, the central lithium is not at the center of this tetrahedral but dislocated near to one of the Mn-Mn edge. This is expected for Li1 position and Li2, but Li2 has an even less symmetric position. As the anisotropy parameters reflect

local symmetry, the analysis of the sideband patterns for the different polymorphs can give relevant information.

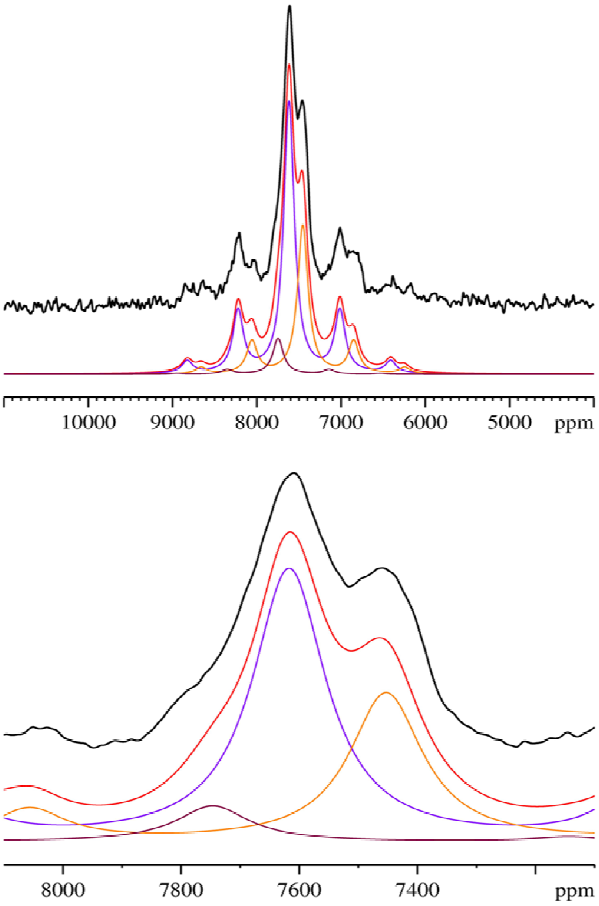

Figure 4.6 – Mn1 ^{29}Si 1D experimental aMAT spectrum (black) and fitted profile (red) with components relative to Pmn2$_1$ (orange), Pmnb (violet), P2$_1$/n (purple) silicon signals.

The best fit of the spectrum, presented in Figure 4.4, considering these four contributions gives satisfactory results, in good

agreement with anisotropy and shift values reported in literature for ^{6}Li of these compounds. This result is confirmed also by the 2D ^{7}Li spectrum. Figure 4.5, from which the presence of four peaks is evident, and also by the ^{29}Si spectrum (see below). From the 2D spectrum it is possible to extract the different contributions to the isotropic dimension, and thus isolate the signals originated from different sites and polymorphs. Also the 1D spectrum extracted from the indirect dimension projection can be fitted according to result obtained from the fit presented in Figure 4.4 and Table 4.1. Our results are in very good agreement with data reported in literature for a similar composition.[34]

The ^{29}Si 1D spectrum, presented in Figure 4.6, is shifted of ~7500 ppm from the zero and it extends over a range of 3000 ppm. This spectrum can be compared to the one obtained for the system Li(Fe/Mn)PO_4.[38] The shift of the ^{31}P for the pure manganese samples was found to be of 7879 ppm, near to the shift range of 7800-7400 ppm for the observed ^{29}Si peaks in the orthosilicates system.

The similarities in the chemical shift of the two distinct nuclei can be explained considering that the shift is dominated by the paramagnetic interaction that in both cases is due to the Mn^{2+} species. Mn^{2+}, as discussed in the previous part of this chapter, gives origin to a strong Fermi contact contribution that is the origin of this massive paramagnetic shift. Indeed, the different coordination of the paramagnetic ion (octahedral in the phosphate material and tetrahedral in the silicate) gives only a second order contribution to the shift. For the d^5 ion the magnetic susceptibility tensor is expected to be isotropic and, as a consequence, the paramagnetic shift is totally due to the strong Fermi contact interaction, as extensively discussed in previous sections. The Fermi contact is dumped quickly with the increasing number of bonds between the observed nucleus and the paramagnetic center and is also a function of the character of the involved chemical

bonds; the strong covalent Si-O bond, as P-O, provides a efficient pathway for the electron spin delocalization to both nuclei giving origin to these huge shifts.

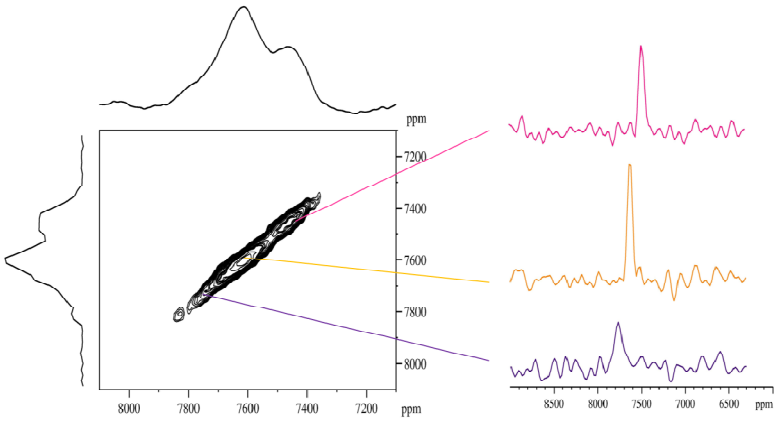

Figure 4.7- Mn1 ^{29}Si experimental 2D aMAT spectrum (black) with slices extracted from the indirect dimension in order to isolate contributions relative to $Pmn2_1$ (pink), Pmnb (orange), $P2_1/n$ (purple) sites.

Considering the local environment of silicon ion in the three polymorphs and the relative intensities of the signals a possible assignment of the peak of the silicon spectra is proposed and reported in Table 4.1. The evaluation of the first cationic coordination sphere for the silicon ion in the different phases is essential for the understanding of the different value of the observed chemical shift and anisotropy values. In order to confirm the proposed attribution, a deep DFT analysis as it allows to consider the effect of the distance between the Si ion and the metal center and the effect of the changes in the values of the angle Si-O-M.

Phase	*Shift (ppm)*	*Anisotropy parameter (ppm)*	*Shift (ppm)*	*Anisotropy parameter (ppm)*
	^{7}Li		*^{29}Si*	
Pmn2$_1$	-122	-820	7453	880
Pmnb	-101	-800	7617	900
P2$_1$/n –Li2	-93	-1250	7747	710
P2$_1$/n –Li1	-47	+ 1000		

Table 4.1 – Chemical shift and anisotropy values for ^{7}Li and ^{29}Si spectra of the Mn1 sample.

The analysis of the 2D ^{29}Si spectrum confirms the presence of at least three different contributions to the overall signal; considering the relative ratio between the phases obtained from the analysis of ^{7}Li measurements, it is possible to propose the attribution of the silicon signals. Results are reported in Table 4.1.

4.3.4 - Li_2FeSiO_4

The different Li_2FeSiO_4 polymorphs were isolated under different synthesis conditions. The *Pmn*2$_1$ phase (β_{II} structure) has been obtained from hydrothermal synthesis at 200°C,[39] at intermediate temperature the *P*2$_1$/*n* phase (γ_s structure) is stable (600°-800°C)[25] while it is possible to isolate the *Pmnb* phase, known as γ_{II} structure, from quenching the sample at 900°C.[28,39]
Our Li_2FeSiO_4 sample presents a X ray powder diffraction pattern (Figure 4.2) that can be indexed with the only use of *P*2$_1$/*n* space group. The NMR data confirm this result. ^{7}Li 1D e 2D spectra, reported in Figure 4.7 and 4.8, are dominated by the paramagnetic interaction. The sideband manifold extends over a wide frequency range (more than 4000 ppm) and the central band can be identified in the range 50, - 150 ppm.

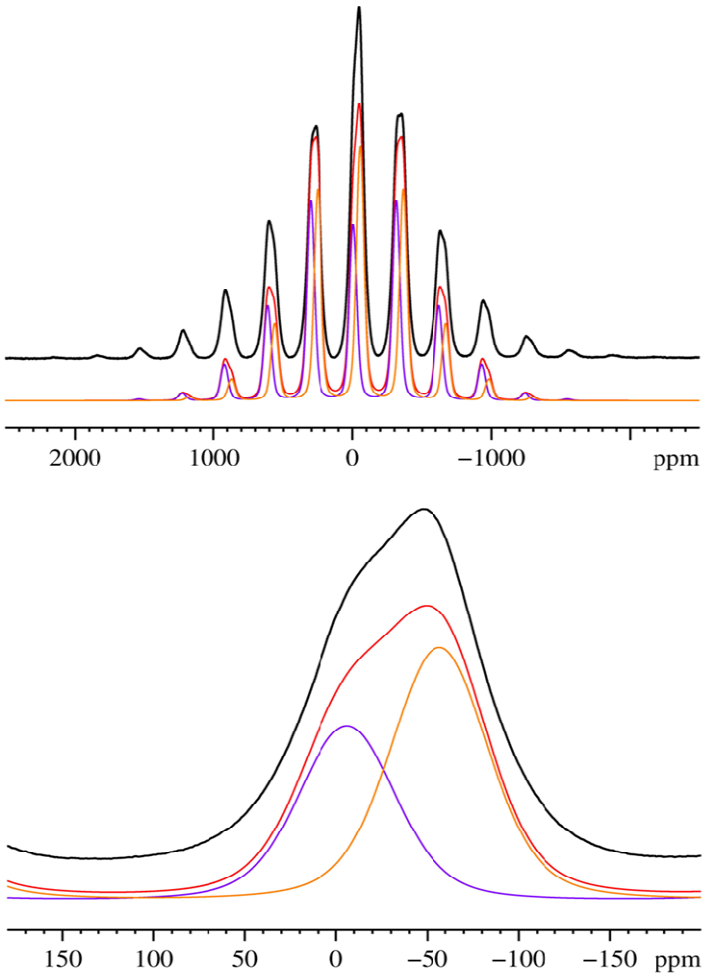

Figure 4.8 – 1D ^{7}Li experimental spectrum (black) with fitted spectrum (red) and the two components of the $P2_1/n$ phase, Li1 (violet) and Li2 (orange) for composition Fe1.

The 1D spectrum can be fitted by considering two contributions with chemical shift -6 and -56 ppm of relative ratio 1:1; these two peaks are attributed to the two crystallographically non-equivalent lithium sites, Li1 and Li2, of the $P2_1/n$ structure. This result is in good agreement with the literature.[28] A similar sample, with the same composition, was prepared according to a different synthetic route. The ^{6}Li spectrum in this case presents isotropic shifts of -7 and -55 ppm. Also the anisotropy parameters for the two sites are similar to those reported for ^{6}Li.[20,28,39]
The overall broadening of the spectrum is directly related to the strength of the dipolar interaction between the nuclei and the paramagnetic centers (trough-space interaction), and particularly with the magnitude of the anisotropy of such an interaction; in this case it is possible to differentiate between the two lithium sites present in the $P2_1/n$ structure because they have significantly different inter-atomic distances from Fe ion (only one crystallographic site).

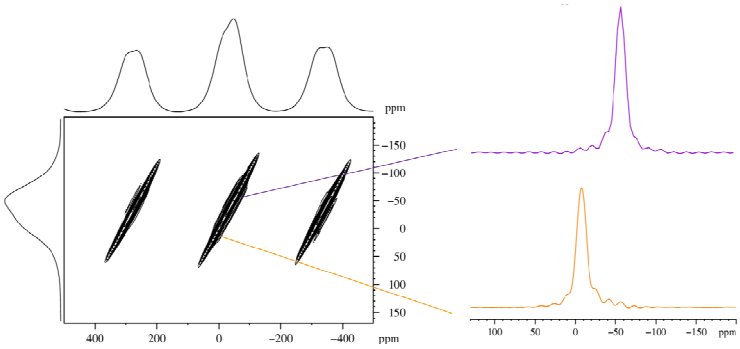

Figure 4.9 - 2D ^{7}Li spectrum for the Fe1 composition; splices extracted from the indirect dimension relatives to the two sites of the $P2_1/n$ phase.

The Li1 unit co-shares a edge with the FeO_4 polyhedron and has a shorter distance (~2.7 Å) respect with the two Li2 sites (linked to

FeO_4 unit trough bridging oxygen) placed at ~ 3.9 Å. The interaction between Li1 and the Fe center is stronger and induce a larger broadening in the spectrum. The narrower powder pattern with isotropic shift at -57 ppm was attributed to Li2 site, while the broader pattern with isotropic shift -9 ppm was related to Li1 site.[28,39] The 2D aMAT experiment was also collected for ^{7}Li to try to resolve and separate the two overlapping sideband patterns of the two lithium sites; the spectrum is presented in Figure 4.9. On the indirect dimension it is possible to observe the isolated centre band of the two lithium sites. The 2D signal does not allow to separate the two contributions, since they have very similar isotropic shifts due to very similar local environments but it is still possible to identify the two contributions.

1D spectrum of ^{29}Si was acquired, results are presented in Figure 4.10. From the 1D spectrum it is possible to observe a single site, as expected from the crystal structure. Also the 2D aMAT spectrum was acquired as reference data for the analysis of mixed samples as from the 2D it is possible to extract the 1D isotropic peak; it is presented in Figure 4.11. The ^{29}Si spectrum is characterized by a width of 3000 ppm, and the isotropic chemical shift can be identified at 3386 ppm. Again, this shift is due to both the Fermi contact and pseudo-contact interactions. Similar shifts were found for ^{31}P in the related system Li(Fe/Mn)PO_4.[38]

Phase	***Shift (ppm)***	***Anisotropy parameter (ppm)***	***Shift (ppm)***	***Anisotropy parameter (ppm)***
		^{7}Li		***^{29}Si***
$P2_1/n$ –Li2	-57	-1250	3386	1000
$P2_1/n$ –Li1	-6	+ 1000		

Table 4.2 – Chemical shift and anisotropy values for ^{7}Li and ^{29}Si spectra of the Fe1 sample.

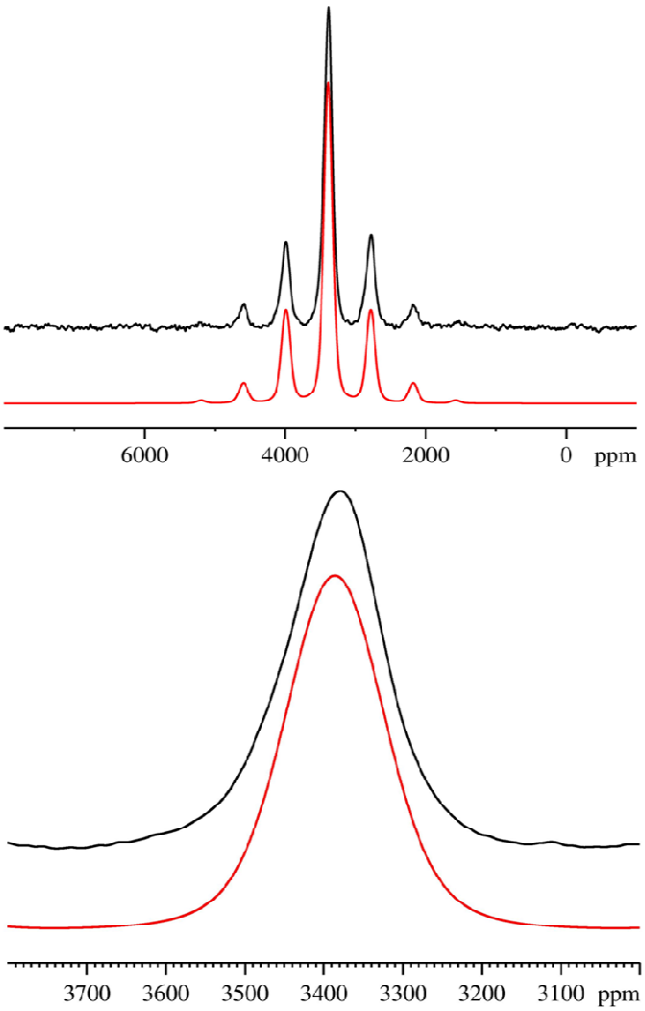

Figure 4.10 – Fe1 1D ^{29}Si experimental spectrum (black) with fitted spectrum (red) resulting from the single silicon site of the P21/n phase, Li1 (violet) and Li2 (orange).

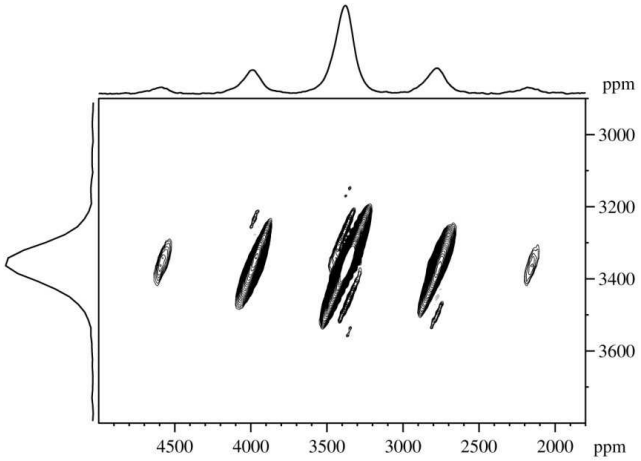

Figure 4.11- 2D ^{29}Si spectrum for the Fe1 sample.

Based on the NMR identification of the phase it was possible to index the diffraction pattern unambiguously and perform the Rietveld refinement of the data, reported in Figure 4.12; the obtained results are in very good agreement with literature data.

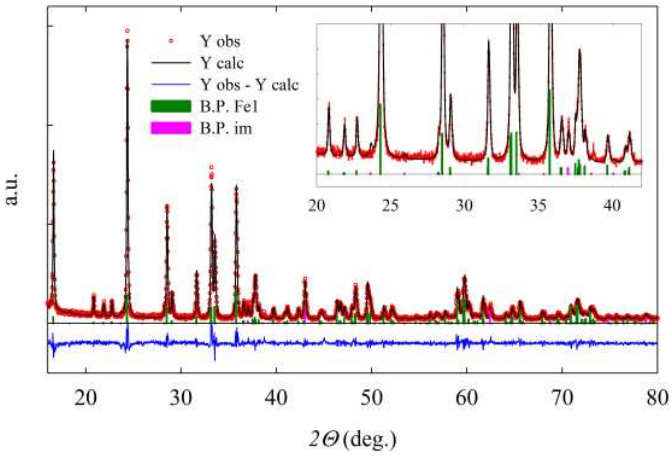

Figure 4.12 – Rietveld refinement of XRD data for sample Fe1.

4.3.5 - $Li_2Mn_{0.75}Fe_{0.25}SiO_4$

The powder diffraction pattern of the Mn075 sample presents many similarities with the one collected for the pure Mn1 sample. At the same time, the NMR spectra reveal many differences.
^{7}Li spectra are reported in Figure 4.13. The peak at 0 ppm is associated with the presence of Li_2SiO_3 phase. The signal coming from the polymorphs can be interpreted as a sum of three different contributions. The peak at -115 ppm is likely associated to the *Pmn*2$_1$ phase, while the two contributions at -61 and -98 ppm are related to the presence of the two lithium sites, Li1 and Li2 respectively, of the *P*2$_1$/*n* polymorphs. The best-fit procedure of the 1D spectrum and the projection of the indirect dimension of the 2D spectrum indicates a relative ratio of *Pmn*2$_1$: *P*2$_1$/*n* of 0.3:0.7. In order to rationalize and, possibly, to reconcile the discrepancies between the XRD Rietveld refinement and the NMR results, we performed a number of sensitivity tests on the best-fit procedure of the diffractograms. Among the checked strategies, we tried to limit the accessible intensities of the different phases. As a result, we observed that a nearly equal fit goodness can be obtained by considering *Pmn*2$_1$ as the main phase, and adding *P*2$_1$/*n* up to several tens percent. These results point out that Rietveld refinement is strongly limited when applied to these systems, because of the similarities in the peaks structure of the different polymorphs. Therefore, we will consider the NMR information as more reliable; results are reported in Table 4.3.

^{29}Si spectra are presented in Figure 4.14 (1D experiment presented on the direct dimension of the 2D spectrum). The observed shift covers a range between 8000 and 2000 ppm, the two limits identified by the two end members Mn1 and Fe1. The signal must be considered as the sum of two distinct sites coming from the two phases of the sample (in fact, both the crystallographic sites present only one site for silicon).

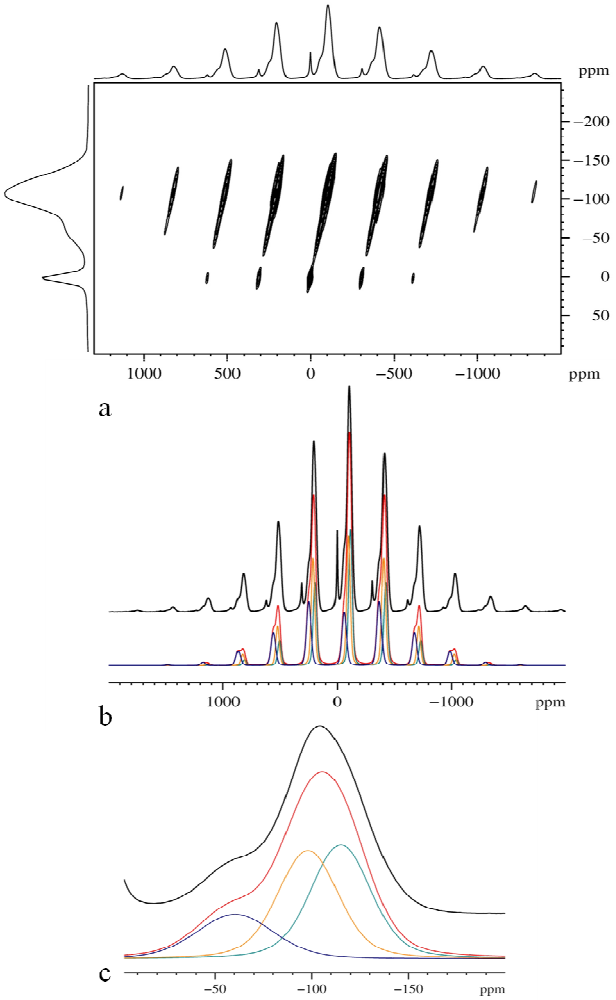

Figure 4.13 – Mn075 ^{7}Li data for the composition; a) 2D aMAT spectrum; b) experimental 1D spectrum (black) with fitted spectrum (red) and the contributions from Pmn2$_1$ (green) and the two components of the P2$_1$/n phase, Li1 (violet) and Li2 (orange); c) zoom on the central band of the 1D spectrum.

The analysis on the two patterns can be simplified by considering the 2D spectrum where the contribution of the sideband patterns is correlated to the isotropic contribution.

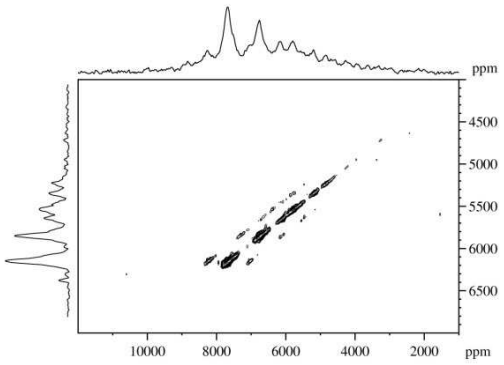

Figure 4.14 - Mn075 2D ^{29}Si spectrum, the 1D spectrum is reported as projection of the direct dimension.

Phase	***Shift (ppm)***	***Anisotropy parameter (ppm)***	***Shift (ppm)***	***Anisotropy parameter (ppm)***
	^{7}Li		***^{29}Si***	
$Pmn2_1$	-115	700	-	-
$P2_1/n$ –Li2	-57	-1250	-	-
$P2_1/n$ –Li1	-6	+ 1000		

Table 4.3 - Chemical shift and anisotropy values for ^{7}Li and ^{29}Si spectra of the Mn075 sample.

The analysis is still complex as it is necessary to consider all the possible local environments of silicon sites. In particular, silicon is tetrahedrally coordinated with oxygen ions in both the polymorphs; in both cases the cationic coordination sphere is constituted by four metal ions. Thus, in the first cationic sphere,

all the possible combinations of Mn/Fe can occur, respecting, on average, the nominal composition of the sample. For a full understanding of the ^{29}Si signals a more accurate analysis is needed and particularly DFT calculations seems to be required.[38]

4.3.6 - $Li_2Mn_{0.5}Fe_{0.5}SiO_4$

^{7}Li spectra for the mixed sample Mn05 are presented in Figure 4.15.

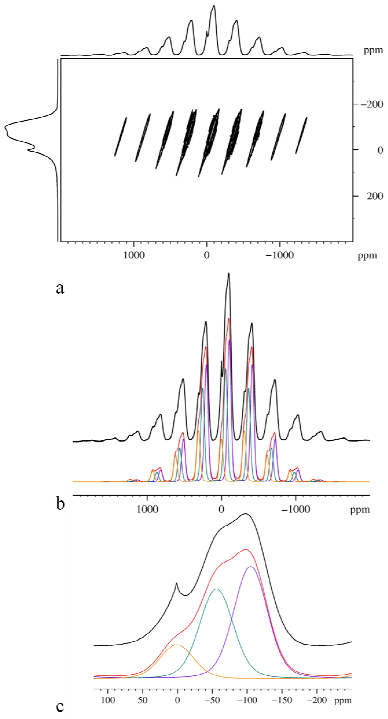

Figure 4.15 – Mn05 ^{7}Li data for the composition; a) 2D aMAT spectrum; b) experimental 1D spectrum (black) with fitted spectrum (red) and the contributions from $Pmn2_1$ (violet) and the two components of the $P2_1/n$ phase, Li1 (green) and Li2 (orange); c) zoom on the central band of the 1D spectrum.

The 1D spectrum was analyzed according to the model proposed by Sirisopanaporn et al. for the same composition.[39]
The spectra were fitted by considering three distinct sites, two related to the $P2_1/n$ phase with isotropic shift 1 (Li1) and -56 (Li2) ppm in ratio 56:44 and one peak at -105 ppm associated to the presence of $Pmn2_1$ phase. The ratio between the two phases is 1:1 as for the data presented in literature.[39]
Also in this case ^{29}Si spectra were acquired, and the results are reported in Figure 4.16. Similarly to the spectrum obtained for the Mn075 sample, the signal covers a range between 8000 and 3000 ppm; in this case the intensities profile is very different due to the different ratio Mn/Fe.

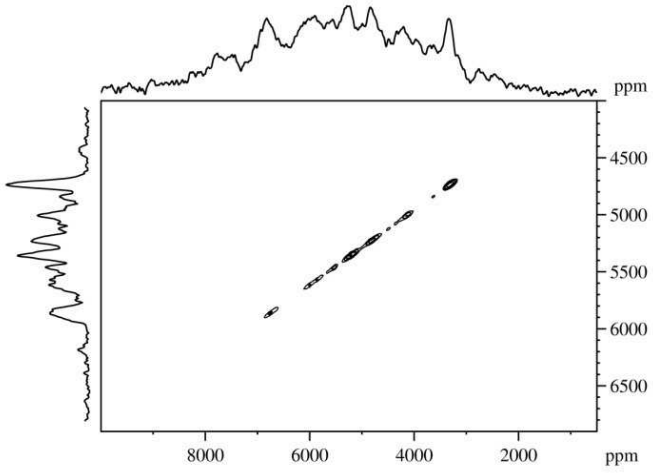

Figure 4.16 – Mn05 2D ^{29}Si spectrum; the 1D spectrum is reported as projection of the direct dimension.

In the indirect dimension it is possible to observe the presence of many different contributions due to the presence of all possible Mn/Fe combination in the first cationic coordination sphere of

silicon ion; this must be considered for all the different polymorphs present in the sample.

Phase	*Shift (ppm)*	*Anisotropy parameter (ppm)*	*Shift (ppm)*	*Anisotropy parameter (ppm)*
	^{7}Li		*^{29}Si*	
Pmn2$_1$	-105	800	-	-
P2$_1$/n –Li2	-55	-800	-	-
P2$_1$/n –Li1	1	+ 850		

Table 4.4 - Chemical shift and anisotropy values for ^{7}Li and ^{29}Si spectra of the Mn05 sample.

4.3.7 - $Li_2Mn_{0.25}Fe_{0.75}SiO_4$

The XRD powder pattern seems to be very similar to the one observed for γ_s Fe sample that was thus considered as the starting model for the structural characterization. The pattern was then indexed according to $P2_1/n$ space group.

The ^{7}Li NMR spectrum, shown in Figure 4.17, exhibits a wide spinning sidebands pattern whit broad individual central band and sidebands. Both the central band and the sidebands are asymmetric and are composed of different contributions. Particularly, the spectrum can be fitted with the use of three contributions. The results are reported in Table 4.5. Two peaks, of relative intensities 0.45:0.55, are found with chemical shift of 2 (Li1) and -52 (Li2) ppm; the shift is very similar to the values observed for the Fe sample and thus they can be associated to the presence of $P2_1/n$ phase. Also the width of the spinning sideband pattern is very similar to those observed for Fe sample and can be explained according to similar considerations relative to the local geometry of the Li1 and Li2 sites.

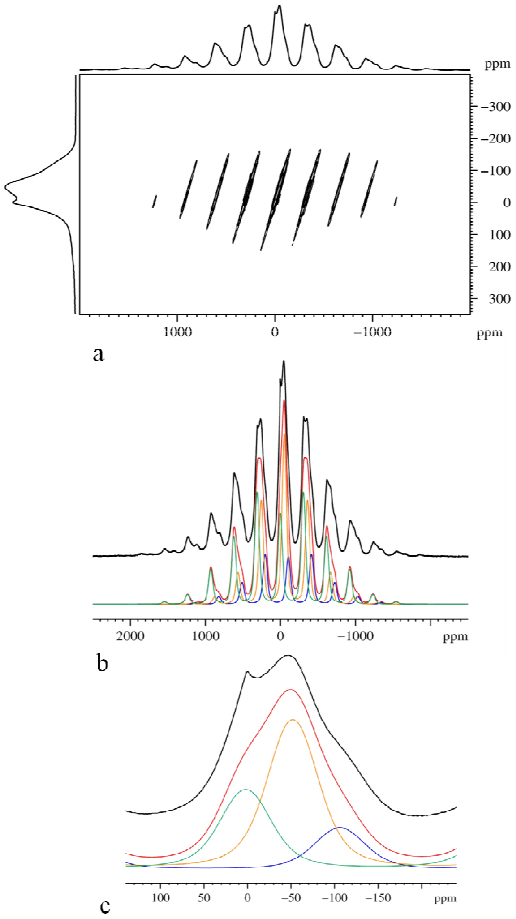

Figure 4.17 – Mn025 ^{7}Li data; a) 2D aMAT spectrum; b) experimental 1D spectrum (black) with fitted spectrum (red) and the contributions from Pmn2$_1$ (blu) and the two components of the P2$_1$/n phase, Li1 (green) and Li2 (orange); c) zoom on the central band of the 1D spectrum.

Literature data reported on a quite similar composition, $Li_2Fe_{0.8}Mn_{0.2}SiO_4$, (sample synthesized under similar heating

conditions) are in very good agreement with the results obtained for Fe075 sample.[39] The sharp peak at 0 ppm can be associated to the already mentioned impurity phase.

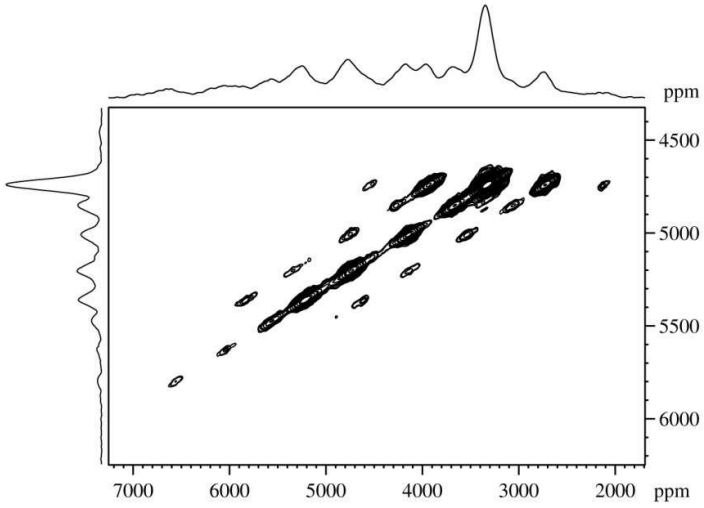

Figure 4.18 – Mn025 2D ^{29}Si spectrum, the 1D spectrum is reported as projection of the direct dimension.

The ^{29}Si NMR spectra are reported in Figure 4.18. The range of frequencies covered by the spectrum is of 6000 ppm, covering the range from the pure-Mn shift to the pure-Fe shift. The 1D spectrum, reported on the direct dimension of Figure 4.18, is complicated by the presence of two distinct polymorphs, each one with a characteristic anisotropy with extensive overlapping of the spinning sidebands, the analysis of the 1D is thus extremely complicated. Also in this case the XRD data were analyzed on the basis of the structural model obtained from the NMR study; the NMR model is consistent with XRD measurements.

Phase	*Shift (ppm)*	*Anisotropy parameter (ppm)*	*Shift (ppm)*	*Anisotropy parameter (ppm)*
	^{7}Li		*^{29}Si*	
Pmn2$_1$	-106	900	-	-
P2$_1$/n –Li2	-52	-700	-	-
P2$_1$/n –Li1	2	1100		

Table 4.5 - Chemical shift and anisotropy values for ^{7}Li and ^{29}Si spectra of the Mn025 sample.

4.4 - Conclusions

Here, for the first time, we reported a multinuclear ^{7}Li and ^{29}Si NMR study on the full series $Li_2Mn_{1-x}Fe_xSiO_4$, combined with routine X-rays diffraction analysis. First of all, we stress the difficulty in obtaining pure samples isotopically enriched in ^{29}Si. In fact, the only enriched precursor for a "solution state" synthesis available on the market was TEOS, which obliged us to perform non optimal sol-gel syntheses on very limited amounts of starting materials (this due to the high cost of enriched TEOS, which was of the order of 3k$/g).

Due to the presence of the rich polymorphism already reported in the literature, Rietveld refinement did not allow us to obtain non-ambiguous results, chiefly in the Mn-rich part of the phase diagram. Therefore, a sophisticated NMR approach, including ultrafast MAS rotation and suitable 2D sequences, was mandatory to identify the polymorphs present in the samples. Figure 4.19 reports a schematic summary of our structural findings. In the Fe-rich region of the phase diagram, the *P2$_1$/n* polymorph is indeed the most easily accessible under our synthesis conditions. When Mn is substituted for Fe, the *Pmn2$_1$* polymorph becomes increasingly important.

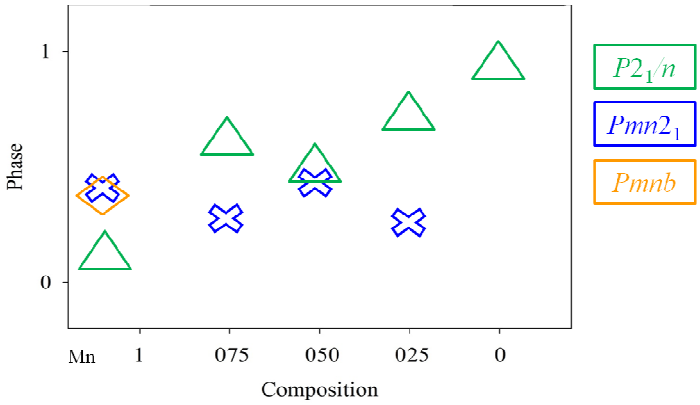

Figure 4.19 - Qualitative structural trend as function of composition at a constant synthesis temperature (700°C).

Results obtained for ^{7}Li are extremely interesting. In fact, we obtained good resolution maintaining the advantages of good sensitivity related to the use of this isotope. The analysis of chemical shifts and anisotropy indicates a clear trend with composition. In particular, chemical shifts can be calculated by considering additive contributions related to Mn/Fe exchange. According to this, it was possible to calculate and identify the expected shifts for ^{7}Li signals of samples with composition not yet reported in in literature.
A preliminary interpretation of 2D ^{29}Si spectra was also given. A more detailed attribution of the spectral features to the various polymorphs does require a parallel DFT analysis, which is at present under planning.

Results on the ^{31}P studies on similar compound, already mentioned during this chapter,[31,38] clearly indicated that the interpretation of spectra based on calculation of Fermi contact terms can be performed and give satisfactory results; from

calculations it is possible to evidence a strong correlation between the paramagnetic shifts and the number of transition metal ions in the first cationic coordination sphere and the M-O-X bond angles (where *X* is the observed nucleus) and the X-O distance.[38]

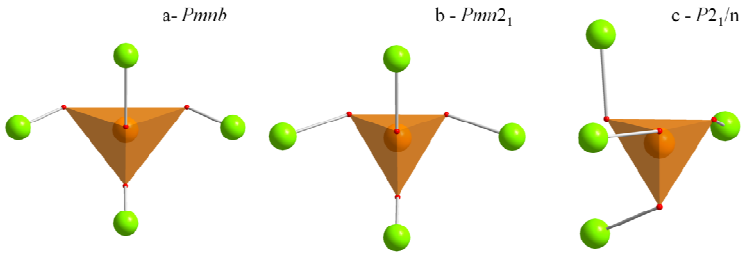

Figure 4.20 – Si tetrahedral and first cationic coordination sphere in the three polymorphs.

As reported in Figure 4.20 differences are expected mainly between the *Pmnb* - *Pmn*2$_1$ and *P*2$_1$/*n* phases, while the discrimination between the *Pmnb* and the *Pmn*2$_1$ phases could be extremely challanging. The full series of samples can be analyzed according to the presence of the two *Pmn*2$_1$ and *P*2$_1$/*n* polymorphs; the ratio between the two is a function of composition, as shown by the Figure 4.19.

The analysis of the challenging silicon spectra summarized in Figure 4.21, should start from the evaluation and full understanding of the Fe1 sample, characterized by the presence of a single polymorph. From this point the evaluation of the contributions of a second polymorph could be performed. A full characterization and a deep study of each possible polymorph is also needed, thus the isolation of the different phases could be helpful. It should be noted that the system in this case is more complex respect to the literature study for the olivine family for which only one phase is possibile.

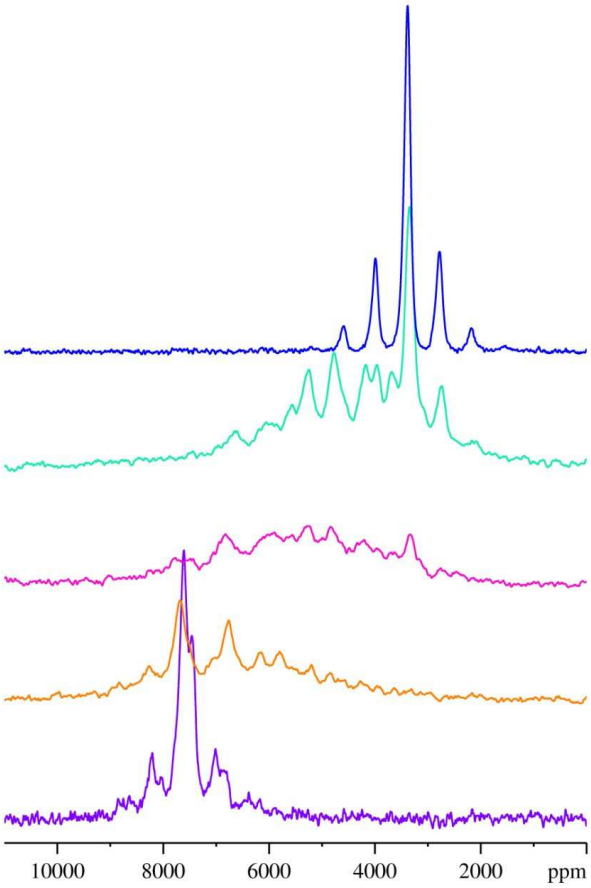

Figure 4.21 – ^{29}Si spectra for all the sample of the series $Li_2Mn_{1-x}Fe_xSiO_4$. Mn1 (violet), Mn075 (orange), Mn05 (pink), Mn025 (light blue), Fe1 (dark blue).

In the present study we must deal with at least two phases for any composition and the symmetry of the considered polymorphs is

considerably lower respect to those of the olivine system; this can further complicate the analysis and the correct evaluation of local environment of the silicon sites. The considered system presents various aspects that complicate significantly the structural analysis. At the same time the proper combination of advanced solid state NMR techniques and DFT calculation can address the problem of structural characterization of heavily complex systems.

4.4 - References

1. M. Armand, J. M. Tarascon, *Nature*, 451 (2008) 652.
2. E. Quartarone, P. Mustarelli, *Chem. Soc. Rev*., 40 (2011) 2025-2040.
3. T. Nagaura, K. Tozawa, *Prog. Batteries Solar Cells*, 9 (1990) 209.
4. M.S. Whittingham, *Chem. Rev*., 104 (2004) 4271-4301.
5. J.-M. Tarascon, M. Armand, *Nature,* 414 (2001) 359.
6. B. Ammundsen, J. Paulsen, *Adv. Mater.,* 13 (2001) 943.
7. J.R. Dahn, U. von Sacken, C.A. Michal, *Sol. St. Ion.,* 44 (1990) 87.
8. T. Ohzuku, Y. Makimura, *Chem. Lett.,* 744 (2001).
9. B. L. Ellis, K.T. Lee, L.F. Nazar, *Chem. Mater*., 22 (2010) 691.
10. J. B. Goodenough, Y. Kim, *Chem. Mater*., 22 (2010) 587.
11. A. K. Padhi, K. S. Nanjundaswamy, J. B. Goodenough, *J. Electrochem. Soc.,* 144 (1997) 1188.
12. S. I. Nishimura, S. Hayase, R. Kanno, M. Yashima, N. Nakayama, A. Yamada, *J. Am. Chem. Soc.*, 130 (2008) 13212.
13. R. Dominko, I. Arcon, A. Kodre, D. Hanzel, M. Gaberscek, *J. Power Sources,* 189 (2009) 51.
14. C. Sirisopanaporn, A. Boulineau, D. Hanzel, R. Dominko, B. Budic, A. R. Armstrong, P. G. Bruce and C. Masquelier, *Inorg. Chem*., 49 (2010) 7446.
15. A. Nyten, A. Abouimrane, M. Armans, T. Gustafsson, J.O. Thomas, *Electrochem. Comm*., 7 (2005) 156-160.
16. C. Deng. S. Zhang, B.I. Fu, S.Y. Yang, I. Ma, *Mater. Chem. Phys*., 120 (2010) 14-17.
17. R. Dominko, M. Bele, M. Gaberscek, A. Meden, M. Remskar, S. Jamnik, *J. Electrochem. Commun*., 8 (2006) 217.

18. V.V. Politaev, A.A. Petrenko, V.B. Nalbandyan, B.S. Medvedev,E.S. Shvetsova, *J. Solid State Chem.* 180 (2007) 180.
19. R. Dominko, *J. Power Sources*, 184 (2008) 462-468.
20. C. Sirisopanaporn, R. Dominko, C. Masquelier, A.R. Armstrong, G. Mali, P.G. Bruce, *J. Mat. Chem*., 11 (2011) 17823.
21. A. Kokalj, R. Dominko, G. Mali, A. Meden, M. Gaberscek, J. Jamnik, *Chem. Mater*., 19 (2007) 36333-3640.
22. A. R. West, F. P. Glasser, *J. Solid State Chem*., 4 (1972) 20.
23. A. R. West, F. P. Glasser, *J. Mater. Sci.*, 5 (1970) 557.
24. P. G. Bruce, A. R. West, *Mater. Res. Bull*., 15 (1980) 379.
25. M.S. Islam, R. Dominko, C. Masquelier, C. Sirisopanaporn, A.R. Armstrong, P.G. Bruce, *J. Mater. Chem*., 21 (2011) 9811.
26. Bruker AXS (2005). TOPAS V3.0: General profile and structural analysis software for powder diffraction data. User Manual Bruker AXS, Karlsruhe, Germany
27. G. Kervern, G. Pintacuda, L. Emsley, *Chem Phys Lett*. 435 (2007) 157.
28. G.Mali, C. Sirisopanaporn, C. Masquelier, D. Hanzel, R. Dominko, *Chem. Mater*., 23 (2011) 2735-2744.
29. G. Mali, A. Meden, R. Dominko, *Chem.Comm*., 46 (2010) 3306-3308.
30. T. Midner, H. Ernest, D. Freude, *Sol. St. Nucl. Magn. Res.*, 5 (1995) 269.
31. D.S. Middlemiss, A.J. Ilott, R.J. Clément, F.C. Strobridge, C.P. Grey, *Chem. Mater*., 25 (2013) 1723 -1734.
32. I. Belharouak, A. Abouimrane, K. Amine, *J. Phys. Chem. C*, 113 (2009) 20733-20737.
33. R.J. Gummow, N. Sharma, V.K. Peterson, Y. He, *J. Sol. State Chem*., 188 (2012) 32-37.

34. G. Mali, A. Meden, R. Dominko, *Chem.Comm*., 46 (2010) 3306-3308.
35. M.E. Arroyo-deDompablo, R. Dominko, J.M. Gallardo-amores, L. Dupont, G. Mali, H. Ehrenberg, J. Jamnik, E. Moran, *Chem. Mater.*, 20 (2008) 5574-5584.
36. S.P. Bond, A. Gelder, J. Homer, W.R. McWhinnie, M.C. Perry, *J.Mater. Chem*., 1 (1991) 327.
37. K.J.D. MacKenzie, M.E. Smith, "Multinuclear Solid State NMR of inorganic materials", Pergamon Materials Series (2002).
38. R. J. Clement, A.J. Pell, D.S. Middlemiss, F.C. Strobridge, J.K. Miller, M.S. Whittingham, L. Emsley, C. P. Grey, G. Pintacuda, *J.Am.Chem. Soc.*, 134 (2012) 17178-17185.
39. C. Sirisopanaporn, R. Dominko, C. Masquelier, A.R. Armstrong, G. Mali, P.G. Bruce, *J. Mat. Chem*., 21 (2011) 17823-17831.

Conclusions and outlooks

My thesis work has led to complete structural characterization of different classes of complex functional oxides. All the crystalline systems here presented are characterized by the presence of many kinds of defects, which are source of local disorder and lattice distortions. The combination of these factors, in most cases, made barely acceptable the characterizations performed with traditional diffraction techniques. The major issues, here, are the strong differences between the average and local structures and/or the impossibility to give a unambiguous definition of the crystal structure. Solid state NMR was proposed as the key strategy to address these aspects. At the same time, these systems are absolutely not trivial also from the point of view of NMR, since they contain quadrupolar nuclei and/or paramagnetic centers. A satisfactory approach to this kind of materials was made possible only in the last years, thanks to the development both of the NMR hardware technology and of sophisticated pulse sequences. Particularly relevant for the study of the systems presented in this thesis are the availability of very high-field spectrometers, the use of UFMAS probes, together with advanced electronic components, and the use of adequate pulse sequences.

The dramatic NMR developments are also making this technique an essential tool for structural investigation. It is possible to define the concept of *NMR crystallography* as the methodology for structural investigation and determination of bothcomplex inorganic and organic compounds. NMR crystallography is now a key element to address the relevant problem of polymorphism.

A further quantic jump is expected to be given by the recent development of dynamic nuclear polarization, *DNP*, that exploits the electronic polarization for the enhancement of the NMR signals. The use of DNP will eliminate one of the major NMR weaknesses, i.e. the low sensitivity and, at the same time, will reduce the relaxation times of the nuclei under observation. The use of DNP will make also possible the study of rare nuclei, interfaces and functionalized surfaces.
Last but not least, the availability of better analogic and digital electronics is paving the way to new experimental concepts, such as imaging under MAS conditions, and even combined techniques such as functional microimaging (*e.g. in operando* studies of electrochemical devices).